Summer 8-4-2021

Geometrically Complex Planar Heat Exchangers

Derli Dias do Amaral Junior
Southern Methodist University, ddiasdoamara@smu.edu

Jose lage

GEOMETRICALLY COMPLEX PLANAR HEAT EXCHANGERS

Approved by:

_____
Prof. José Lage
Professor of Mechanical Engineering

_____
Prof. Volkan Otugen
Professor of Mechanical Engineering

_____
Prof. David Willis
Professor of Mechanical Engineering

_____
Prof. Ali Beskok
Professor of Mechanical Engineering

_____
Dr. Antohe Bogdan
Adjunct Professor of Mechanical Engineering

GEOMETRICALLY COMPLEX PLANAR HEAT EXCHANGERS

A Dissertation Presented to the Graduate Faculty of the

Lyle School of Engineering

Southern Methodist University

in

Partial Fulfillment of the Requirements

for the degree of

Doctor of Philosophy

with a

Major in Mechanical Engineering

by

Derli Dias do Amaral Junior

MSc in Mechanical Engineering, São Paulo University, USP
BSc in Mechanical Engineering, São Paulo State University, UNESP

August 4th, 2021

ACKNOWLEDGMENTS

I would like express my sincere gratitude to my advisor, Prof. José Lage, for his guidance, encouragement, and precious advice throughout my research. His insights, experience, and suggestions contributed to my progress as an Engineer and as a researcher.

Many thanks to Prof. Ali Beskok, Prof. David Willis, Prof. Volkan Otugen, and Dr. Bogdan Antohe for their participation and valuable comments as members of my Ph.D. advisory committee. It has been an honor for me to interact with and be guided by these high-quality Professors. I am greatly thankful to all my friends at SMU for their support, especially Dr. Amir Kiaee, my lab mate. I am very grateful for the loving support of my beloved family from Brazil and here in the US. This work has been partially financially supported by the Brazilian National Research Council CNPq – Grant 208653/2014-7.

DEDICATION

I would like to dedicate my dissertation to the people from whom I have received the most support and love, my beloved wife Tatiane and my son Zyan, my dog Dooby, my beloved father Derly Amaral, who passed away in 2018, while I was here in Dallas, my precious mother Dalva D. R. Amaral and my brother Ricardo Leandro. I am nothing without you.

Amaral, Derli D. MSc in Mechanical Engineering, Sao Paulo University, USP
BSc in Mechanical Engineering, Sao Paulo State University, UNESP

Geometrically Complex Planar Heat Exchangers

Advisor: Professor José Lage

Doctor of Philosophy conferred August 4th, 2021

Dissertation completed July 08th, 2021

In this study, geometrically complex planar heat exchangers, designed in line with the Constructal Law and operating at steady-state, are investigated numerically. The work is divided into two parts, one focusing on diffusion heat transfer in a rectangular plane and another on conjugate diffusion-convection heat transfer in a circular plane heat exchanger.

In the first part, a heat generating rectangular solid volume made of a low conductivity material is cooled through a small, isothermal side-section of the domain. The diffusion cooling process is improved by distributing within the heat generating material a fixed amount of a high conductivity material. The question of how to best distribute the high conductivity material to cool the domain and at the same time optimize the decrease in its maximum temperature is answered via geometric optimization based on Constructal Law. The result is a T-shaped network type distribution for the high conductivity material embedded in the heat generating volume. However, this embedded approach, called here the "in-plane" distribution, is of very limited practical use for being too intrusive to the domain. An alternative proposed and investigated here is the "out-of-plane" distribution, in which the high conductivity material network is placed on top of the heat generating plane. Three different network distributions with increased complexity and same specifications (i.e., same uniform heat generation rate, planar aspect ratio and thickness of

generating volume, and same volumes of base material and high conductivity material) are investigated numerically for both, in-plane and out-of-plane configurations. The main objective is to compare the heat transfer effectiveness achieved by each configuration. This aspect is very important because, if the effectiveness are comparable, the option of using the out-of-plane distribution could alleviate the practical limitations of the in-plane (embedded) configuration. An additional effort in this first part of the project is to extend the analysis to a non-dimensional parametric study, where the number of different networks is increased to six and different amounts of low and high thermal conductivity materials are investigated. This part if not only to establish if in-plane and out-of-plane yield similar results, but also to understand how the high/low thermal conductivity volume ratio influences the removal of heat out of the heat generating volume.

The results, obtained numerically, show the two networks, i.e., in-plane and out-of-plane, yield nearly identical temperature distributions and heat transfer effectiveness (to within the numerical uncertainty achieved by the simulations) for all configurations tested. Hence, one can confidently use the out-of-plane networks instead of the in-plane networks in practical applications of T-shaped network cooling cold plates. The results also confirm the robustness of the thermal design and extend previous work, showing an increase in network complexity (e.g., by increasing the number of assemblies in each network) indeed yields better cooling performance, even when some of the stringent assumptions imposed in the analysis of building the networks are not fully satisfied.

In the second part of the work, a heat generating material in a circular planar domain (a disk) is now cooled via convection through circular channels from the center to the periphery of the domain. The optimum distribution of the fixed volume convection channels in the domain, again following Constructal Law, yields a tree-shaped network starting with one inlet at the center

of the disk, and flowing through bifurcating channels toward a set number of outlets distributed uniformly at the periphery of the disk. Here the thermal-hydraulic performance of the resulting tree-shaped flow networks is obtained numerically and compared to the simpler, radial flow networks (feeding the same number of peripheric outlets) for cooling the disc. The flow entering at the center of the disc is assumed isothermal and fully developed. Two tree-shaped flow networks are considered, having either six (one bifurcation level) or twelve (two bifurcation levels) outlets, conceived for maximizing the cooling and minimizing the flow resistance. Both, tree-shaped and radial flow configurations are set with the same disc solid and fluid (channels) volumes, and same uniformly distributed volumetric heat generation rate in the solid region.

The results show the best performance flow distribution depends on factors that go beyond the channels being either radial or bifurcating, highlighting the very complex heat transfer interaction in this conjugated convection-diffusion system. Moreover, the flow separation effect intrinsic to the channel bifurcations and neglected in previous studies, is essential to the thermal design as it affect not only the overall pressure loss but also the overall heat transfer performance, particularly when the flow channel Reynolds number is high, as one would expect.

TABLE OF CONTENTS

LIST OF FIGURES

LIST OF TABLES

NOMENCLATURE

C	constant
D	disc diameter, m
D_i	path height, m
D_i	section hydraulic diameter, m
f	dimensionless flow resistance
H	height, m
H_i	height length, m
k	thermal conductivity, $Wm^{-1}K^{-1}$
L_i	depth length, m
$\dot{m}$	mass flow, kg s^{-1}
M	dimensionless mass flow
N	number of outlets
Nu	Nusselt number
n	direction perpendicular to surface
n_0	number of central ducts
p	constructal level, pressure, N m^{-2}
Pr	Prandtl number
q	heat generation rate, W
q'''	volumetric heat generation rate, W m^{-3}
R	disc radius, m
Re	Reynolds number
R	solid radius, m
S	mean rate-of-strain tensor
Sv	svelteness number
t	disc thickness, m
T_0	inlet temperature, K
T_m^*	thermal resistance
T^*	non-dimensional temperature
u	velocity, m s^{-1}

U_0	mean inlet fluid velocity, m s^{-1}
V	total flow channel volume, m^3

Greek symbols

α, β, γ	angles, rad
ΔP	pressure loss, N m^{-2}
μ	fluid viscosity, kg m^{-1} s^{-1}
ρ	fluid density, kg m^{-3}

Subscripts

eff	effective
f	fluid
i	assembly index, rank of tube
H	high
L	low
k	kinetic
opt	optimal
p	pipe
x, y, z	Cartesian coordinates
rd	radial
s	solid
t	turbulent
0, 1, 2, ...	tubes positioned sequentially from the origin
o	elemental volume parameter

Superscripts

$*$	non-dimensional parameter

INTRODUCTION

In a ground-breaking study, Bejan [1] considered how to best distribute a finite amount of high thermal conductivity material into a uniformly heat-generating volume to facilitate the flow of heat out of the volume through a small lateral isothermal area (a heat sink), or, equivalently, to minimize the maximum temperature attained by the heat generating material. Originally a simple optimization challenge, the search for an appropriate solution to the material distribution problem gives rise to an infinity of possible geometric alternatives. Following the simplest possible geometry for the high thermal conductivity material distribution, a set of paths resembling T-shaped networks emerge. As one proceeds from the simplest to the more complex network alternative, the results get progressively better – meaning, the maximum temperature inside the heat generating domain gets smaller. That is, the evolution toward more complex geometries (or networks) yields an easier flow of heat and a more efficient system. This fundamental engineering design process, in turn, was observed to mimic the time evolution of several natural transport systems, systems observed to progress in time, or to evolve toward more complex geometries to achieve better, easier processes. This observation supports a new natural (physics) law, named Constructal law.

Constructal law successfully explains the observed time-evolution of shapes and structures of diverse natural and engineering systems [2]. The law deals with the morphing of the system through time, or the design evolution, and it postulates that “For a finite-size flow to persist in time

(or to continue to exist), it must evolve in such a way that it provides easier and easier access to the flow that goes through it" [1]. Constructal law has been applied in many fields of science, not only in engineering [3-8].

Here, guided by the Constructal law, consideration is given to planar heat transfer systems of increasingly complex geometry. These systems aim to operate as cold-plates, or simply as facilitators of thermal energy transferring from where it is generated to where it is cooled. In common, the systems considered here are planar (i.e., one dimension is much smaller than the other two), they have specific base-configurations (simplest possible geometries) used for performance comparison, they operate either under conduction or under a conduction-convection (conjugate heat transfer) combination, and have limited real-estate available for design (either a fixed volume of high thermal conductivity material available for the conduction case or a fixed amount – volume - of flow channels available for the conduction-convection case). The work is divided in two parts, as detailed next.

The first part of the work consists of a 3D and steady numerical analysis of the conduction heat transfer process through a uniform heat generating low conductivity material in a planar rectangular geometry. The volume is cooled by an isothermal heat sink located along one of the sides of the domain, with all other exposed surfaces considered adiabatic. A base configuration is built by imbedding a high conductivity material throughout the heat-generating volume forming T-shaped networks as suggested by the optimization distribution process. This distribution, called in-plane configuration, aims at improving the heat transfer process out of the domain, resulting in a lower maximum temperature within it. For being disruptive and highly impractical (for requiring imbedding the high conductivity material within the heat generating volume) an alternative distribution is also considered, in which the high thermal conductivity material is placed atop the

heat generating material without directly disturbing it, in a configuration called out-of-plane. A preliminary effort is then pursued considering a square domain designed with practical geometrical dimensions and materials. Three of the simplest T-shape square networks for the high conductivity material are shaped and applied to each configuration for comparison purposes, each using exactly the same amount (volume) of low and high conductivity materials. The main objective is to compare the performance of the two (in-plane and out-of-plane) configurations, evaluating the practicality of using the out-of-plane, instead of the in-plane, configuration as a cold plate design. The second effort follows focusing on a parametric study of the thermal performance of each configuration in terms of the thermal conductivity ratio of the cold plate. In this effort, several additional T-shape networks for the high conductivity material are considered as well.

The second part of the work consists of 3D and steady numerical analysis of radial (the base-configuration) and tree-shaped flow networks for cooling a planar heat generating disk. The disk has a single inlet at the center and a certain number of outlets uniformly distributed along its periphery. The incoming flow is isothermal and fully developed and the channels to the periphery are all regular circular channels. Two tree-shaped flow networks are considered, having either six (one bifurcation level) or twelve (two bifurcation levels) peripheric outlets, all conceived for minimizing flow resistance. The diameter and length of the channels change after each bifurcation in the tree-shaped networks. Both, tree-shaped and radial, flow configurations are set with the same disc solid and fluid (channels) volumes, and volumetric heat generation rate. The effect of varying the flow rate through the disk is considered not only in the heat transfer performance but also in the hydraulic efficiency of the system.

1 OUT-OF-PLANE T-SHAPED CONDUCTING NETWORKS: ALTERNATIVE FOR PRACTICAL APPLICATION

The volume-to-point cooling design problem proposed by [1] was tackled with basic conduction principles, considering a heat generation rate q uniformly distributed within a certain thin rectangular material of thermal conductivity k_L and volume V_0, where $V_0 = L_0 H_0 W$, L_0 being the depth, H_0 the height, and W the width of the volume, yielding a volumetric heat generation rate $q''' = q/(L_0 H_0 W)$. Figure 1 shows a view from the top of volume V_0. This volume is cooled via a mid-side opening of small area (heat sink), maintained at temperature T_0, centrally located at (x,y) = (0,0) in the figure, through which heat flows out of the volume, with all other boundaries being adiabatic. At steady-state, this configuration leads to a maximum temperature T_{max} in the volume achieved at the corners (symmetry) at $x = L_o$ and $y = \pm H_o/2$, opposite to the heat sink.

The analysis [1] then proceeds with the utilization of a finite amount of a high thermal conductivity material, of volume V_H and conductivity k_H, to help reduce the maximum temperatures in the domain. This material is considered to be imbedded with the heat-generating material as if distributed "in-plane" with it. Note in the analysis that both, high and low thermal conductivity materials, occupy the domain volume V_0; i.e., there is in this analysis an intrinsic assumption of the volume occupied by the high conductivity material V_H being much smaller than V_0. A first and simplest (most regular) geometric alterative for distributing the k_H material is a straight path connecting the heat sink centered at (x,y) = (0,0) to the opposite end of the volume, located at (x,y) = (0, L_o), as shown by the dashed area in Figure 1. Observe the volume occupied by the high conductivity material in this simplest configuration is $V_H = L_0 D_0 W$ as shown in Fig. 1, with D_0 being its height; hence, $V_H/V_0 = H_0/D_0$, and the requirement $V_0 \gg V_H$ translates into $D_o \ll H_o$.

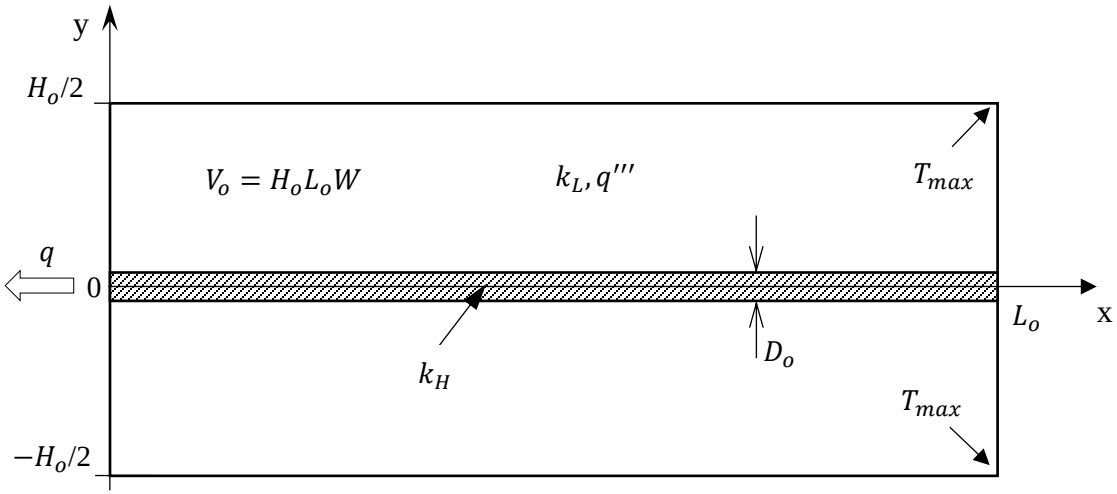

Figure 1. Elemental volume V_0 with heat generating material k_L and high thermal conductivity material k_H.

The temperature difference between the heat sink temperature T_0 and the hottest spot temperature T_{max} in V_0 of Fig. 1, written as $\Delta T_0 = T_{max} - T_0$, can be shown to be equal to [1]:

$$\Delta T_o = \frac{q'''}{2k_L}\left(\frac{H_0}{2}\right)^2 + \frac{q''' H_o}{k_H D_o}\frac{L_o^2}{2} \tag{1}$$

It is worth keeping in mind Eq. (1) is an approximated result valid when the heat conduction through k_L is unidirectional in *y*, which is satisfied when the domain is slender, i.e., $H_o \ll L_o$. Also note Eq. (1) allows for the minimization of ΔT_0 with respect to the shape of the elemental domain, H_0/L_0 (this can be seen by nondimensionalizing ΔT_0, dividing it by $q''' L_0 H_0/k_L$), yielding the result:

$$\left(\frac{H_0}{L_0}\right)_{opt} = 2\left(\frac{k_L H_0}{k_H D_o}\right)^{1/2} \tag{2}$$

In view of the slenderness requirement, $H_o \ll L_o$, and remembering by construction $H_0 > D_0$, Eq. (2) also requires $k_L < k_H$, which reassures the design choice of using a high thermal conductivity material, in relation to the heat generating base material. The geometrical lengths of the first assembly, $i = 0$, is now complete because H_0, D_0 and k_H, k_L are all specified by the thermal designer and Eq. (2) provides the remaining shape relation of the first construct $i = 0$.

The evolution of the k_H distribution within k_L proceeds by realizing the need to approximate the high thermal conductivity material even more to the points with maximum temperature, at the top and bottom right corners of Fig. 1, to better cool the domain. This leads naturally to a second construct, $i = 1$, a T-shape structure built by placing several optimized first constructs side-by-side perpendicular to the y = 0 line of the domain, as shown in Fig. 2 (only two first constructs are shown in the top right corner of the domain for visual simplicity). This simple option immediately yields a geometric requirement for this second construct, namely $H_1 = 2L_{0,\text{opt}}$, which links the geometry of the first construct to the geometry of the second. The optimization of the lengths H_1, L_1 and D_1 of this second construct follows the same analysis as the optimization of the first, by reducing the visual resolution used to look at the domain to "see" the region occupied by the first construct (the regions above and below the horizontal k_H region) simply as a homogeneous heat generating region occupied by a composite material made of materials k_L and several branches of k_H. In passing, this homogenization trick is commonly used to simplify the analysis of complex porous media. Under this homogenization approach, the new construct is seen exactly as the first one, as shown in Fig. 1, but now with a different heat generating region, still dissipating the same total amount of thermal energy but with an equivalent conductivity k_1. Observe the analysis provides the optimum number of first constructs to be connected to the horizontal (L_1,D_1) section as $n_{1opt} = 2\ L_{1opt}/H_0$.

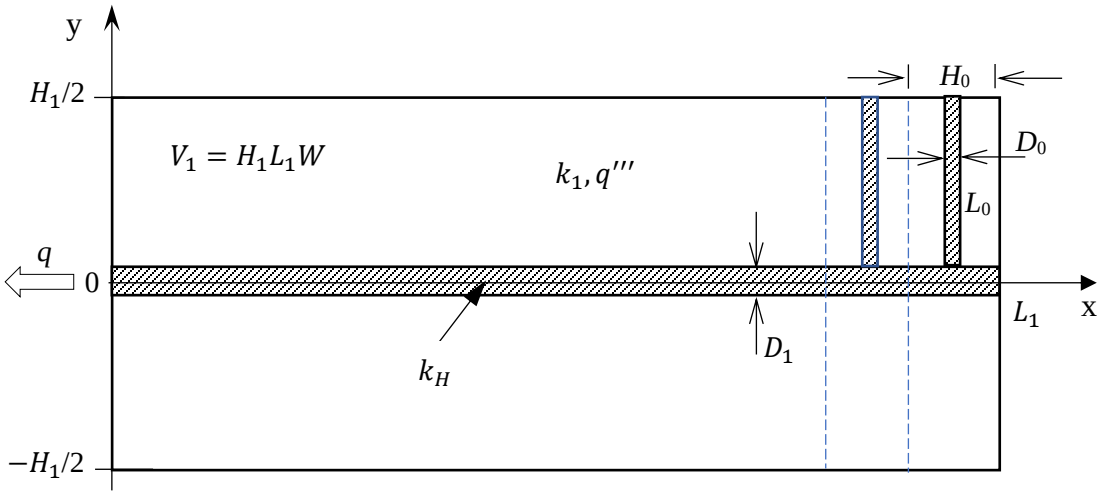

Figure 2. Primary volume V_1 with composite heat generating material made of several (only two shown) first constructs i = 0 with k_L and k_H and each measuring H_0, L_0 and D_0, connected to k_H, measuring L_1 and D_1 forming the new construct i = 1.

A third T-shaped construct, i = 3, can be imagined in a manner similar to the first and second, with additional similar steps followed by induction. Figure 3 shows the resulting structured (network) after four iterations, with the first elemental construct having length L_0, and the last having length L_4, as indicated in the figure. Only the two extreme assemblies L_0 are shown connected to L_1 in Fig. 3; the full network would be populated with these assemblies on both sides of L_1, filing the entire domain. Also noteworthy is that, when the constructs evolve from i = 0, the number of branches continuously decreases; in line with the fact of the domain being adiabatic on the right side, it becomes unnecessary to fill the entire domain with high conductivity material. That is why the length of the high conductivity material of constructs larger than i = 1 does not cover the entire domain length; for instance, in the case i = 4 in Fig. 3, L_4 is not equal to the total depth of the domain.

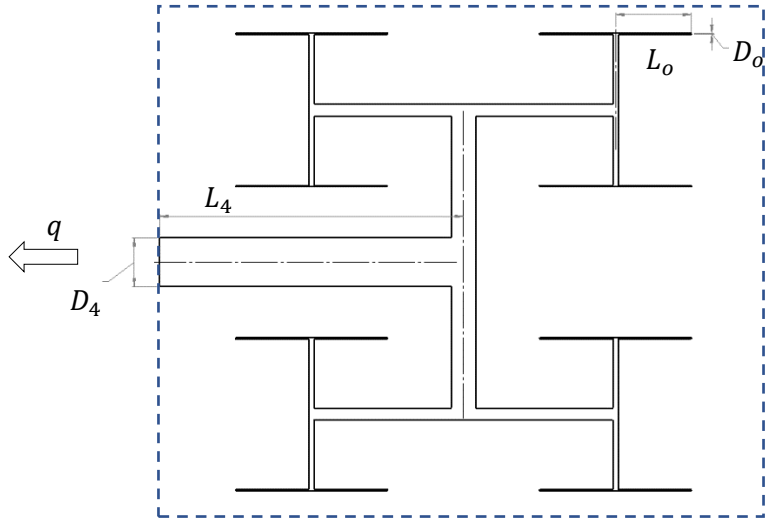

Figure 3. Assembly i = 4 of the T-shape network.

Finally, every assembly construction step i is followed by the optimization of the k_H volume dimensions (i.e., assembly height H_i, depth L_i and branch height D_i; keep in mind the assembly width W is kept constant for k_H being in-plane with k_L) to minimize the maximum temperature of the system. More details about the construction and the optimization process can be found in [1] and [9]. Table 1 shows the resulting parameters optimized for the first seven assemblies, from [1].

Table 1. Main geometric parameters of the first seven optimized assemblies [1].

Assembly i	Assembly height factor H_i/H_{i-1}	Assembly Shape[a]	Branch height factor D_i/D_{i-1}	Assembly depth factor L_i/L_{i-1}
0	-	*R*	-	
1	$\left(\frac{D_0 k_H}{H_0 k_L}\right)^{1/2} \gg 1$	*R*	$\left(\frac{D_0 k_H}{H_0 k_L}\right)^{1/2} \gg 1$	*1*
2	*1*	*S*	*2.31*	*1*
3	*2*	*R*	*2*	*1*
4	*1*	*S*	*2*	*1*
5	*2*	*R*	*2*	*1*
6	*1*	*S*	*2*	*2*

[a]S – square, $H_i = L_i$; R – a rectangle with aspect ratio $L_i/H_i = 2$

1.1 Designing Practical T-shaped Network Cold Plates: Out-of-plane Configuration

The construction analysis leading to the geometry presented in Fig. 3, is based on imbedding the high thermal conductivity material in the heat generating domain. In practice, this would be a tremendous task for being very invasive – one would have to insert the very complex network of k_H into k_L without disrupting the heat generating characteristics of the domain. An alternative to facilitate the use of the high conductivity network in practice, particularly by circumventing the imbedding (in-plane) of material k_H in the domain, is introduced here.

Because of the practical nature of the present effort, all the basic dimension and material specifications are chosen with a possible future manufacturability and assembly of the cold plate in mind. Hence, the domain is chosen as square, with height H and depth L equal to 0.254 m (10

in) and width W equal to 6.35×10^{-3} m (¼ in). Copper and resin are chosen as material k_H = 400 W/mK and k_L = 1.5 W/mK, respectively, due to their large difference in thermal conductivities (leading to k_H/k_L = 267), great availability, and easy machining/molding. Resin volume V_L equals 2.56×10^{-4} m^3 (15.625 in^3) and copper V_H equals 1.536×10^{-4} m^3 (9.375 in^3), with total volume being 4.097×10^{-4} m^3 (25 in^3). Notice, with these volumes, the last construct ratio of the network is set as having H_n/D_n = 1.67. Also set is the smallest dimension feature of the network to be equal or larger than 2 mm (this is the high conductivity material height D_0 of the first construct).

Three networks, shown in Fig. 3 (imbedded in the base material), with different assembly levels of increasing complexity (i.e., i = 0, 2 and 4), are pursued for preliminary analysis and for establishing how the in-plane configuration compares to the new alternative configuration.

The height H_i, depth L_i and branch height D_i, of each assembly in each network are found using the data and correlations shown in Table 1. Keep in mind the fitting of the network within the available volume is not a simple task. The resulting geometries are generated in a CAD 3D software with a parametric link to Excel to iteratively solve for all lengths involved in each network assembly to guarantee the correct final resin and copper volumes in each case.

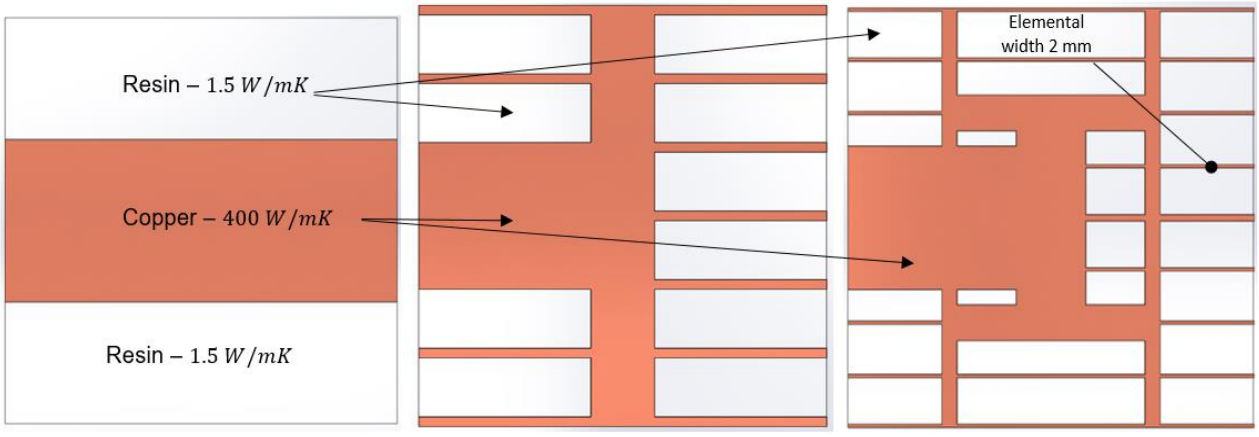

Figure 4. From left to right, embedded (in-plane) T-shaped networks with i = 0, 2, and 4, respectively.

The construction of the networks is based on the smallest element of the fourth assembly [10], that is, the building process is from the smallest to the largest construct, with all dimensions having a tolerance of $\pm$ 0.2 mm (set as a convergence criterion in Excel).

Before proceeding, it is worth pointing out the chosen very small resin-copper volume ratio, namely 1.67, does not align itself with the analysis followed when building the optimized network – recall in the initial assumption of negligible high conductivity volume. It so happens the resulting geometric relations derived from the analysis impose severe restrictions on the network geometry because the height D_0 of the smallest branches become very small very quickly when i increases. A relatively large volume of high conductivity material is chosen here to allow for a reasonable (manufacturable) size of the smallest branch height (limited to 2 mm). Nevertheless, the deviation from the original assumption regarding the high conductivity material volume will be revisited in the conclusion section of this chapter.

Now, the alternative configuration considered here places material k_H atop (out-of-plane) the base material k_L. In this way, the high conductivity material need not be imbedded in the base material, but simply placed on top (or bottom) of it, a configuration much easier to achieve in practice once a high conductivity material network is built. The two considered configurations, i.e., either imbedded or atop the base material, are shown in Fig. 5 for the i = 4 network.

Observe the width W of the resin in the out-of-plane configuration (right of Fig. 5) must be adjusted to yield the same total resin volume as the amount used in the in-plane network (left of Fig. 5), that is $W = 3.97 \times 10^{-3}$ m (5/32 in) for the out-of-plane configuration. Doing so guarantees not only the same resin volume but also the same total thermal energy dissipated by the base material (keep in mind the same base material volumetric heat generating rate is used in all cases).

The width of material k_H in the out-of-plane network, on the other hand, is maintained as 6.35 × 10^{-3} m (¼ in), or the same as the width used in the in-plane networks (because the copper network used in both configurations is identical, with identical volume).

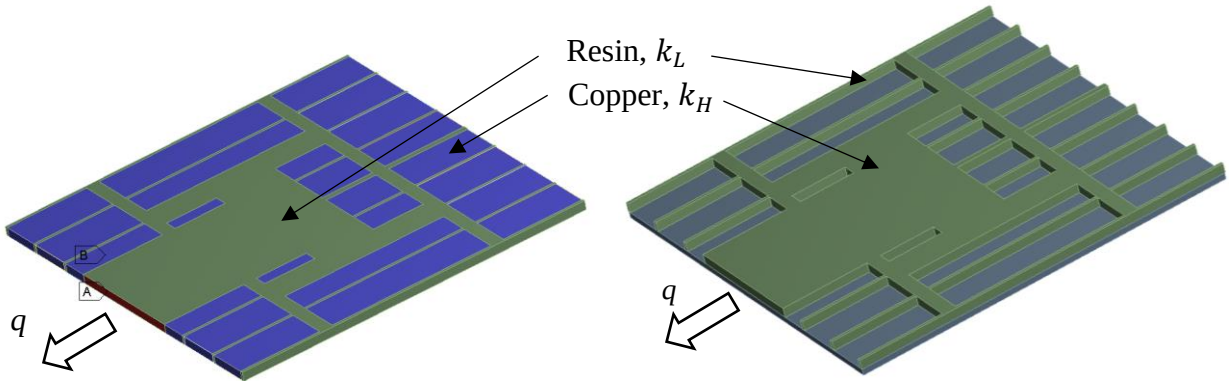

Figure 5. In-plane network (left) and out-of-plane network (right) for i = 4.

1.2 Comparing In-plane and Out-of-plane Configurations: Numerical Simulations

The in-plane and out-of-plane configurations form two sets, each with the three networks shown in Fig. 4, for a total of six domains to be tested. In all cases, the volumetric heat generation rate dissipated in the resin (base material, k_L) is set as $q''' = 50$ kW/m^3. The resulting thermal energy generated in the domain is drained through the isothermal heat sink operating steadily at 22 °C along the side of the domain (Fig. 5). Observe the heat sink area coincides with the area occupied by the high conductivity copper material at the left boundary of the domain in all cases, while all other surfaces of the domain are considered adiabatic.

The numerical simulation of the heat transfer process in each configuration is performed considering a domain with height H, depth L and width W, using a 3D, steady conduction equation

for homogeneous material with volumetric heat generation rate term q''' applied to the resin (base, low conductivity k_L material) region, and without the heat generation term when applied to the copper (high conductivity k_H material) region, respectively Eqs. (3) and (4):

$$\frac{\partial^2 T}{\partial x^2} + \frac{\partial^2 T}{\partial y^2} + \frac{\partial^2 T}{\partial z^2} + \frac{q'''}{k_L} = 0 \tag{3}$$

$$\frac{\partial^2 T}{\partial x^2} + \frac{\partial^2 T}{\partial y^2} + \frac{\partial^2 T}{\partial z^2} = 0 \tag{4}$$

with adiabatic boundary conditions, i.e., $\partial T/\partial n = 0$, along all external surfaces with normal n except the heat sink surface, where $T = T_0$. Equation (4) might give the wrong impression the problem solution is independent of k_H. However, in dealing with two distinct materials in the domain, as in the present case, compatibility conditions must be imposed at their interfaces, i.e., identical temperatures $T_H = T_L$, and heat fluxes $k_H \partial T_H/\partial n = k_L \partial T_L/\partial n$, where n is now the direction perpendicular to the resin-copper interface. Keep in mind that, imposing of continuous heat flux at the interface implies a perfect thermal contact between the two materials. Observe once the network is chosen, the parametric space affecting the temperatures within resin and copper is composed of H, D, W, k_H, k_L and q''', all with values set already.

A second-order space-accurate finite-volume scheme, with non-uniform grid distributed in all directions, is used for the simulations. The numerical grids are refined near the interfaces of the two materials to reduce the effects of heat-generation and thermal conductivity discontinuities. Extensive grid accuracy tests are performed considering the most demanding (with largest temperature gradients) case, i.e., for the $i = 4$ network. The results presented here are guaranteed to be accurate to less than 1%, in terms of the difference in local temperatures within any domain, when the number of grid points used is doubled.

Figure 6 presents temperature distribution results side-by-side for both configurations, namely in-plane (left) and out-of-plane (right), for the simplest $i = 0$ network case (see Fig. 4). Recalling the domain is 3D, these temperature distributions are along the top plane of the domain. Notice in the out-of-plane case the temperature distribution is of the top surface of the resin (the region interfacing the copper network placed above it). Notwithstanding, the thicknesses of both configurations being so small (in comparison to the domain lengths along the two other directions) and the top and bottom sides being adiabatic guarantee negligible temperature variation along the z direction (i.e., direction perpendicular to the plane of Fig. 6). The minimum temperature in all cases equals 22 °C, which is the heat sink set temperature.

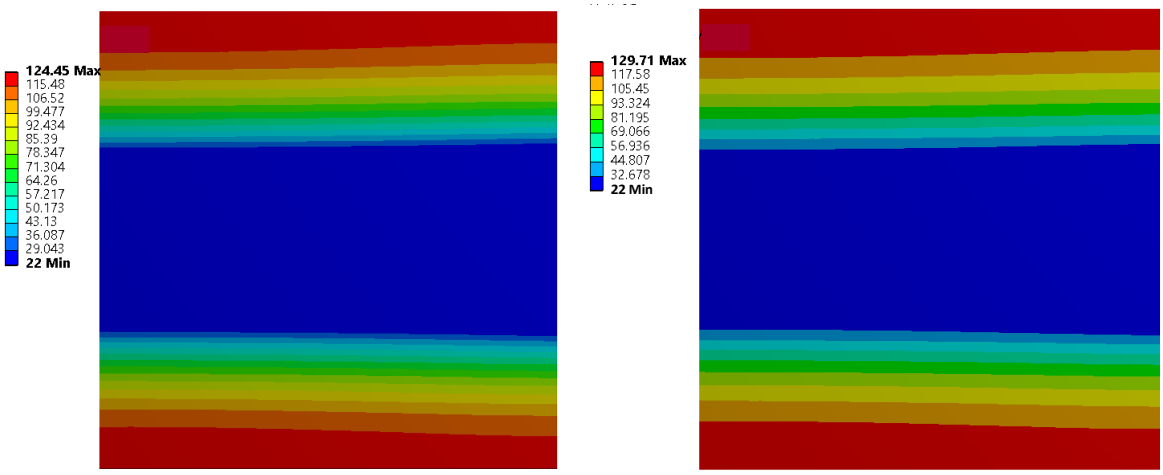

Figure 6. Temperature distribution for in-plane (left) and out-of-plane (right) configurations, both for the simplest $i = 0$ network case.

The temperature distributions of Fig. 6 show the heat flux within the domain to be predominantly along the y direction toward (perpendicular to) the high conductivity material region, in support of one of the assumptions made when deriving Eq. (1). The maximum

temperature within the entire domain in each case is 124.45 °C for the in-plane case, and 129.71 °C for the out-of-plane case. The resulting T_{max} being slightly higher for the out-of-plane case is consistent with the slightly longer path for the heat to flow through and out of the system (the heat must move up from the base material to the high conductivity material in the out-of-plane configuration to be transported to the heat sink, as opposed to moving through it in the in-plane configuration). In conclusion, the maximum difference in the local temperatures between the two configurations in this case equals 5.26 °C, or 4.2 % deviation from the in-plane network result.

Figure 7 shows similar temperature distribution results, but now using the second network of Fig. 4, with i = 2, when the maximum temperatures in each case equal 38.73 °C for the in-plane case (left) and 39.04 °C for the out-of-plane case (right). Again, the maximum temperature of the out-of-plane case is slightly higher than the maximum temperature of the in-plane case. Observe the difference between the two cases drops to only 0.31°C, or approximately 0.8 % deviation from the in-plane configuration result – the distributions of both configurations are practically identical.

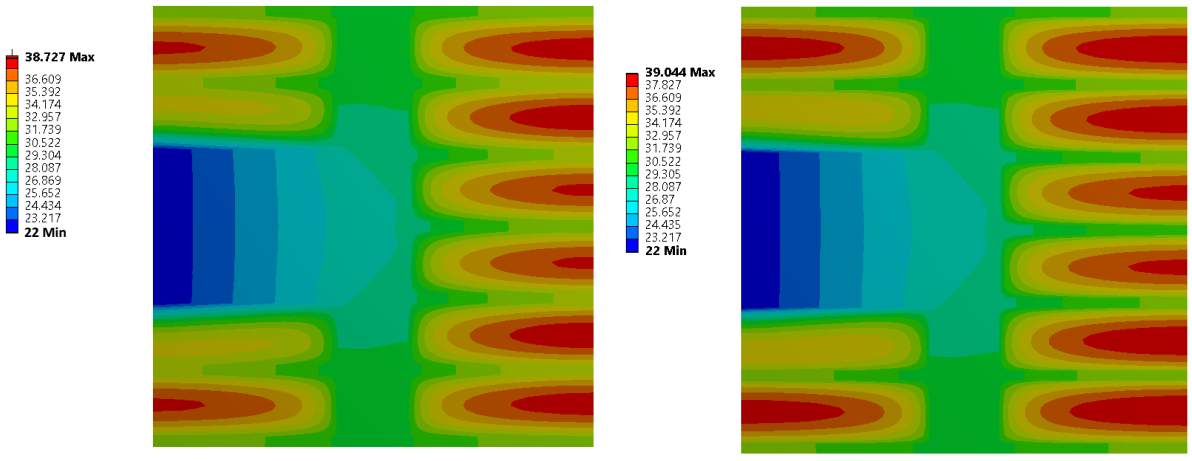

Figure 7. Temperature distribution for in-plane (left) and out-of-plane (right) networks (i = 2).

The last network considered here, with i = 4, yielded the temperature distributions shown in Fig. 8. In this case, the maximum temperature equals 37.28 °C for the in-plane case (left) and 36.98 °C for the out-of-plane case (right). Observe the maximum temperature difference between the two cases drops again, although slightly, now to 0.30°C, or approximately – 0.8 % deviation from the in-plane network result. Noteworthy is the maximum temperature of the out-of-plane case being slightly lower than the maximum temperature of the in-plane case. This result is meaningless because the difference is within the uncertainty of the numerical results.

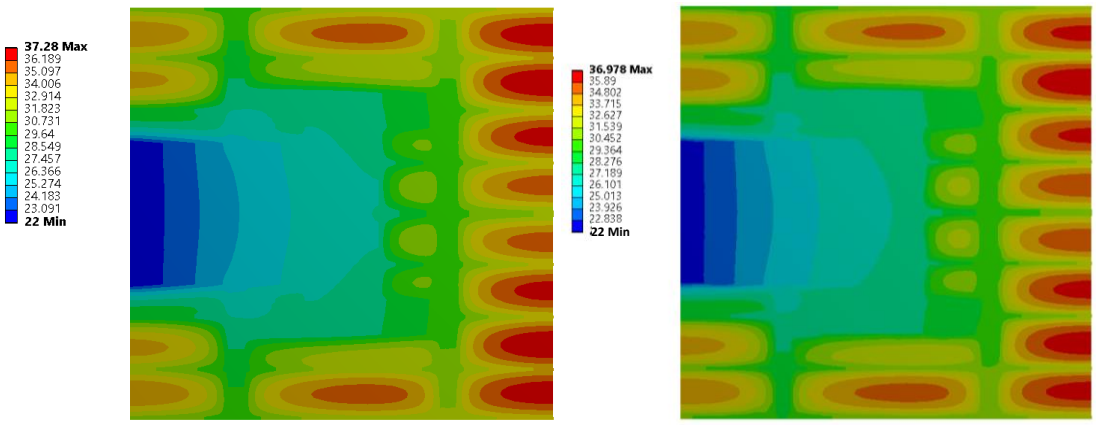

Figure 8. Temperature distribution for in-plane (left) and out-of-plane (right), both with i = 4.

1.3 Summary and Conclusions

The problem of cooling a heat generating planar (thin) volume through a small, lateral, isothermal heat sink, utilizing a finite amount of high thermal conductivity material, is re-visited with emphasis on the practical utilization of the resulting cold plate design.

The minimization of the maximum temperature of the heat generating material using T-shape networks leads to a series of geometric relations for the dimensions of the network branches in the cold plate. The minimization analysis assumes the high conductivity material to be imbedded (in-plane) into the base heat generating material, restricting its application. An alternative out-of-plane configuration, in which the high conductivity material network is placed on top of the generating base material is then considered to facilitate the utilization of the resulting cold plate design. A preliminary comparison of the two (in-plane versus out-of-plane) configurations is then pursued numerically considering a practical cold plate system made of heat generating resin (the base material) and copper (the high conductivity material), with each configuration tested for three distinct and simple networks.

Resulting temperature distributions indicate the increase in network complexity, by increasing the number of assemblies in each network (i.e., increasing i from 0 to 2), indeed yields better cooling performance, even when some of the stringent assumptions imposed in the optimization analysis of building the networks (for instance $H_o \ll L_o$ and $V_H \ll V_L$, see [1]) are not strictly satisfied by the present design. The results obtained here then show the optimized T-shaped network to be more robust than originally expected (this aspect concurs with and extends some of the observations found in [10]).

More importantly, the present results also show the two, in-plane and out-of-plane, configurations yield essentially identical temperature distributions (to within the numerical uncertainty achieved by the simulations) when $i \geq 2$. Hence, the practical utilization of the Constructal-inspired networks using T-shape assemblies with two distinct materials at steady-state can be more easily accomplished in practice by using the out-of-plane networks instead of the in-plane networks.

A final note is necessary regarding the thermal contact resistance between the surfaces of the two materials, not accounted for in the model and numerical simulations performed here. In practice, even if the imbedded configuration is possible, the thermal contact resistance between the two materials would exist in the in-plane configuration. This is also the case for the out-of-plane configuration. When i is small (0 and 1), however, the contact area (interface) between the two materials is much larger in the out-of-plane configuration than in the in-plane configuration. Hence, it is possible to anticipate the present results are conservative with respect to the out-of-plane configuration, as in practice the thermal contact resistance is likely to be a more imposing hindrance to heat flow in the in-plane configuration than in the out-of-plane configuration. As the number of constructs increases ($i > 1$), the difference in contact area between the two materials is reduced, and the thermal contact effect should tend to become equal in both cases. Again, in practice the out-of-plane configuration has the advantage of allowing for pressing the high conductivity network against the base material more easily, hence allowing for a better thermal contact, and reduced thermal resistance, than in the in-plane configuration.

2 CONDUCTIVITY RATIO EFFECT ON THERMAL PERFORMANCES OF IN-PLANE AND OUT-OF-PLANE CONDUCTIVE NETWORKS

2.1 Introduction

Here the problem considered in the previous chapter is revisited and expanded to investigate the thermal conductivity ratio, k_H/k_L, effects on both, in-plane and out-of-plane configurations. Also, all networks included in Table 1 are tested – notice the network final shape depends on the number of assemblies used, with i = 1, 3 and 5 yielding rectangular networks with H_i/L_i = 2, and i = 2, 4, and 6 leading to square networks with H_i/L_i = 1, which affects the ideal domain shape H and L where such networks can fit. Figure 9, as an example, shows the most complex network considered here, i = 6 (square), with the first elemental construct having a height D_0 and depth L_0, and the last having height D_6 and depth L_6, as indicated in the figure. All the resulting optimized parameters are obtained following Table 1.

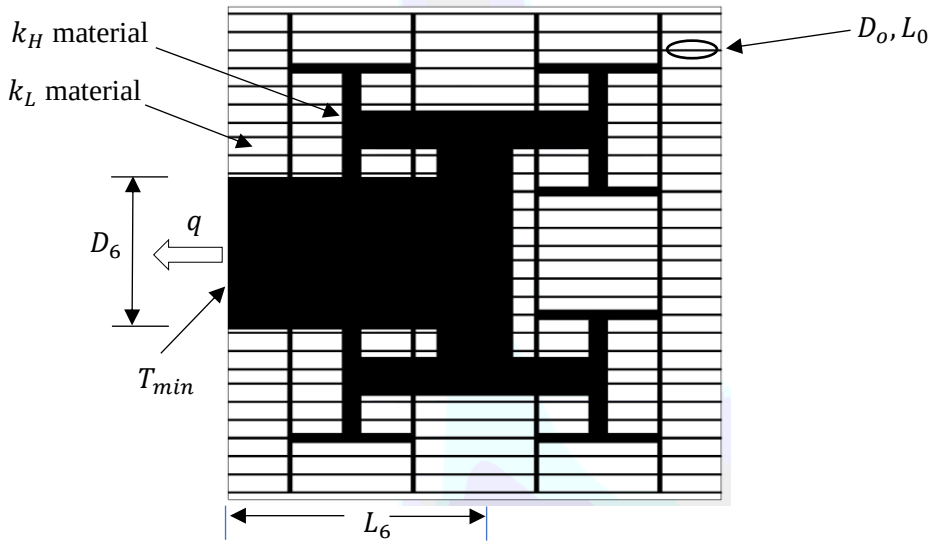

Figure 9. Sixth assembly, i = 6, of the T-shape network.

2.2 Modeling and Numerical Simulations

The numerical simulations of the resulting heat transfer process in each configuration, within a domain with height H, depth L and width W, are performed as described before, using Eqs. (3) and (4) with listed boundary and interface conditions. The formulation is altered, to make the results broader, by nondimensionalizing the length parameters in respect to the domain depth L, with $(x^*,y^*,z^*) = (x,y,z)/L$, and the temperatures as

$$T^* = \frac{T - T_0}{\frac{q''' L^2}{k_L}} \tag{5}$$

The resulting balance equations, equivalent to Eqs. (3) and (4), for the base and high conductivity material regions, become:

$$\frac{\partial^2 T^*}{\partial x^{*2}} + \frac{\partial^2 T^*}{\partial y^{*2}} + \frac{\partial^2 T^*}{\partial z^{*2}} + 1 = 0 \tag{6}$$

$$\frac{\partial^2 T^*}{\partial x^{*2}} + \frac{\partial^2 T^*}{\partial y^{*2}} + \frac{\partial^2 T^*}{\partial z^{*2}} = 0 \tag{7}$$

The boundary conditions become $\partial T^*/\partial n^* = 0$, along all surfaces and $T^* = 0$ along the heat sink surface, and the compatibility conditions imposed along all interfaces between the base and the high conductivity materials become: $k^* \partial T_H^*/\partial n^* = \partial T_L^*/\partial n^*$, and $T_H^* = T_L^*$, where the new parameter is $k^* = k_H/k_L$. Observe the parametric space ruling the heat transfer results, once a network is chosen, is now made of only three parameters, namely the domain height and width aspect ratios, $H^* = H/L$ and $W^* = W/L$ (note the other domain dimension becomes $L^* = 1$), and the thermal conductivity ratio k^*. Interestingly, the nondimensional results, in terms of T^*, are independent of the volumetric heat generation rate term q'''.

2.3 Domain and Networks

Because of the different resulting shape of the networks (see Table 1), two domains are considered here, one with $H^* = L^* = 1$, for the square networks $i = 2$, 4, and 6, and another with $H^* = 2$, $L^* = 1$, for the rectangular networks $i = 1$, 3, and 5. In all in-plane configuration cases, the even (square) assemblies had $W^* = 0.025$ and the odd (rectangular) assemblies had $W^* = 0.0354$ (these are reasonable dimensions, considering the planar nature of the cold plates). The total domain volumes are then either 0.025 or 0.0708, depending on the aspect ratio of each domain.

All high conductivity material networks are built following Table 1, using CAD 3D with a parametric link to Excel as described in the previous chapter. Figure 10 shows the resulting six different network geometries tested. The ratio between the heat generating volume V_L and the high conductivity volume V_H is set as $V_L/V_H = 3/2$ for all cases. Again, the thickness of the heat generating material must be adjusted in the case of the out-of-plane configuration to keep the same heat generating volume.

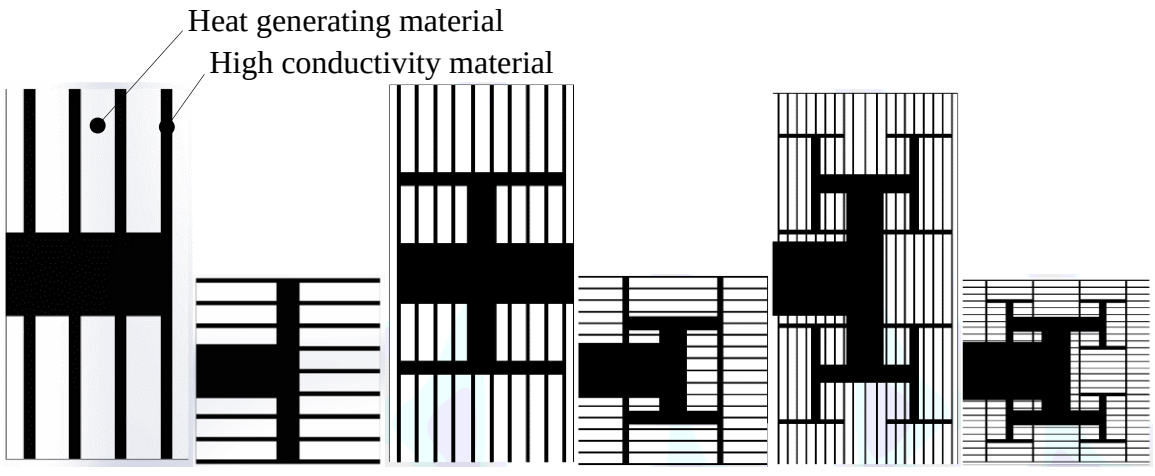

Figure 10. T-shape networks, from left to right with $i = 1$ to 6, with correct aspect ratios.

Hence, $W_L^* = 0.015$ for the square assemblies and $W_L^* = 0.0425$ for the rectangular assemblies in the out-of-plane configurations; no thickness adjustment is necessary for the high conductivity material, as the network is maintained the same in both configurations.

The out-of-plane configuration is designed similarly as described before (Chapter 1). Figure 11 shows a side-by-side 3D rendition of the two configurations for the square network obtained with $i = 2$. Keep in mind, again, the thickness of the heat generating material is reduced in the out-of-plane configuration, while the high conductivity material network is identical in both configurations. The size of the heat sink surface equals the size of the high conductivity material surface centered at the origin to the left of the domain, indicated with $T^* = 0$ in Fig. 11, being identical in both cases.

Finally, the numerical simulations are done as before, using a second-order finite volume scheme, with a non-uniform grid in all directions. Again, the grids are refined near the interfaces of the two materials to reduce any discontinuity effects. Extensive grid accuracy tests are performed, and less than 1% difference is achieved by the local temperature values reported here when the number of grid points used in the numerical simulations is doubled.

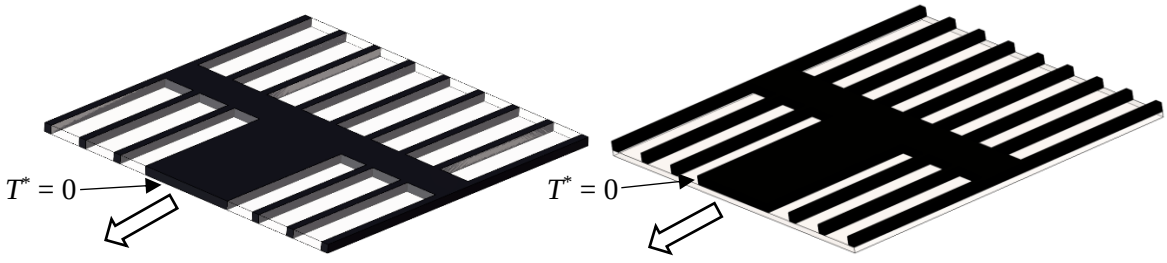

Figure 11. In-plane network (left) and out-of-plane network (right) for $i = 2$.

2.4 Results

Figures 12 and 13 present, for a qualitative comparison, the T^* distribution at the top surface of the domains, side-by-side for the $i = 1$ to 6 networks (from left to right), and for the in-plane and out-of-plane configurations, respectively (out-of-plane configuration T^* distribution refers to the top of the heat generating material).

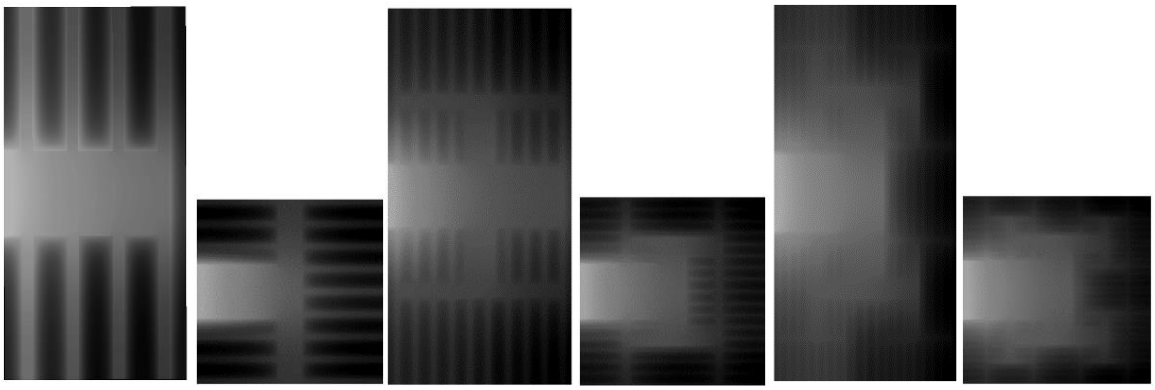

Figure 12. Temperature distribution for in-plane configuration, i = 1 to 6 (from left to right), with k^* = 267.

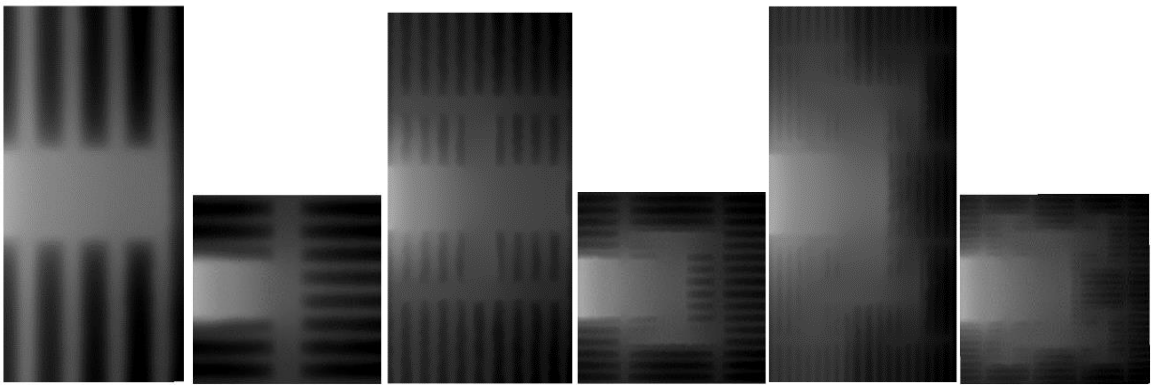

Figure 13. Temperature distribution for out-of-plane configuration, i = 1 to 6 (from left to right), with k^* = 267.

Keep in mind the minimum temperature in the domain for all cases is $T^* = 0$ located at the heat sink surface of each cold plate (centered along the left side of the domain in the region occupied by the high conductivity material). As seen, the results of each configuration in Figs. 12 and 13 are very similar to each other. Also interesting, the increase in the number of assemblies makes the variation of temperature in the domain more subtle (the network branches become less discerning as *i* increases), as expected. This is a consequence of the eas access to the flowing heat in the domain achieved by the higher order and more complex network assemblies.

The obtained maximum temperature T^*_{max} within each domain is shown in graphical form in Figure 14, for the rectangular (i = 1, 3, 5), and for the square networks (i = 2, 4, 6). Observe, as mentioned before in the modeling section, the T^* results are independent of the heat generation rate term q''' but not of the domain geometry, which are different when the aspect ratio of the networks differs. This explains why the temperatures of the even assemblies in Fig. 14 differ from the temperatures of the odd assemblies.

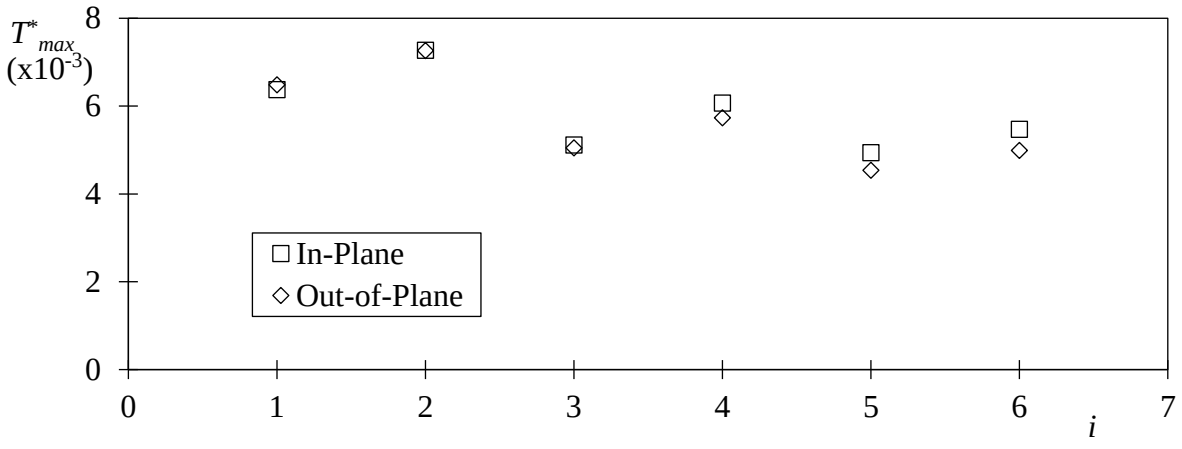

Figure 14.Maximum nondimensional temperature T^*_{max} versus i for k^* = 267.

The in-plane results of Fig. 14 fall slightly above the results for the out-of-plane configurations, with the difference increasing with *i*. Although the difference is very small and very close to the uncertainty of the numerical simulations, this difference is likely a manifestation of the larger contact area between the heat generating material and the high conductivity material provided by the out-of-plane configuration in comparison to the in-plane configuration.

The graphs presented in Figures 15 through 21 show T^*_{max} for similar cases as in Fig. 14, but with different k^*, from 10 to 8,000. Included are the results for $k^* = 267$ for completeness. Figure 15, for instance, for k* = 10, shows not only a large T^*_{max} value, of order 0.10, as expected when k^* is small (see Eq. (5)), but also a small variation as *i* increases. This indicates the small difference between the thermal conductivities of the generating material and the high conductivity material hinders the networking role of facilitating the heat flow out of the domain. Observe also the very small difference between the in-plane and out-of-plane results in each case.

Interestingly, a strong effect of increasing the complexity of the networks is observed only when k^* increases beyond 100, Fig. 17. Before then the results show little change as *i* increases.

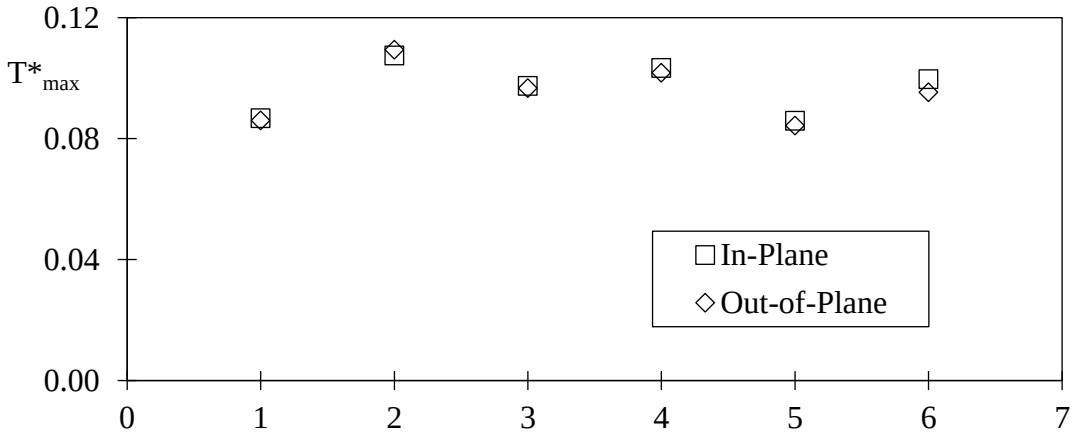

Figure 15. Maximum nondimensional temperature T^*_{max} versus *i* for $k^* = 10$.

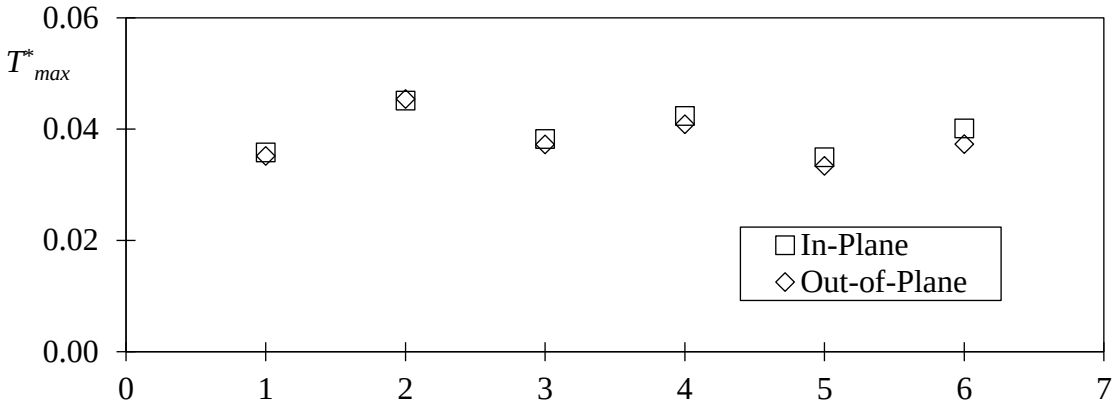

Figure 16. Maximum nondimensional temperature T^*_{max} versus i for $k^* = 30$.

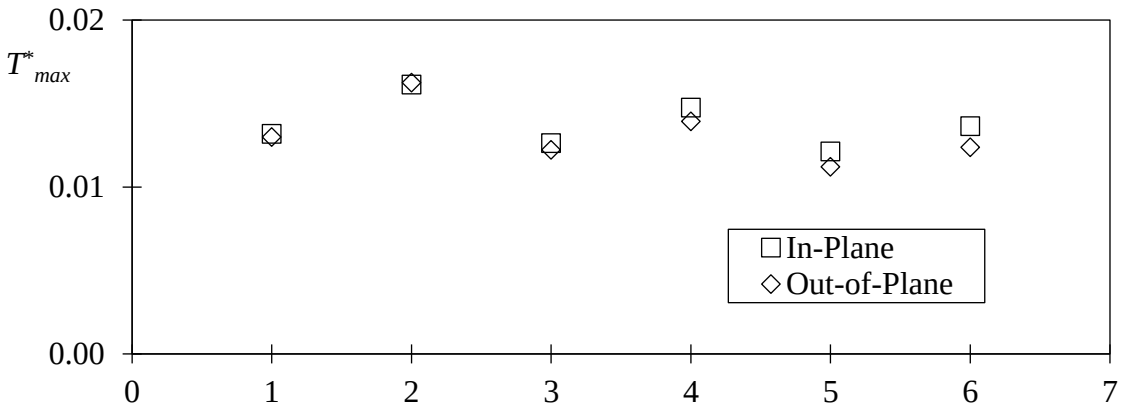

Figure 17. Maximum nondimensional temperature T^*_{max} versus i for $k^* = 100$.

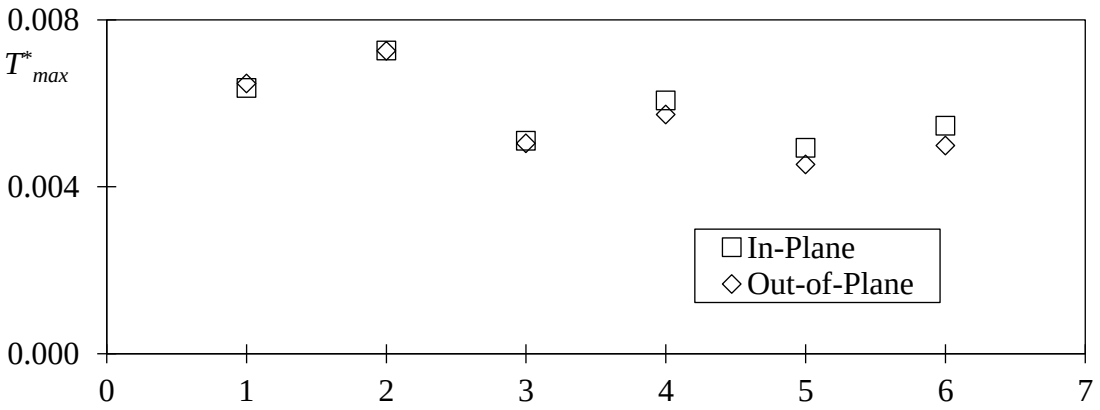

Figure 18. Maximum nondimensional temperature T^*_{max} versus i for $k^* = 267$.

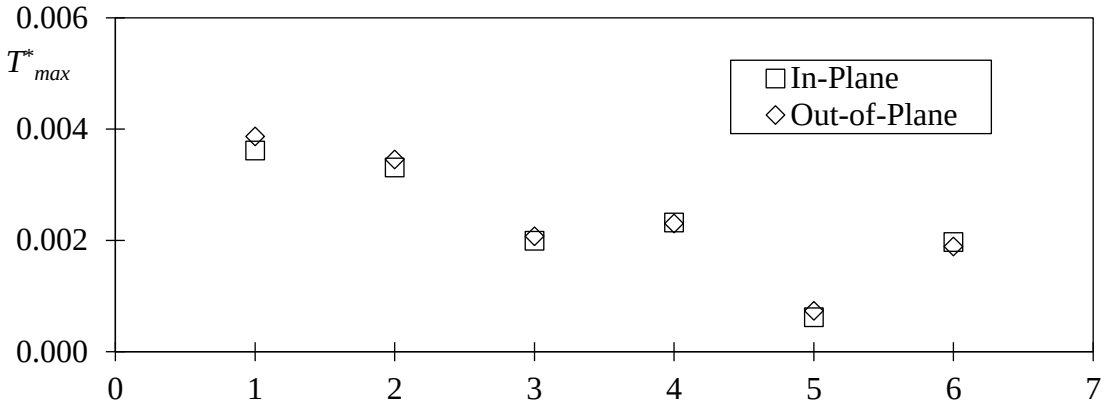

Figure 19. Maximum nondimensional temperature T^*_{max} versus i for $k^* = 800$.

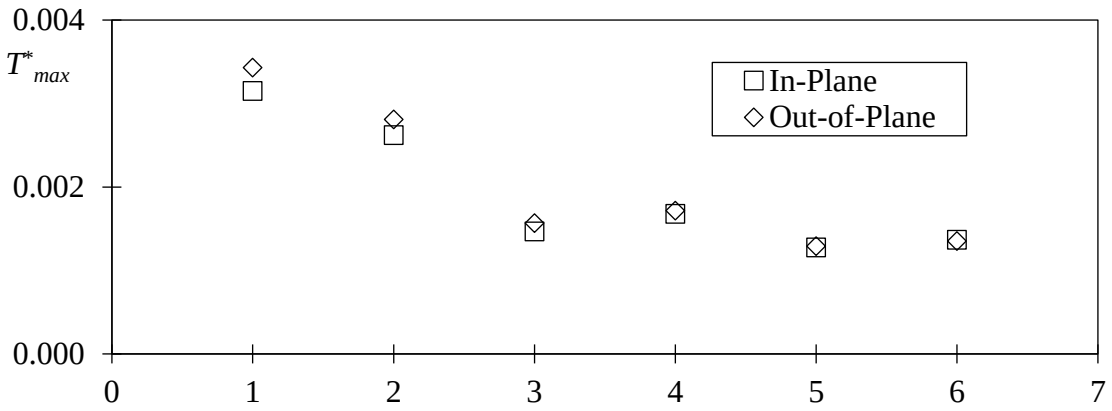

Figure 20. Maximum nondimensional temperature T^*_{max} versus i for $k^* = 1{,}200$.

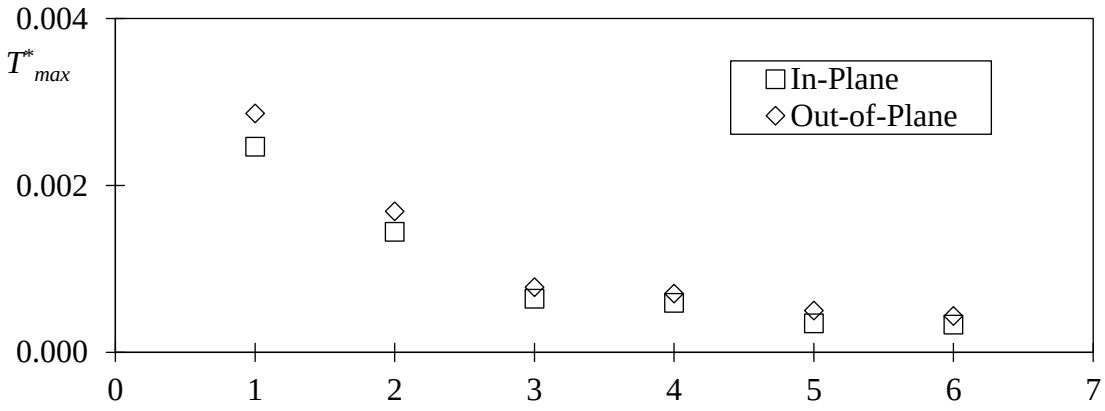

Figure 21. Maximum nondimensional temperature T^*_{max} versus i for $k^* = 8{,}000$.

As k^* increases beyond 100, the effect of using more complex networks (higher i) of high conductivity material becomes much more prevalent, particularly when i is smaller than 4. This aspect becomes independent of the aspect ratio of the network as well. Note, when k^* increases beyond 3,000, the effect of increasing i does not change much anymore. Finally, all results indicate very little difference between the in-plane and out-of-plane configurations. Figures 22 and 23 present results for in-plane and out-of-plane, respectively. The similarity of the results of both configurations is striking.

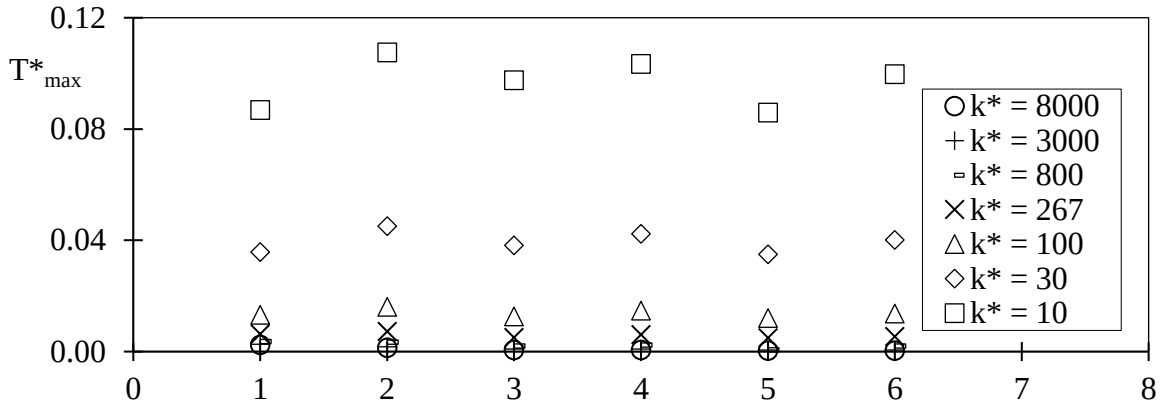

Figure 22. Maximum temperature versus i for in-plane configuration.

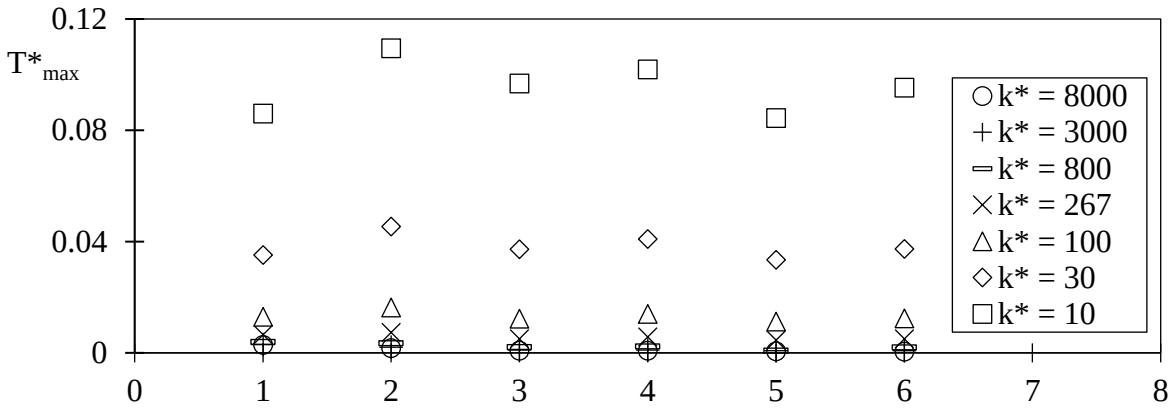

Figure 23. Maximum temperature versus i for out-of-plane configuration.

A highlight of the effect of increasing k^* is shown in Fig. 24, where the temperature distribution of the domain is presented for k^* from 10 to 8,000, for the out-of-plane configuration with the i = 4 assembly. The effect of enhancing the flow of heat through the high conductivity material is clear as k^* increase: observe how the network becomes increasingly more visible as k^* goes from 10 to 8,000 - the tendency is for the high conductivity material region to become more isothermal. Temperature range is the same for all plot of Fig. 24.

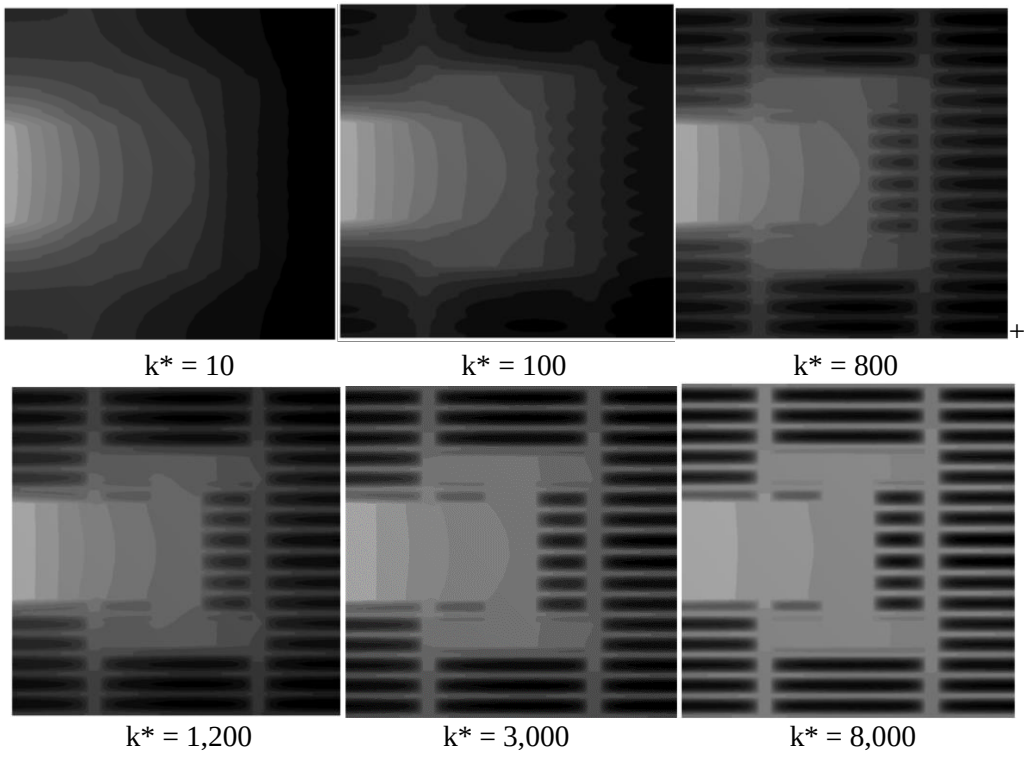

Figure 24. Effect on temperature distribution T^* as k* increases out-of-plane with i = 4.

2.5 Summary and Conclusions

The analysis presented in Chapter 1 is extended to perform a comparison between in-plane and out-of-plane configurations under different high-to-low thermal conductivity ratio, using six distinct optimal T-shape networks of increasing complexity. The geometries of these networks

present two distinct aspect ratios, making them suitable for two distinct cold plates (with different surface areas). The mathematical formulation, including balance equations, boundary and compatibility conditions for numerical simulations presented in Chapter 1, is nondimensionalized to identify the ruling parameters of the heat transfer process in the cold plate.

The results, obtained numerically, indicate the increased effectiveness of the high conductivity material network to cool better the heat generating material as the complexity of the design increases using more assemblies. This increase becomes predominant as the thermal conductivity ratio k^* increases beyond 100, and it tends to flatten out for i larger than 3 and k^* larger than 800. Similarly to the results presented in Chapter 1, the high conductivity material networks seem to be very robust: they achieve the desired objective even when some of the stringent assumptions imposed in the derivation of their geometries (for instance $V_H \ll V_L$, see [1]) are not satisfied.

More importantly, the present results also show the two networks, i.e., in-plane and out-of-plane, yield essentially identical temperature distributions. Hence, the practical utilization of the T-shape networks in plane cold plates becomes much more feasible, now that the out-of-plane configuration is shown to be as efficient as the in-plane configuration.

3 OPTIMAL BIFURCATING FLOW NETWORKS FOR COOLING A HEAT GENERATING DISC – LAMINAR FLOW CASE

This chapter considers the thermo-hydraulic implications of using convection channels for cooling a heat generating disc-shaped domain. This is essentially a conjugate problem, when conduction through a solid domain is coupled with convection through a flow network.

Thermal science in the past decades has been marching towards smaller and smaller scales. The proper use of the real estate available is one of the priorities in thermal design. Hence, volumetric optimization is extremely important, particularly in the cooling of electronics [11-13], where high heat density (heat generated per unit of volume) is a common characteristic [1].

In the previous two chapters, consideration is given to cooling a heat generating planar rectangular volume utilizing conduction heat transfer through a high conductivity material. T-shape networks emerge as a simple, feasible optimal path for the high conductivity material. A similar approach can be used for colling a solid plane disc [14].

The problem gets more complicated, and interesting, when one envisions replacing the conductive heat transfer path made of a solid material by ducts carrying a cooling (or heating) fluid, yielding a flow cold plate. When the total volume of the ducts is fixed, the question of how best size and distribute the ducts to minimize the maximum temperature of the heat generating material emerges naturally, making the problem very similar to the one tackled in Chapters 1 and 2. Wechsatol et al. [15] considered such a problem, suggesting an optimal tree-shaped flow network designed for cooling an insulated heat generating solid disc by convection. The simplest possible flow networks are the radial configuration, formed by circular ducts emanating from the center of the disc going straight (radially) toward the periphery. More complex networks are built

by allowing the original radial ducts to bifurcate, with the number of bifurcations determining the number of delivery (flow outlets) at the periphery. The geometry of the ducts (diameter and length) is optimized, following a very simplified analysis, for reducing the maximum temperature of the heat generating material. Thermo-hydraulic performance curves are then obtained for each network, with the results indicating the direct radial flow configuration (without any branching) yielding best thermal performance, while the branched (bifurcated) networks yielding best flow performance (less pressure-drop or pumping power).

Lu Zhihao [16] considered a disc-Y-shaped liquid cooling cold plate, where the effect of branching level on cooling performance was analyzed. When comparing networks with one to four branching levels, the peak temperature and average temperature were reduced by 28.8% and 13.5%, respectively, with the increases in pressure loss to be less than 0.04 kPa.

Further studies on the optimization of disc heat convection flow networks were performed by [17, 18], where the goal was the minimization of flow and thermal resistances. Due to the reduction of electronic components, microchannel disc-shaped cold plates are considered [19-21] good alternatives to the more common and less effective parallel flow cold plates.

The objective here is to re-visit the original work of [15] leading to the design of optimal bifurcating flow networks for cooling a heat generating disc material. The simplifications imposed in the analysis leading to the optimized flow networks, mainly that of fully developed laminar flow in each flow branch, are likely to have distorted thermo-hydraulic results. Several flow networks are then investigated, with the thermo-hydraulic process studied by a heat generating disc simulated numerically for several flow configurations, covering laminar and turbulent flow regimes in the flow branches.

3.1 Flow Networks

A sample configuration considered here is presented in Fig. 25, showing the top view of a solid heat generating plane disc of diameter R fit with an optimal flow network made of circular pipes emerging from its center. This flow network sprawls toward the periphery of the disc, linking, via discrete branches, the center inlet to discrete outlets located around the outer circumference. Notice each of the three symmetric radial pipes leaving from the disc center, with diameter D_0 and length L_0, undergoes a bifurcation with angle α, giving rise to six pipes each with diameter D_1 and length L_1. Each of these secondary pipes will then undergo another bifurcation of angle β, forming tertiary pipes of diameter D_2 and length L_2, resulting in a N = 12 outlet network.

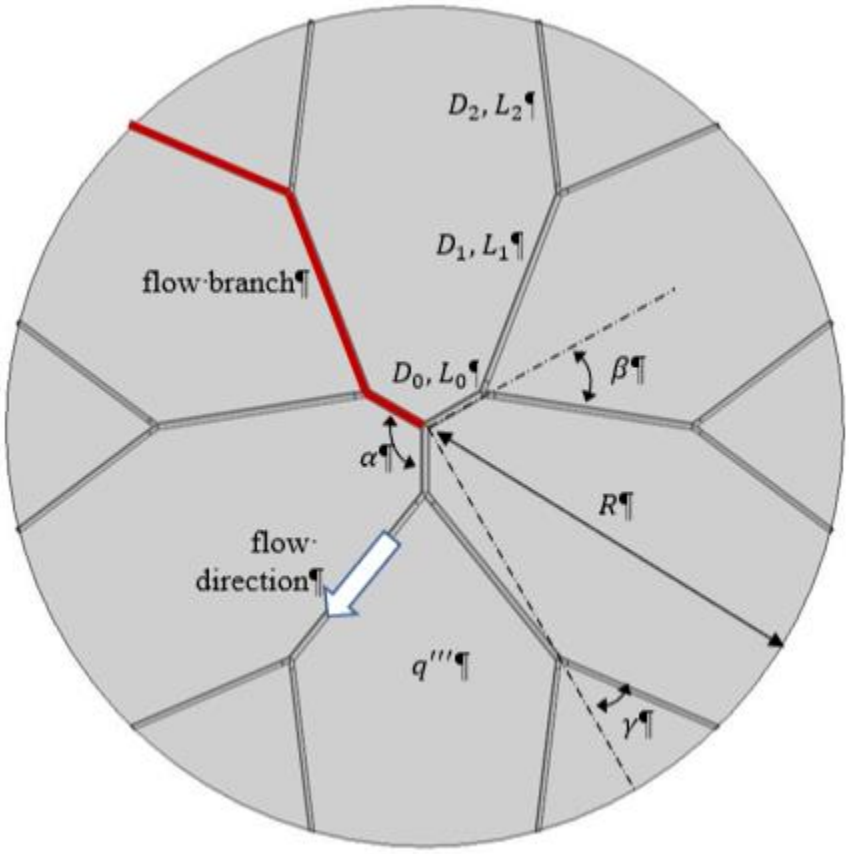

Figure 25.Two-level flow network for cooling a heat generating disc.

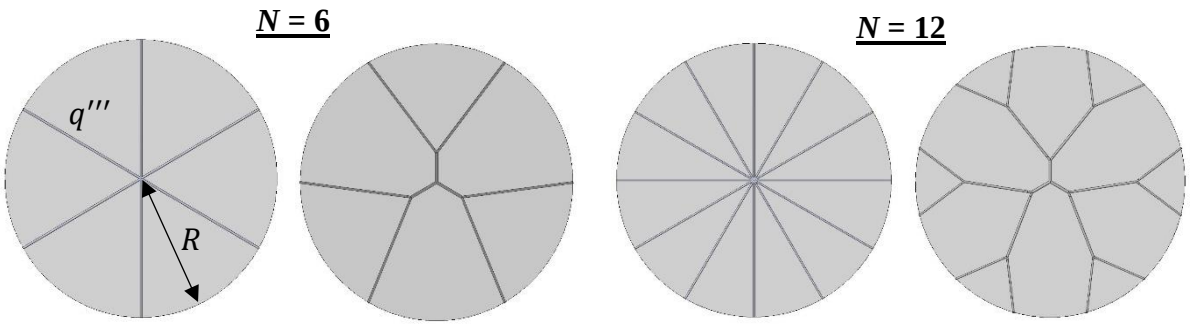

Figure 26. Radial and bifurcating flow networks, with N = 6 and N = 12, for cooling a heat generating solid disc.

Consideration is given here to the simplest network, the *radial* network, with either six (N = 6) or twelve (N = 12) outlets, as shown in Fig. 26. Notice these networks have the same number of center branches (for being radial), either six (n_0 = 6) or twelve (n_0 = 12). Also shown in Fig. 26 are the corresponding branched networks studied here, both with three center branches (n_0 = 3). Observe the first branched network, with N = 6, is a one-level bifurcating flow network, while the one for N = 12 is a two-level bifurcating flow network, shown also in Fig. 25.

The optimization of the flow network geometries for the configurations shown in Fig. 26 is obtained from [23]. Using the listed relations, and choosing a disc radius R = 254 mm, for instance, the primary dimensions obtained are shown in Table 2, including the primary diameter D_o and the length of the pipes for each bifurcating level, in the form $L_i^* = L_i/R$. The branching networks considered here have n_0 = 3 because this number of center pipes yields minimum total pressure drop for any bifurcating network [23].

The subsequent pipe diameters are obtained following [22], who, in a study of blood capillary networks, have shown there is an empirical relation observed for the optimal sizing of flow pipe diameter *D* across bifurcations, namely:

$$\frac{D_{i+1}}{D_i} = 2^{-\frac{1}{3}} \tag{8}$$

where *i* refers to the upstream (of the bifurcation) pipe, and (*i*+1) to the immediate downstream pipe. Notice for each flow branch in Fig. 25, the two-level bifurcating network, *i* = 0 refers to the pipes emanating from the center of the disc, and *i* = 2 refers to the pipes delivering the fluid to the disc periphery.

Table 2. Optimized dimensions for radial, single- and two-level bifurcation of Fig. 26.

N	*Configs.*	D_0 *[mm]*	n_0	L_0^*	L_1^*	L_2^*	f
6	*radial*	*3.94*	*6*	*1*	-	-	*6*
	one-bifurc.	*5.00*	*3*	*0.214*	*0.822*	-	*5.85*
12	*radial*	*2.79*	*12*	-	-	-	*12*
	two-bifurc.	*4.58*	*3*	*0.157*	*0.509*	*0.432*	*9.82*

Notice the total volume occupied by the fluid (the total pipe volume of the flow network) V is the summation of the individual pipe volumes, given by:

$$V = n_0 \sum_{i=0}^{p} 2^i \frac{\pi}{4} D_i^2 L_i \tag{9}$$

where p is the pipe section that touches the periphery (equal to the number of bifurcation by each flow branch from the center of the disc). With Eq. (9) and Table 2, and assuming a disc thickness equal to 6.35 mm (1/4 in), the calculated volume of the pipes in this case equals 1.86×10^{-5} m^3; this value is maintained fixed for all configurations. Observe the ratio of pipes volumes to disc volume ($V_D = 1.2870 \times 10^{-3}$ m^3) equals 0.0145, or 1.45 %.

Using the parameters from [15] and Eq. (8), one can reproduce the geometries using a CAD software. However, due to the size difference between D_i to D_{i+1} one must create a geometric transition at each bifurcation, which affects very slightly the total pipe volumes. This transition, however, is carefully done to guarantee all pipe volumes match to within 0.5 %.

An additional note is necessary about the construction of the flow networks, as indicated by [23]. From a practical standpoint, the pump power necessary to maintain the fluid flowing through the disc flow network is related to the volumetric (or mass, for an incompressible fluid) flow rate and the pressure loss ΔP along a flow branch, i.e., from the center of the disc to one of the peripheric outlets. It is convenient then to define a friction coefficient in terms of the flow rate through the disc, and the disc overall geometric characteristics, namely

$$f = \frac{\Delta P}{8\pi\nu\dot{m}} \frac{V^2}{R^3} \tag{10}$$

where $\dot{m} = \dot{m}_0 n_0$ is the total mass flow rate that enters the disc, with $\dot{m}_0 = \rho_f U_o A_0$ being the mass flow rate through each center emanating branch, ν and ρ_f are the fluid (considered Newtonian and incompressible) kinematic viscosity and density, U_0 is the cross-section averaged fluid speed and A_0 is the cross section area (uniform) of the center pipe, and n_0 is the number of pipes from

the disc center. Observe once a disc (with V and R), a fluid (with ρ and ν), and a flow rate entering the disc $\dot{m}$ are chosen, Eq. (10) yields a direct proportion between f and ΔP. This makes f a representative of the total pressure drop of the disc, and a comparable parameter between all flow configurations, as long as V, R, ρ_f, ν, and $\dot{m}$ are set.

In a simplified analysis [23], assuming the flow in each pipe of a flow branch laminar and fully developed and neglecting the bifurcating pressure losses, the minimization of the flow pressure drop yields f to be at most function of n_0, $f(n_0)$, because the individual friction factors through the pipes forming the branched path are dependent on each pipe length and volume (or diameter) only. In the case of a radial flow configuration, f equals n_0 and Eq. (10) recovers the known Hagen-Poiseuille relation between ΔP and $\dot{m}$. Expressions for $f(n_0)$ for the optimized bifurcating configurations were obtained by [23]. When the one-level bifurcation is considered, for instance, the expression for $f(n_0)$ becomes:

$$f(n_0) = n_0 \left(\left[cos\frac{\pi}{2n_0} + sin\frac{\pi}{2n_0} \left(\frac{2^{-1/3}}{sin\ \beta} - \frac{1}{tan\ \beta} \right) \right]^3 \right) \tag{11}$$

where, in the optimization process to minimize the network flow resistance ΔP, the bifurcation angle turns out to equal $\beta = 0.654$ rad (recall this is the first branching angle, Fig. 25), which does not depend on the angle α. Notice Eq. (11) indicates the smallest f is obtained for the minimum n_0, which equals 3 [23]. The corresponding f values for each of the four flow configurations considered here are included in Table 2.

Figure 27 [23] shows, for a fixed number of outlets N, fixed total pipe volume V and fixed disc radius R, the disc flow resistance, f, or the total pressure drop imposed to the inlet flow by a branch of the flow network. Notice the curves for the bifurcating configurations (pairings) start at

their minimum, i.e., when $n_0 = 3$ - e.g., the one-level bifurcation curve begins at $N = 6$. Observe for the radial network (no pairing) configuration, $f(n_0) = n_0 = N$, as shown in Fig. 27.

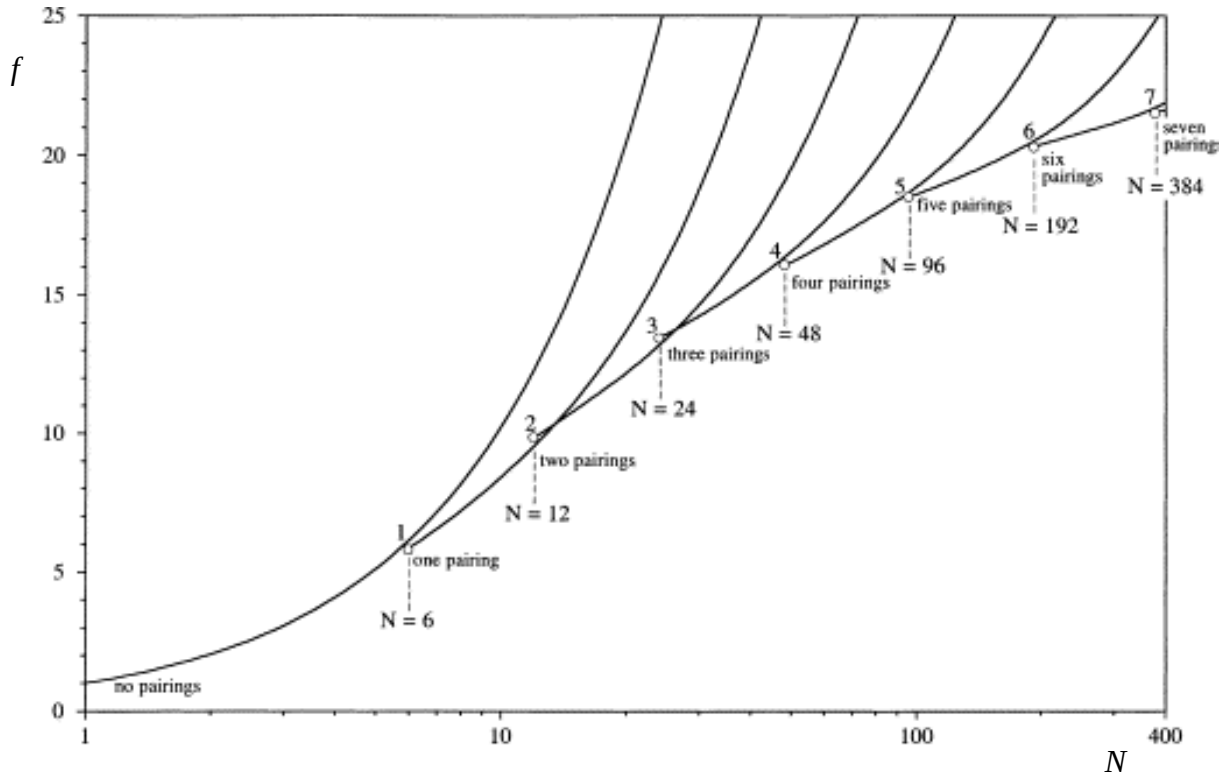

Figure 27. Effect of the number of bifurcations (pairings) on the disc flow resistance (f) as function of number of outlets N at the periphery of the disc [23].

Where a branching (pairing) curve begins, shown with a small circle in Fig. 27, the friction factor f for this branching is very similar to the f value of the preceding branching level; for instance, the two-level branching (two-pairings) begins when $N = 12$, and the f value for this network is very close to the f value for the preceding one-level branching. This means there is no preferred configuration between the two when it comes to total pressure drop, and this does not hold when comparing with one branching level. For instance, for the same $N = 12$ the figure shows

the radial flow configuration (no pairing curve) yielding a higher flow resistance *f* than any of the two branching alternatives.

Finally, the fully developed laminar flow assumption made in obtaining *f* shown in Fig. 27 and the neglect of the bifurcation losses, make *f* independent of the mass flow rate. This, and other aspects, are investigated in the following sections.

3.2 Mathematical Modeling and Numerical Simulations: Laminar Flow

The conjugate convection-diffusion problem resulting from using the flow networks to cool a heat generating solid disc is simulated numerically considering the 3D process at steady-state, with all fluid and solid properties being uniform and constant (i.e., incompressible and Newtonian fluid, homogeneous and isotropic solid and fluid), negligible viscous dissipation, and no body forces. The resulting system of mass, momentum, and energy conservation equations is:

$$\nabla . \boldsymbol{u} = 0 \tag{12}$$

$$\boldsymbol{u} . \nabla \boldsymbol{u} = -\frac{1}{\rho_f} \nabla P + \nu \nabla^2 \boldsymbol{u} \tag{13}$$

$$\boldsymbol{u} . \nabla T = \alpha_f \nabla^2 T \tag{14}$$

$$0 = k_s \nabla^2 T + q''' \tag{15}$$

where $\boldsymbol{u}$ is the local fluid velocity (inside the flow pipes), P is the local fluid pressure, ρ_f, ν, α_f are respectively the fluid density, kinematic viscosity, and thermal diffusivity, T is the temperature (of the fluid in the fluid energy equation Eq. (14), or of the solid in the solid energy equation Eq. (15)), k_s is the solid thermal conductivity and q''' is the volumetric heat generation rate in the solid region only.

Equations (12)-(15) are solved under boundary conditions of impermeable and non-slip solid surfaces ($\boldsymbol{u}$ = 0 along the solid-fluid interfaces), adiabatic ($\nabla T = 0$) top, bottom and side (except flow outlet) disc boundaries, uniform pressure P_p and $\partial T/\partial z = 0$ at any flow outlet (located at the periphery of the disc; equivalent to fully developed flow condition), uniform temperature T_0 at the flow inlet, and fully developed flow $\boldsymbol{u} = u_z(r)$ at any disc inlet branch. Also imposed are compatibility thermal conditions along the fluid-solid interfaces, namely $T_f = T_s$ and $k_s(\nabla T)_s = k_f(\nabla T)_f$, with *f* and *s* referring to solid and fluid and k_f being the fluid thermal conductivity.

Assuming the inlet flow as laminar, the axisymmetric and fully developed condition in each flow branch emanating from the center of the disc is:

$$u_z(r) = 2U_0\left[1 - \frac{r^2}{R_o^2}\right] \tag{16}$$

where $U_o = 4\dot{m}_0/(\rho\pi D_0^2)$, is the average fluid speed at the inlet branch, $R_0 = D_0/2$, is the radius of the inlet branch, r is the local radial coordinate in the circular pipe. The formulation is now complete. Before proceeding, the nondimensionalization of the formulation is performed by using as length scale the disc diameter $D = 2R$, and as speed scale the inlet average speed U_0. The pressure and temperature are nondimensionalized following:

$$P^* = \frac{P - P_p}{\rho U_0^2} \qquad , \qquad T^* = \frac{T - T_0}{\frac{q''' D^2}{k_f}} \tag{17}$$

With these nondimensionalizations, the balance equations Eqs. (12)-(15) then become:

$$\nabla^* . \boldsymbol{u}^* = 0 \tag{18}$$

$$\boldsymbol{u}^*.\nabla^*\boldsymbol{u}^* = -\nabla^* P^* + \left(\frac{n_0}{M}\right)\nabla^{*2}\boldsymbol{u}^* \tag{19}$$

$$\boldsymbol{u}^*.\nabla^* T^* = \left(\frac{n_0}{MPr}\right)\nabla^{*2} T^* \tag{20}$$

$$0 = \nabla^{*2} T^* + \frac{1}{k^*} \tag{21}$$

The ruling parameters emerging from the nondimensionalization process are the fluid Prandtl number, Pr = ν/α_f, the solid-fluid thermal conductivity ratio, $k^* = k_s/k_f$, the number of inlet branches n_0, and a nondimensional mass flow rate parameter,

$$M = \frac{4\dot{m}}{\mu\pi D} \tag{22}$$

Observe M relates directly to the Reynolds number in each flow branch at each bifurcation level i, namely Re_i (i = 0, 1, 2, … p) via:

$$Re_i = \frac{D}{D_i}\left(\frac{1}{2^i}\right)\left(\frac{M}{n_0}\right) \tag{23}$$

Equation (23) is useful because it allows for three important extensions, namely:

$$Re_0 = \frac{D}{D_0}\left(\frac{M}{n_0}\right) \tag{24}$$

$$\frac{Re_{Bi\_i}}{Re_{Rd}} = 2^{(p-i)}\frac{D_{Rad}}{D_i} \tag{25}$$

$$\frac{Re_i}{Re_{i-1}} = \frac{D_{i-1}}{2D_i} = 0.63 \tag{26}$$

The first Eq. (24) is valid for any network, either radial or bifurcating (observe each of these will have a different n_0). The second relation compares the Re of any bifurcating segment i of a p-level

bifurcation with the Re of the corresponding (with same total number of outlets N) radial configuration. Because $p \geq i$ and $D_{Rad} > D_i$, Eq. (25) anticipates $\mathrm{Re}_{Bi\_i} > \mathrm{Re}_{Rd}$. The last, Eq. (26), is valid for a bifurcating network only (for which more than one flow duct segment exists, and n_0 is a fixed number). Observe from Eq. (25) the flow branch with highest Re is the initial branch, namely Re_0 is the maximum Reynolds number in a bifurcating network, and this is the Re signaling potential transition from laminar to turbulent flow in the entire network.

A word of caution in relation to Eq. (24): hydraulic results in studies of flow bifurcation are usually presented in terms of the inlet Reynolds number, Re_0, e.g., [27]. This is certainly a trait inherited from classical fluid mechanics, where the predominant analysis of flow with average speed U_0 through a single, regular (un-bifurcating) duct of diameter D_0, results in $\mathrm{Re}_0 = \rho U_0 D_0/\mu$ being directly proportional to the mas flow rate, $\mathrm{Re}_0 = 4\,\dot{m}_0/(\mu\pi D_0)$. In bifurcating networks as the ones dealt with here, this relation still holds; however, when comparing for the same flow rate $\dot{m}_0$ the pressure drop of distinct networks, for instance with $N = 6$ radial and one-level bifurcating, the Re_0 values of each configuration will differ because their D_0 is different (Table 2). Hence, if one presents pressure drop results calculated at the same Re_0 value for both configurations, these two Re_0 will not refer to the same mass flow rate – this is like comparing *apples* with *oranges*! That is why in here all flow comparisons are done in terms of M, not Re_0.

The boundary and compatibility conditions for solving Eqs. (18-21) become: $\boldsymbol{u}^* = 0$ along the fluid-solid interfaces); adiabatic $\nabla T^* = 0$ top, bottom and side (except flow outlet) disc boundaries; $P^* = 0$ and $\partial T^*/\partial z^* = 0$ at the flow outlet; $T^* = 0$ and $\boldsymbol{u}^* = u^*_z(r^*) = 2[1-(r^{*2}/R_0^{*2})]$ at the flow inlet; and $T^*_f = T^*_s$ and $k^*\nabla \mathrm{T}^*_s = \nabla T^*_f$ along the fluid-solid interfaces.

The nondimensional balance equations, with boundary and compatibility conditions, are solved using a second-order accurate finite-volume method to find the fluid velocity and temperature fields in the fluid and solid regions of the disc. Due to symmetry, the thermo-hydraulic simulations of each of the four configurations (Fig. 26) are restricted to four disc sectors, with symmetry conditions in T^* at their radial solid boundaries. These 3D sectors are covered with an unstructured mesh in the solid and fluid regions, as shown in Fig. 28, with grid refinement near the solid-fluid interfaces and near the flow inlet and outlet. Notice the mesh density is much increased in the pipe network to accurately capture the flow (pressure-velocity and temperature) variations and the variations caused when the fluid pass through any of the bifurcations along the network.

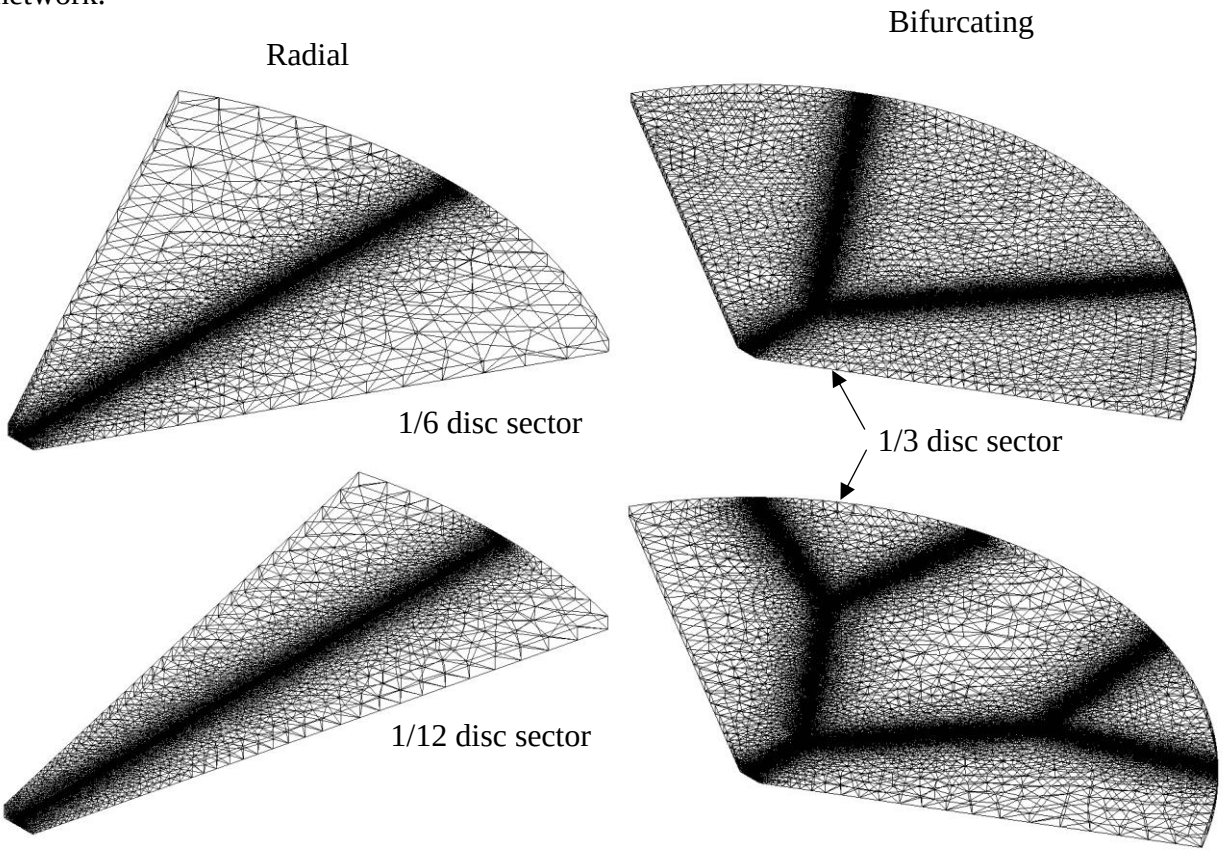

Figure 28. Sample computational meshes for N = 6 (top) and N = 12 (bottom) disc sectors for simulating configurations shown in Fig. 26.

Grid sensitivity analyses are thoroughly investigated, particularly for the most stringent cases (i.e., highest fluid speed, pressure and temperature gradients) of each network configuration. Pressure loss and maximum temperature results presented here are within 0.5% of the equivalent results obtained with a grid having double the grid density. The mesh quality is checked by comparing the resulting nondimensional total pressure drop of the two radial flow configurations (for N = 6 and 12) with the theoretical predictions from the Hagen-Poiseuille equation, for several different nondimensional flow rate M values. The pressure drop results are recast in the form of f, Eq.(10), using the P^* definition Eq. (17), for being more representative as a comparison parameter,

$$f = \left(\frac{1}{2\pi^2 \nu}\frac{V^2}{R^3}\frac{U_0}{D_0^2}\right) P_0^* \tag{27}$$

As shown in Figure 29, the numerical results fall within less than 2.5 % of the equivalent theoretical predictions. The results for the bifurcating configurations can be validated in a similar manner using the prediction by [23] when the bifurcating effects are negligible. Otherwise, there is no way to validate the results because no theoretical prediction or experimental measurements exists for the pressure loss across bifurcations identical to the ones used here.

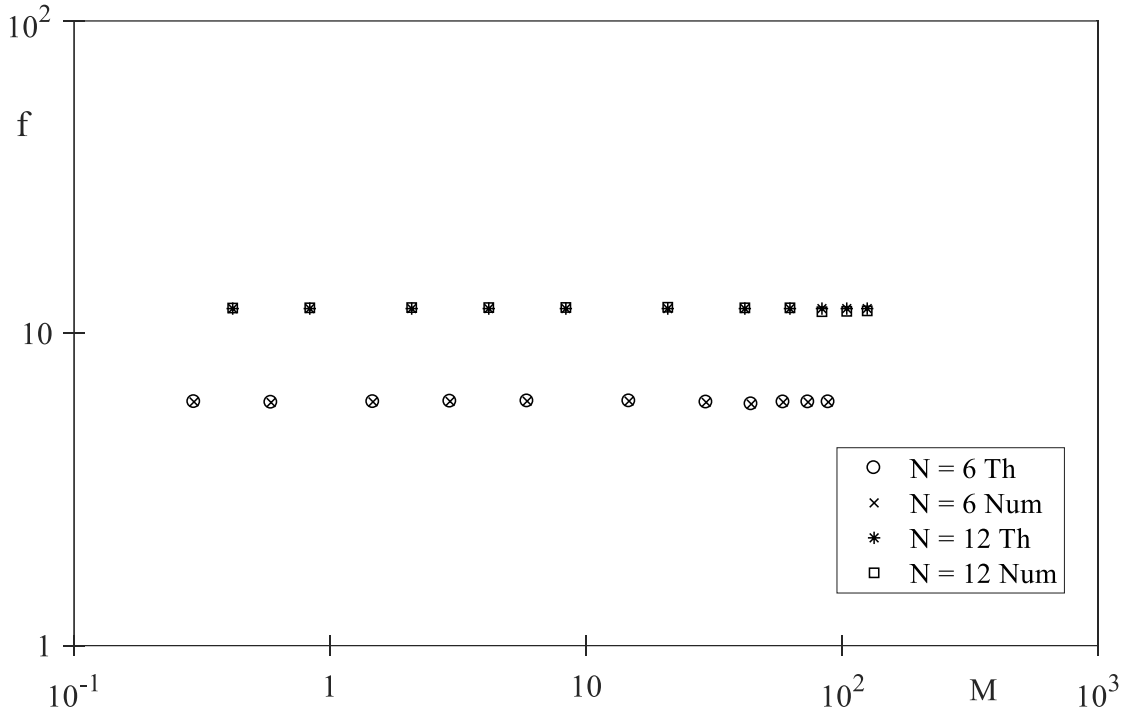

Figure 29. Total nondimensional branch pressure-drop comparison between numerical (Num) results and theoretical (Th) predictions for radial configuration with N = 6 and 12.

Numerical simulations are performed for Pr = 7 (water) and M varying from 0.2 to 130, which is equivalent to Reynolds number at the inlet branch, Re_0 (for radial or first branch of bifurcating network, with D_0 and L_0) varying from a minimum of 6 (for the N = 12 and radial configuration) to a maximum of about 4,800 (for N = 12 and two-level bifurcation configuration) – see Eq. (24) and Table 2 the values vary a little with the flow configuration and N chosen. It is worth recalling Re_0 is the highest Reynolds in any branch of a bifurcating network, Eq. (26). Results are also sought for five different k^* = 1, 4, 18, 63, 260. There is a total of about 220 different simulated cases (55 for each network configuration).

Of interest to evaluate the hydraulic performance of the cold plate is the parameter f, Eq. (27), and to evaluate the thermal performance is the maximum temperature within the domain T_m^*,

$$T_m^* = \frac{T_m - T_0}{\frac{q''' D^2}{k_f}} \tag{28}$$

The best configuration among the four studied in this work should present the lowest flow resistance and lowest thermal resistance, or equivalently the lowest f and T_m^*.

Also of interest is the Nusselt number of the branch convective flow from the origin towards the periphery of the disc, defined by:

$$Nu = \frac{-q''}{\left(T_0 - T_{f\_m}\right)} \frac{D}{k_f} \tag{29}$$

where q'' is the average heat flux crossing the solid-fluid interface of the network, namely:

$$q'' = \frac{q''' V_s}{A_d} \tag{30}$$

with V_s being the solid total volume and A_d the total solid-fluid interface surface area of the flow network, and T_{f_m} being the maximum temperature recorded in the fluid region (note this is not the bulk fluid temperature), likely registered at the solid-fluid interface at the outlet of the flow. In this sense, the Nusselt number tells the extent to which the fluid flow is effective in removing the heat generated from the solid.

A note about the pressure loss caused by the bifurcations becomes important. According to [26], it is possible to show bifurcation losses have a sizeable effect when optimizing the geometry of flow channels when $Sv^2 < 10$, which happens when the flow segments along a branch are thick (not slender), where Sv is the svelteness, a global property of the flow branch defined as:

$$Sv = \frac{(\sum_{i=0}^{N} L_i)}{V^{1/3}} \tag{31}$$

with $(\sum_{i=0}^{N} L_i)$ being the total length of ducts from the center to the periphery of the disc and V being the total duct volume. In the present work, the svelteness of the bifurcation configurations is Sv = 9.9 for the one-level and Sv = 10.5 for the two-level; therefore, $Sv^2 < 10$ is not satisfied by either configuration. Hence, significant bifurcation losses are not expected, and the pressure losses of the bifurcating cases should be similar to those of the radial flow.

3.3 Results and Discussions

3.3.1 Fluid Flow Resistance

Figure 30 presents some velocity and pressure distribution for radial configuration with N = 6, and with M = 0.35. Recall the inlet flow is set as fully developed, so the velocity profile is not to change throughout the duct and the pressure drop should equal a constant.

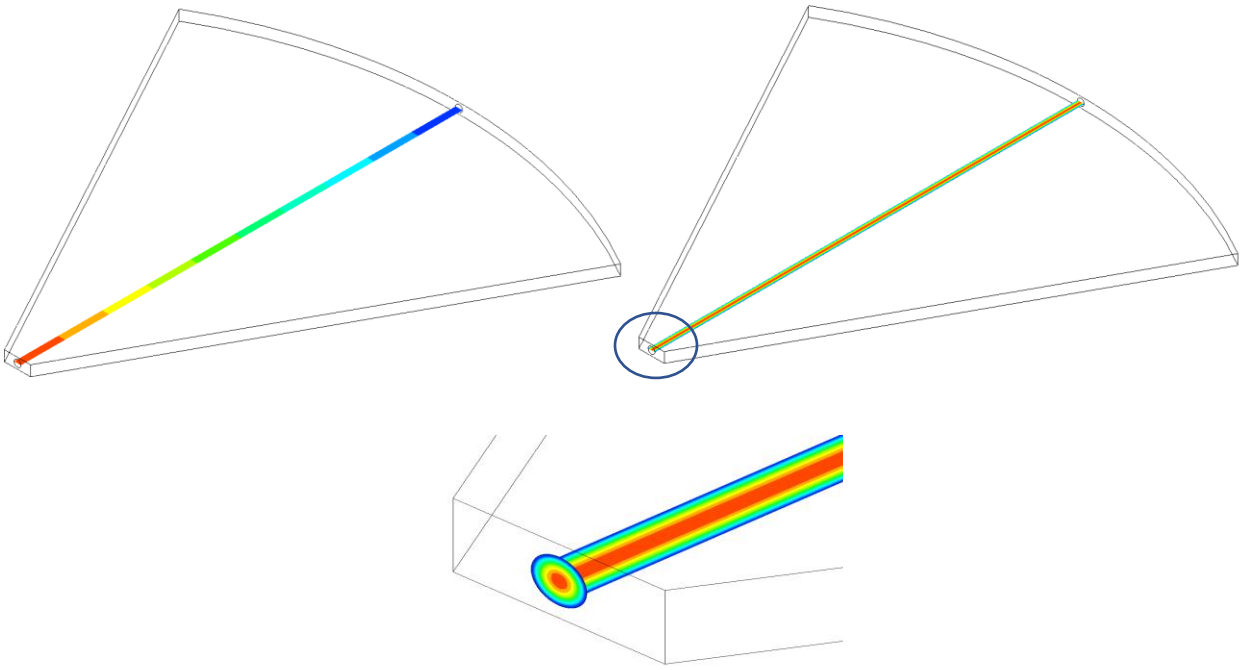

Figure 30.Velocity and pressure distribution for radial flow with N = 6 and M = 100.

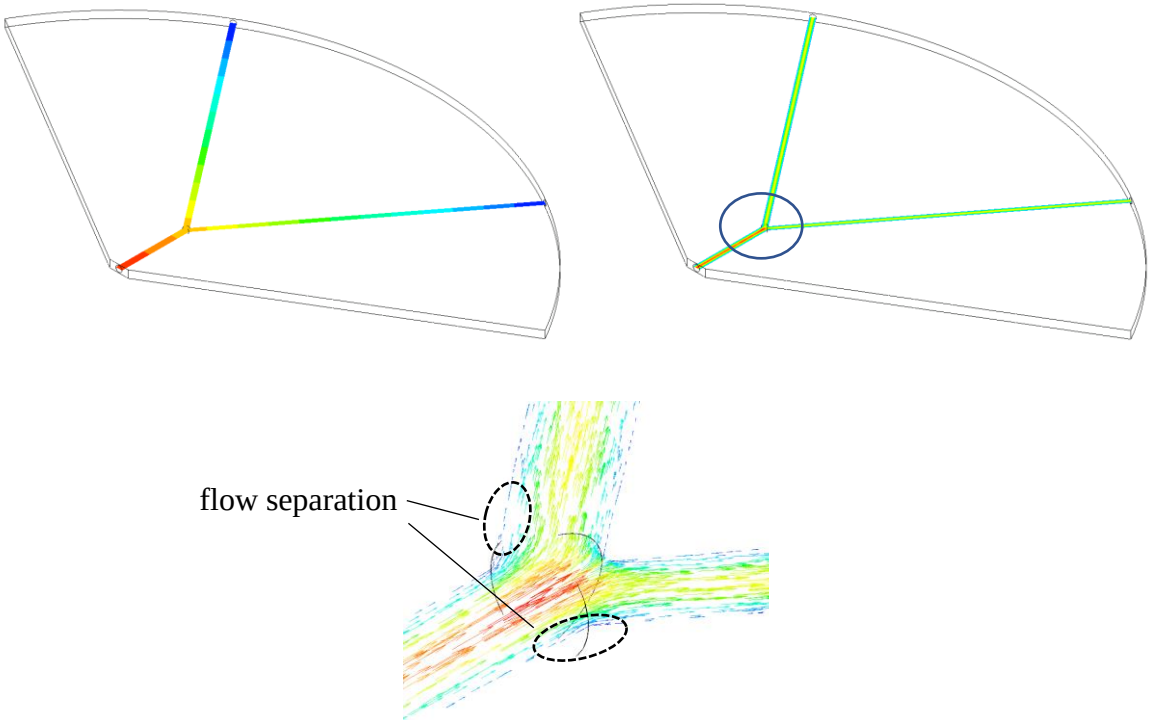

Figure 31.Velocity and pressure distribution for one-level bifurcation flow network with N = 6 and M = 100.

Figure 31 shows the velocity and pressure distributions for the one-level bifurcated flow network, with N = 6 and M = 100 as well. The small inset shows the velocity vectors across the bifurcation. There is flow separation right pass the bifurcation, where a small recirculating flow cell can be seen in each side on the outer surface of the duct (shown in the inset).

Figure 32 shows the total pressure drop results, in terms of f, versus the nondimensional mass flow rate M, for the two configurations with N = 6, namely the radial and the one-bifurcation network. Noticeable, the pressure loss for both configurations is almost identical until M is about 10, beyond which they diverge.

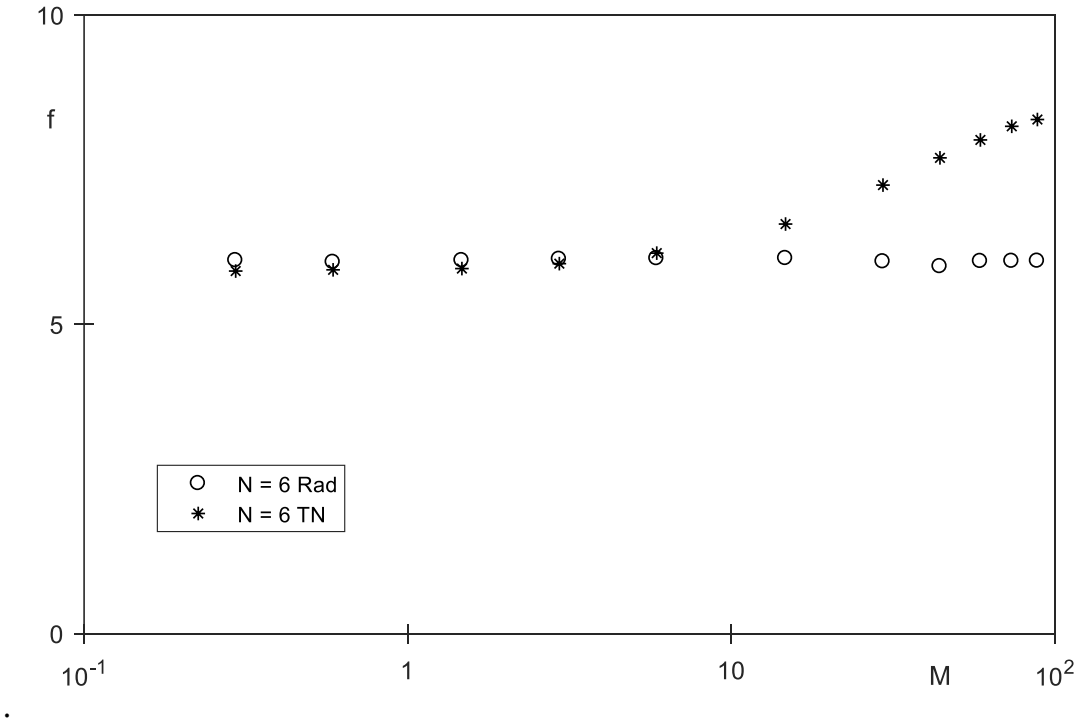

Figure 32. Dimensionless flow resistance f versus M for N = 6 and radial (Rad) and one-level bifurcation network (TN) configurations.

When M > 8, the bifurcated geometry starts to yield higher pressure losses. This result seems contrary to the conclusion by [23], in which the dimensionless flow resistance f should be

a constant in the laminar range (with $N = 6$, $f = 6$ for radial and $f = 5.849$ for bifurcating – note the theoretical predictions by [23] are verified by the numerical results) if $Sv^2 > 10$. However, for the current bifurcating networks $Sv^2 > 10$, and the dimensionless flow resistance of the bifurcating network increases, surpassing the radial pressure drop when $M > 8$, as the local pressure loss imposed by the bifurcations becomes a significant component to the total pressure loss. The radial flow configuration, as expected, keeps a constant flow resistance for the entire M-range.

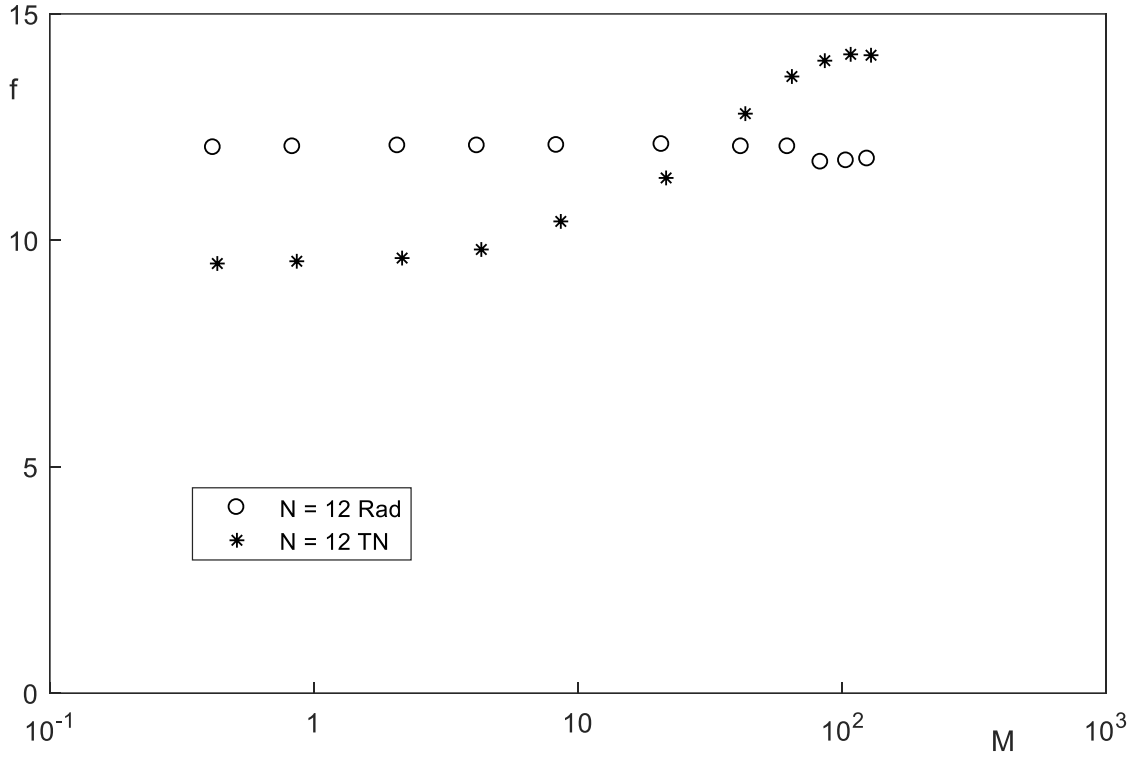

Figure 33. Dimensionless flow resistance f versus M for $N = 12$ and radial (Rad) and two-level bifurcation network (TN) configurations.

Similar observations can be made for the configurations with $N = 12$, as seen in Fig. 33. According to [23], the dimensionless flow resistance f should be a constant in the laminar range (for $N = 12$, $f = 12$ for radial and $f = 9.82$ for bifurcating – again, this theoretical prediction is

validated by the numerical results). As seen in Fig. 33, however, the pressure loss in the bifurcating network departs from the constant value when $M > 3$, eventually surpassing the pressure drop of the radial network when M ~ 30.

Results presented in Figs. 32 and 33 highlight an important conclusion: to answer what is the best configuration in terms of flow resistance, one should first ask the range of Re the configuration will work under, simply because the pressure loss imposed by bifurcations becomes increasingly important as the flow rate increases (or, as the Reynolds number increases).

Figure 34 summarizes the flow resistance results using the f_{TN}/f_{Rad} ratio, where f_{TN} is the friction factor for the bifurcating configuration and f_{Rad} is for the radial configuration, which is equivalent to $\Delta P_{TN}/\Delta P_{Rad}$ (Eq.(10)). Hence, results above 1.0 means the radial configuration yields lower flow resistance compared to its equivalent bifurcating network configuration. From Fig. 34, for M > 100 the radial configurations yield the best performance and for M < 100 the bifurcating networks are preferred.

Also noticeable from Fig. 34 is the flipping, around 1.0, of the pressure-loss ratio of $N = 6$ and 12 as M increases. Before $M \sim 10$ the radial and bifurcating networks with $N = 6$ show a closer pressure-drop than with $N = 12$. The reverse is true when M grows beyond 10. This is a result of the two bifurcation levels in the $N = 12$ network yielding a substantial gain in pressure drop when the dominant pressure drop effect is that of the longitudinal flow in each pipe. This also causes a small delay, for $N = 12$, in the M value (~ 30) for which the loss caused by the bifurcations overcome the segment losses, as compared to $M \sim 8$ for the $N = 6$ cases.

One should keep in mind there should be no comparison in terms of flow resistance between $N = 6$ and $N = 12$ networks. As the total pipe volume is constant for all geometries, $N = 6$ will always present lower pressure loss than that of $N = 12$.

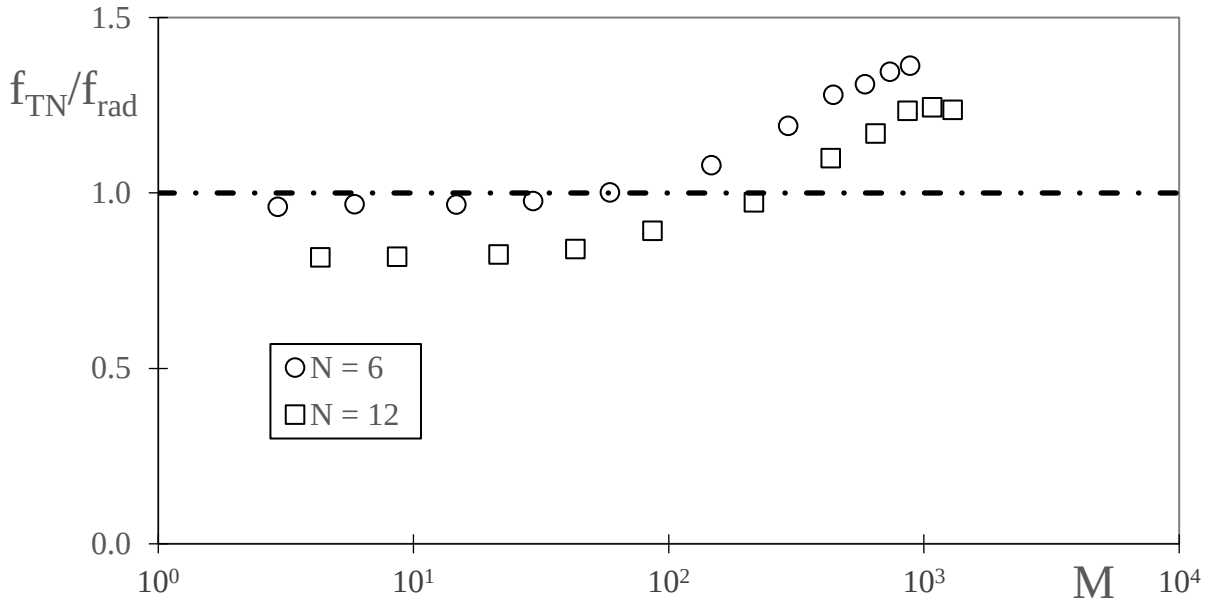

Figure 34. Dimensionless flow resistance ratio.

Noteworthy, the results presented here agree with Figure 27 curves for low Re numbers only. Therefore, in the present case, there is a mass flow dependency on the dimensionless flow resistance even for svelteness values $Sv^2 > 10$.

3.3.2 Thermal Resistance

Figure 35 shows the solid and liquid nondimensional temperature distribution in the mid-plane of the disc for $N = 6$ and one-level bifurcating configuration with M = 0.35 for the case k^*

= 1 (same solid and fluid thermal conductivity). The fluid temperature is zero at the origin and warms up as it moves towards the rim of the disc, as expected. The three solid hot spots (maximum temperature) are located furthest from the flow ducts near the periphery of the disc.

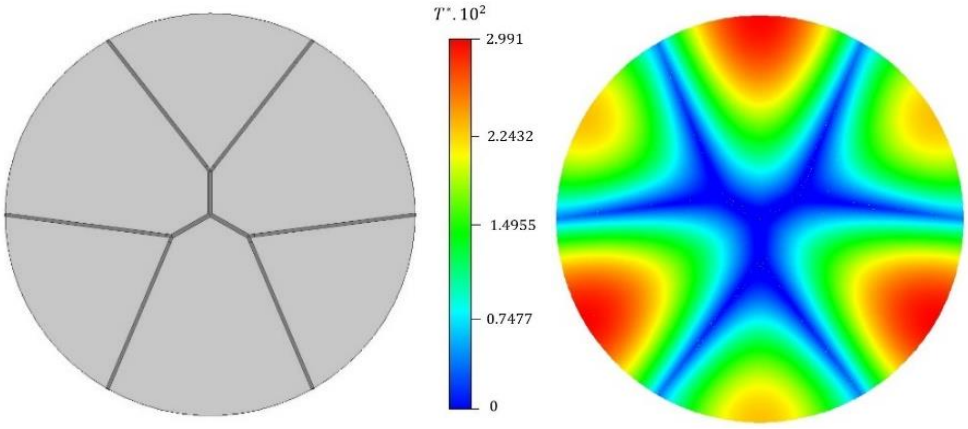

Figure 35. Disc mid-plane nondimensional temperature distribution (equivalent thermal resistance) for N = 6, M = 0.35, one-level bifurcation configuration with k^* = 1.

As the mass flow M increases, the maximum temperature T_m^* is expected to decrease for a given k^* and configuration. The results presented in Figure 36 confirm this expectation for the radial flow configuration case, N = 6 and k^* from 1 to 260.

Noticeable in Fig. 36 is the very small flow rate effect in the maximum temperature when k^* = 1. Recalling this is a conjugate heat transfer process, this result is a consequence of the high thermal resistance offered by the solid region to the heat transfer process, even when the solid and fluid thermal conductivities are equal, holding the convective effect in the ducts irrelevant for the overall cooling of the disc.

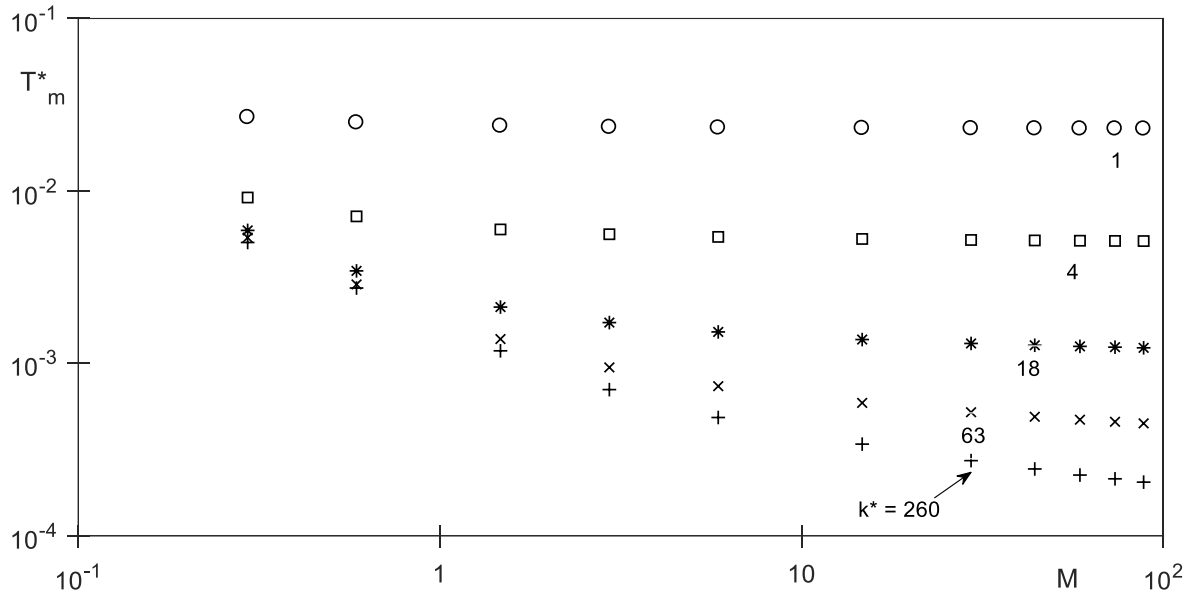

Figure 36. Nondimensional maximum temperature in the disc versus nondimensional mass flow rate, for radial configuration with $N = 6$ and several k^*.

As the solid-fluid thermal conductivity ratio increases beyond 1, the convective effect becomes progressively more evident as the conduction thermal resistance decreases in relation to the convective thermal resistance. Figure 36 shows this trend very clearly. Notice the variation in T_m^* gets progressively reduced as k^* grows beyond 18. Also evident is the limitation in the effect of increasing M: as M grows beyond about 10, the changes in T_m^* with M tend to flatten out.

A similar graph is shown in Figure 37, in this case also for $N = 6$ but with a one-level bifurcation network. As can be seen, the results in Figs. 36 and 37 seem very similar for both configurations.

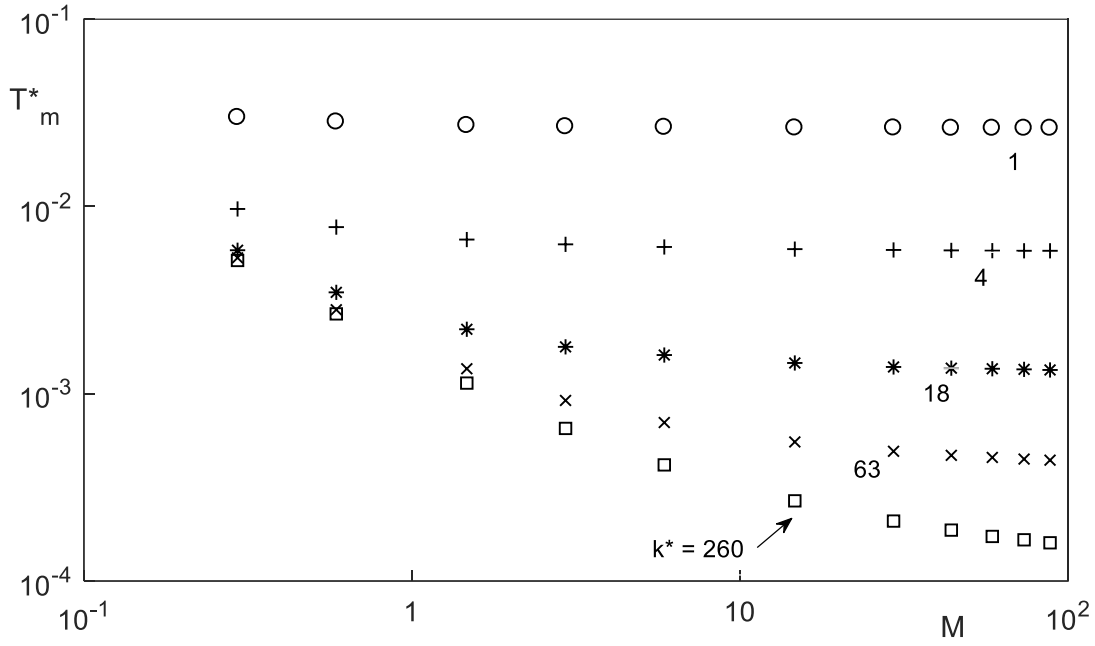

Figure 37. Nondimensional maximum temperature in the disc versus nondimensional mass flow rate, for one-level bifurcating configuration with $N = 6$ and several k^*.

Figures 38 and 39 show the nondimensional maximum temperature for the radial and bifurcated flow configurations with $N = 12$. The results are very similar to the results for the N = 6 cases. In all cases, the best thermal performance in terms of minimum maximum temperature is obtained when $k^* = 260$, as expected.

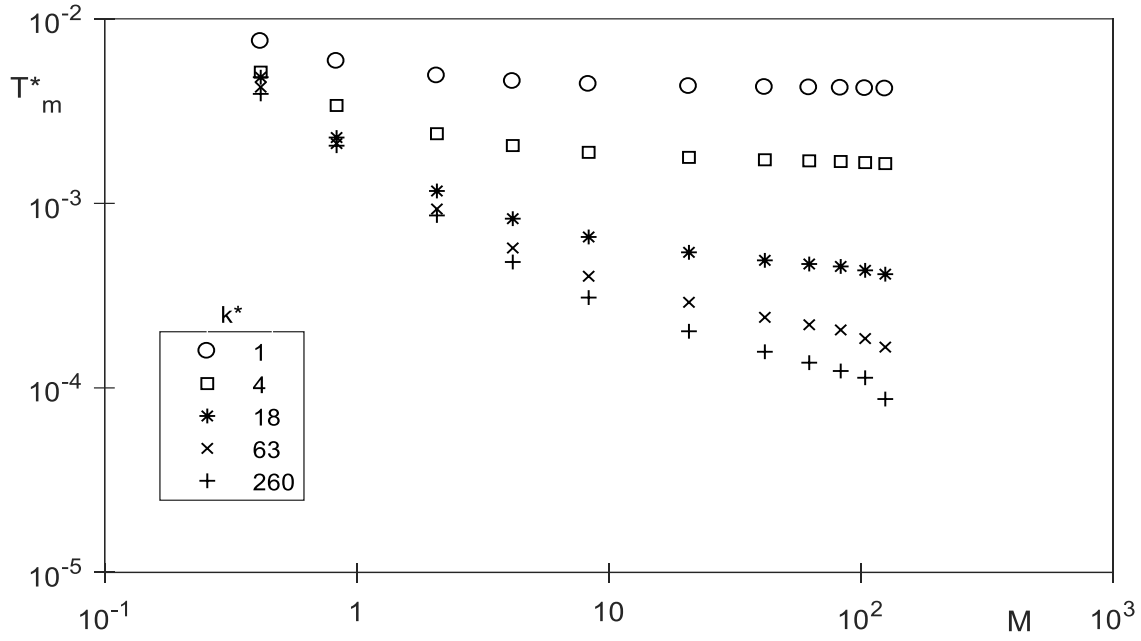

Figure 38. Nondimensional maximum temperature in the disc versus nondimensional mass flow rate, for radial configuration with N = 12 and several k^*.

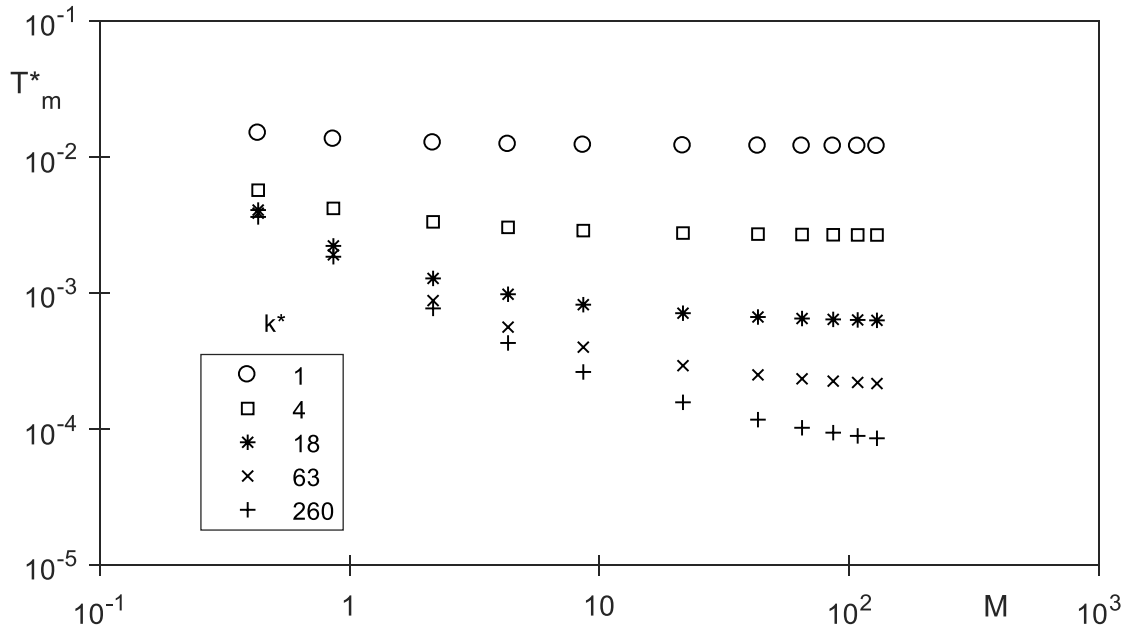

Figure 39. Nondimensional maximum temperature in the disc versus nondimensional mass flow rate, for two-level bifurcating configuration with N = 12 and several k^*.

The thermal performances of the radial and bifurcating networks, with N = 6 and 12, are compared in Fig. 40, in terms of T_m^* for k* = 260. Recall this case yields the smallest diffusion resistance (for k_s being much higher than k_f) of all cases. An initial observation, common to both N cases, is that when M is small (less than about 3) the radial networks seem to yield slightly better thermal performance than the bifurcating ones, in line with [15].

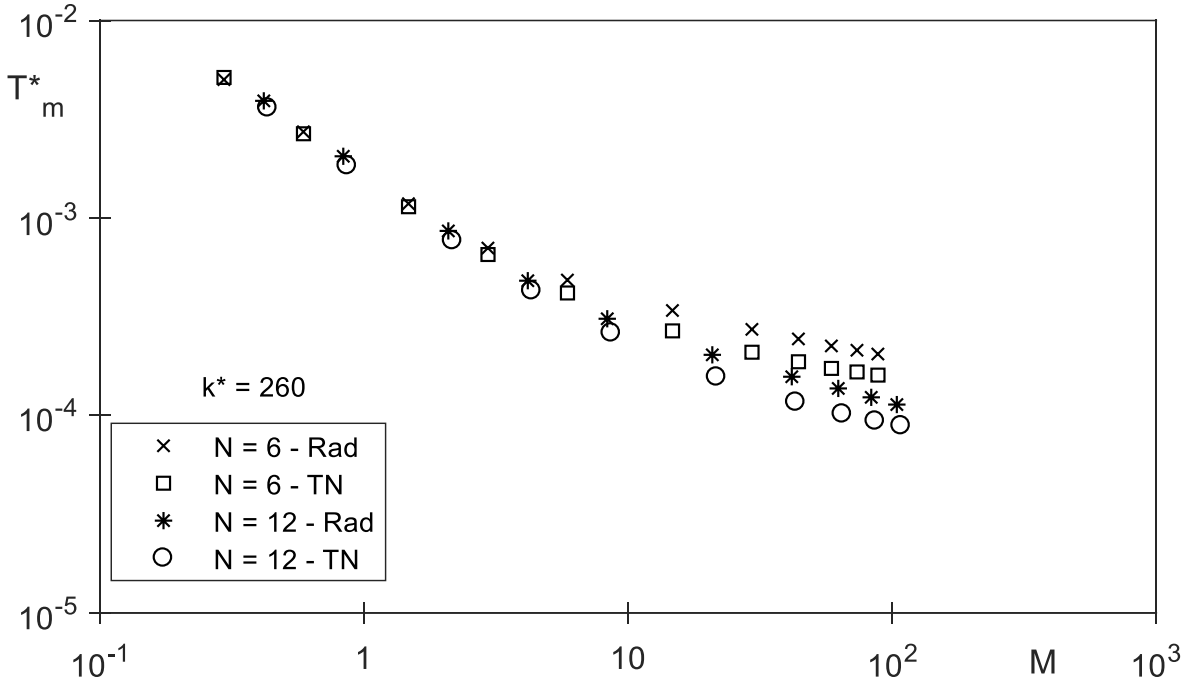

Figure 40. Nondimensional maximum temperature in the disc versus nondimensional mass flow rate, for radial and bifurcating configuration, N = 6 and 12, with k^* = 260.

However, as M increases past 3, the performance of the two networks flips, with the bifurcating networks yielding better results, with smaller T_m^*, than their radial counterparts. This is likely a result of the extra mixing induced in the convective flow by the bifurcations, an effect known to increase as M increases. Hence, the more bifurcations a network branch has, the better

the overall mixing effect will be. Indeed, the bifurcating network with N = 12 (two bifurcations for every channel leaving the center of the disk) leads to better thermal performance than the bifurcating network with N = 6 (only one bifurcation). This effect is less predominant when small k^* values are considered, because convection is less effective in this case (because of the strong conduction resistance by the solid).

Figure 41 shows the nondimensional temperature distribution in the mid-plane of the disc for M = 100 and k^* = 260. These temperature distributions correspond to the limit of the laminar range. It is clearly seen the two-level network with N = 12 provides a much better and more uniform cooling of the disc than any of the other three alternatives. This is a manifestation of the better access to the flowing heat provided by the two-level bifurcating configuration in this case. Interestingly, the access in question is the one provided by the convection ducts, and their access is effective only when the diffusion resistance by the solid is small, otherwise their effect becomes hindered – i.e., to access the ducts, the heat must flow to them first through the solid. Again, the highest nondimensional temperature of the disc happens at a point along the periphery equidistant to two consecutive and furthest outlet ducts in all cases.

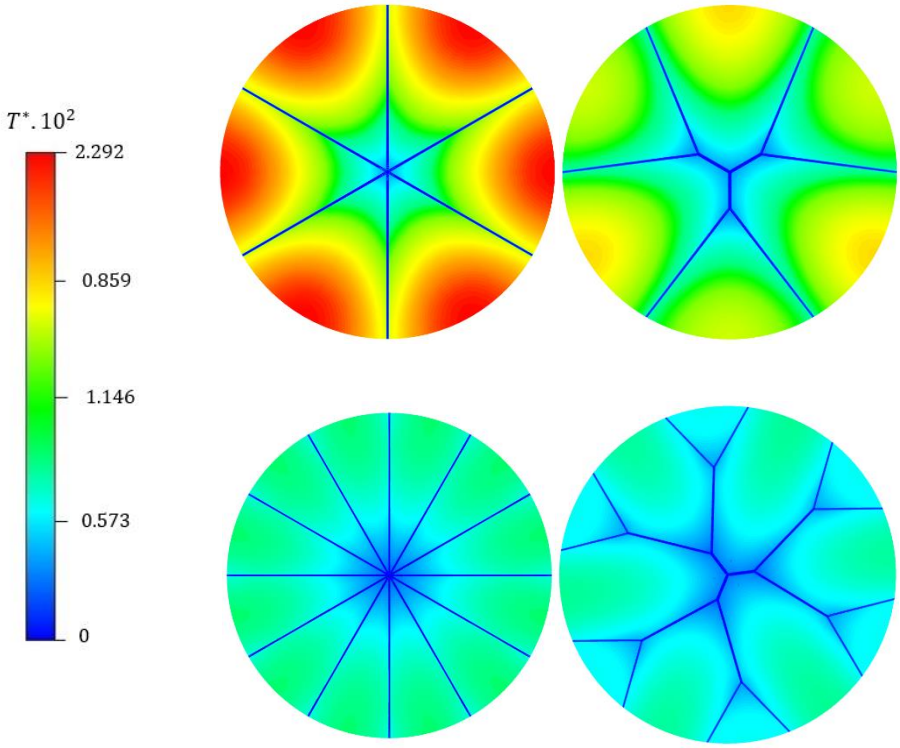

Figure 41. Disc mid-plane nondimensional temperature distribution for radial and bifurcating cases, with M = 100 and k^* = 260.

At the opposite extreme of the conductivity spectrum, the case with k^* = 1 is shown in Figure 42 for all flow configurations. Now, an increase in M does not yield much variation in $T_m{}^*$. Clearly seen in the graph is the best thermal performance by the radial configurations, with the one for N = 12 leading the pack. With this low k^*, the bifurcations always hinder the cooling performance as their geometry increases the diffusion thermal resistance of the solid.

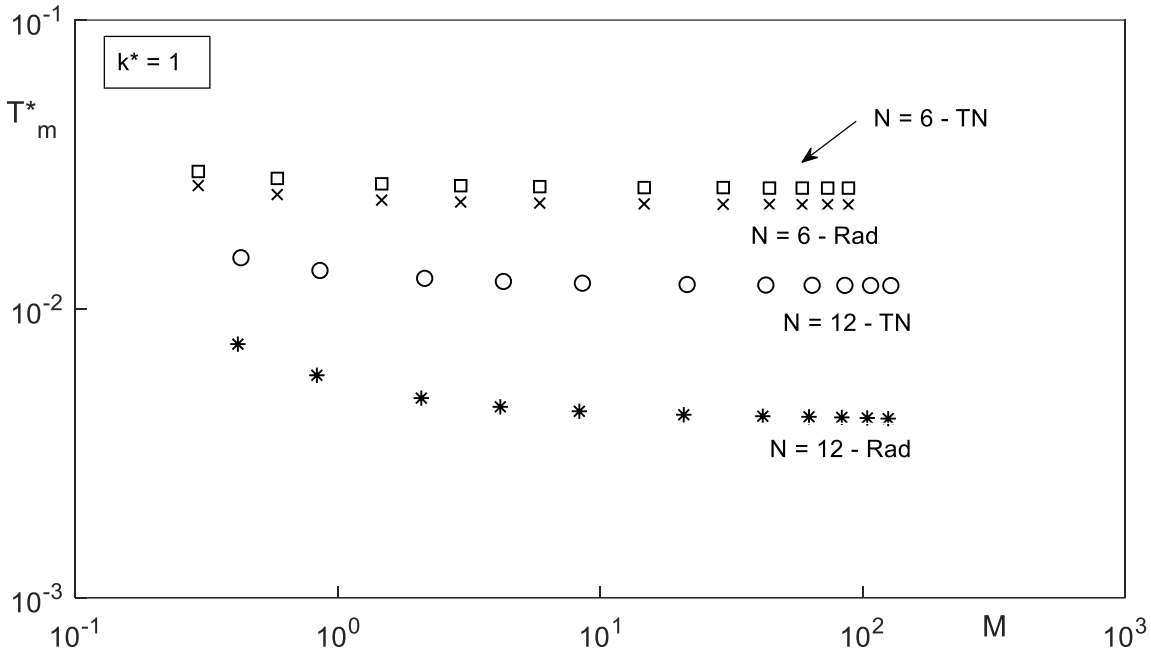

Figure 42. Nondimensional maximum temperature in the disc versus nondimensional mass flow rate, for radial and bifurcating configuration, N = 6 and 12, with k^* = 1.

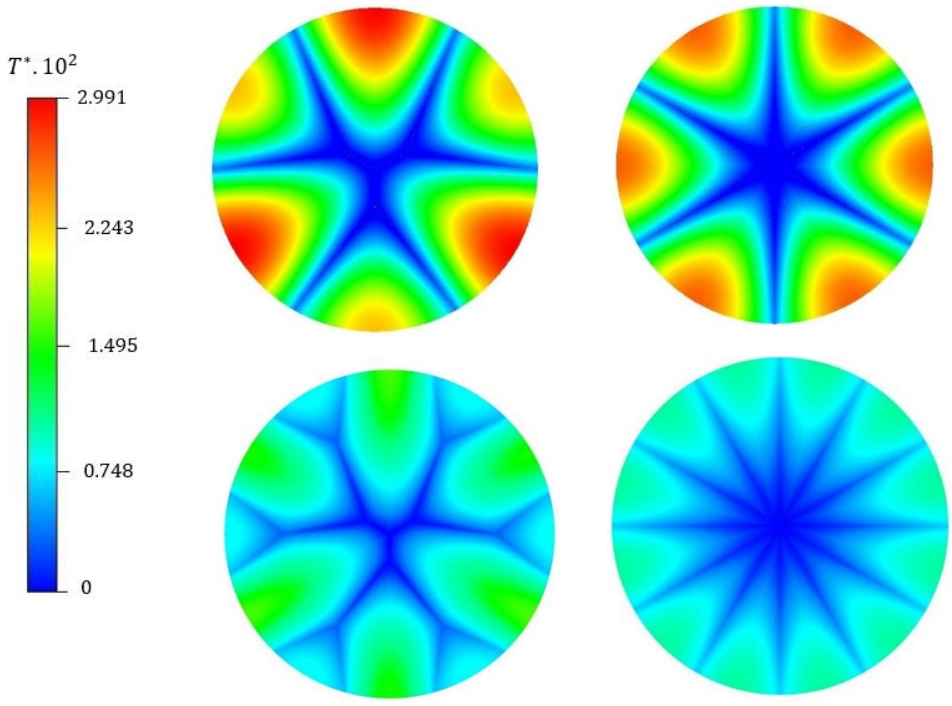

Figure 43. Disc mid-plane nondimensional temperature distribution for radial and bifurcating cases, N = 6 and 12, with M = 0.35 and k^* = 1.

Figure 43 shows the non-dimension temperature distribution for all four geometries, with M = 0.02 and k^*= 1. Clearly seen, for k^* = 1, the radial distribution covers more of the solid region, improving the thermal diffusion resistance of the solid region, then leading to a better overall cooling. The opposite happens when the bifurcating configurations are pursued.

Finally, the visual effect on the mid-plane nondimensional temperature distribution of the disc by changing k^* is shown in Figure 44, for the two-level bifurcating network, N = 12, and M = 0.35. With the same network, increasing k^* facilitates the generated heat of the solid to reach the convective branches, allowing the convection transport to carry the heat away as efficiently as possible.

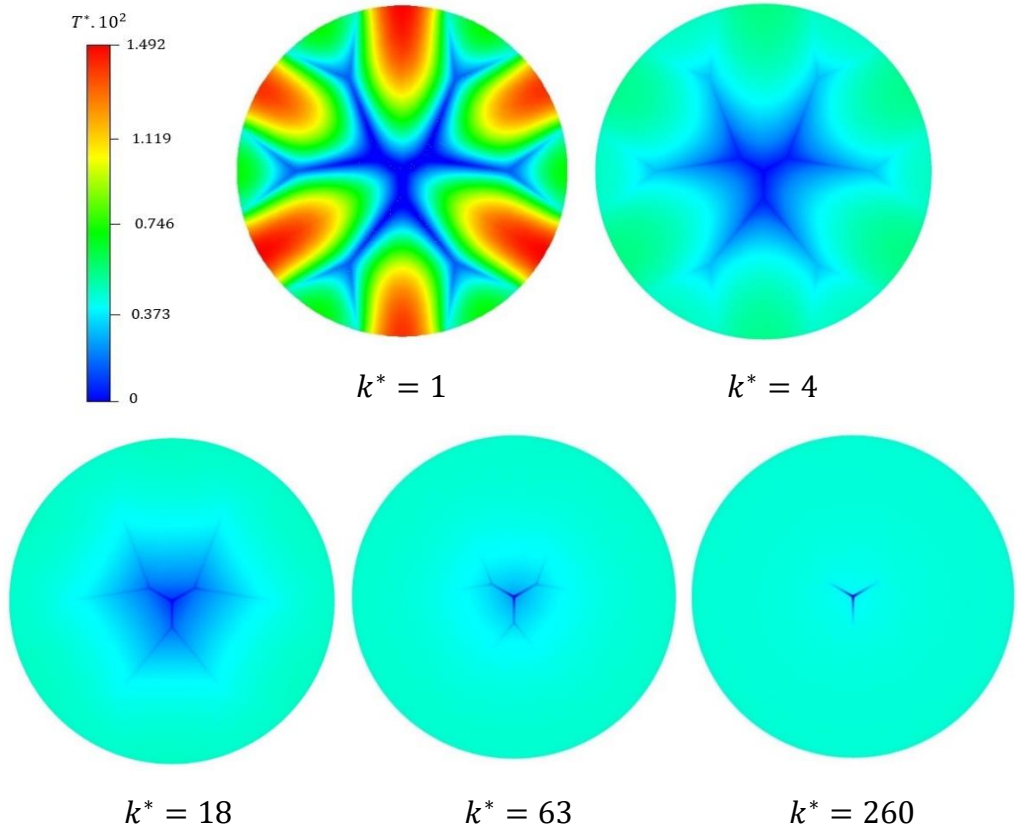

Figure 44. Disc mid-plane nondimensional temperature distribution for the two-level bifurcating configuration, N = 12, with M = 0.35 and several k^* values.

3.3.3 Convective Heat Transfer

Equation (29) shows that the Nusselt number increases as $T_{f\_m} \rightarrow T_0$. Therefore, high Nusselt Numbers are the main objective when the target is to remove the dissipated heat from the disc with minimum fluid temperature increase.

Results for Nu are shown in Fig. 45 for N = 6 configuration cases and k^* = 1 and 260. As M increases, or the mass flow rate through the disc increases, all Nu increase, as expected. Also expected in the increase in Nu as k* increases. Noticeable is the small effect k^* has on Nu when M is smaller than 1, in which case all configurations yield about the same Nu. At this low M level, the convection effect of the network is hindered, and the conduction thermal resistance in the solid region is expected to prevail, as the results show. The differences between the configurations becomes more evident as k^* increases beyond 1, in which case an increase in k^* leads to a stronger convective effect on Nu. Note the M effect differs slightly between the radial and the bifurcating configurations: the curving of the Nu evolution as M approaches 100 is more accentuated in the radial cases. Therefore, the bifurcating Nu with k^* = 1 overcomes the Nu for radial with k^* = 260. From all cases, the bifurcating configurations yield better thermal performance than their radial counterparts in the entire M range considered.

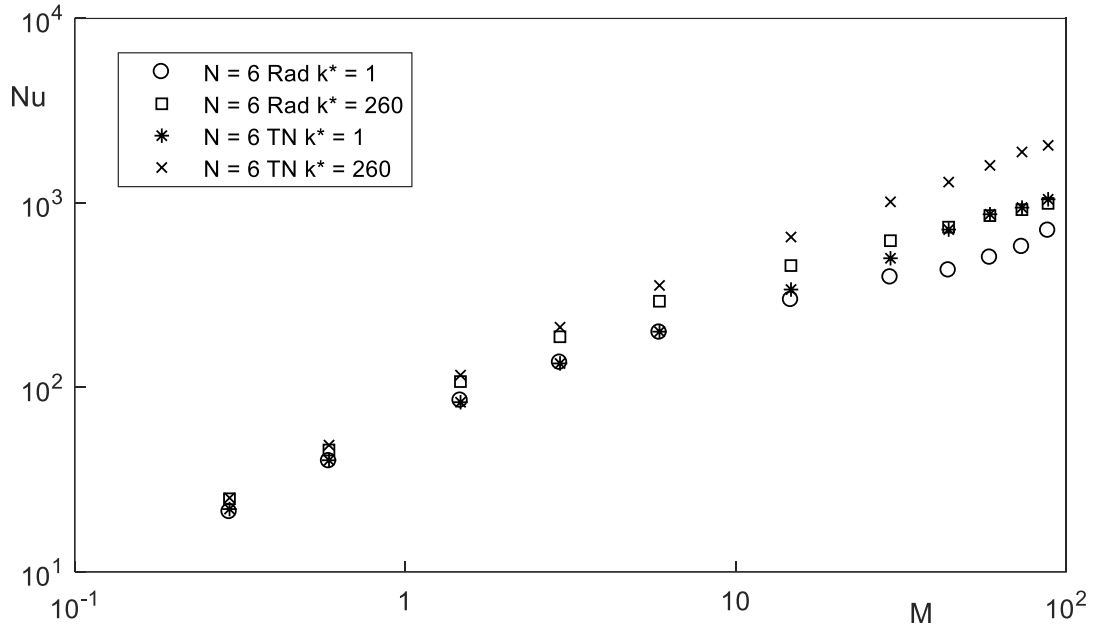

Figure 45. Nusselt number versus M, for N = 6, and k^* = 1 and 260.

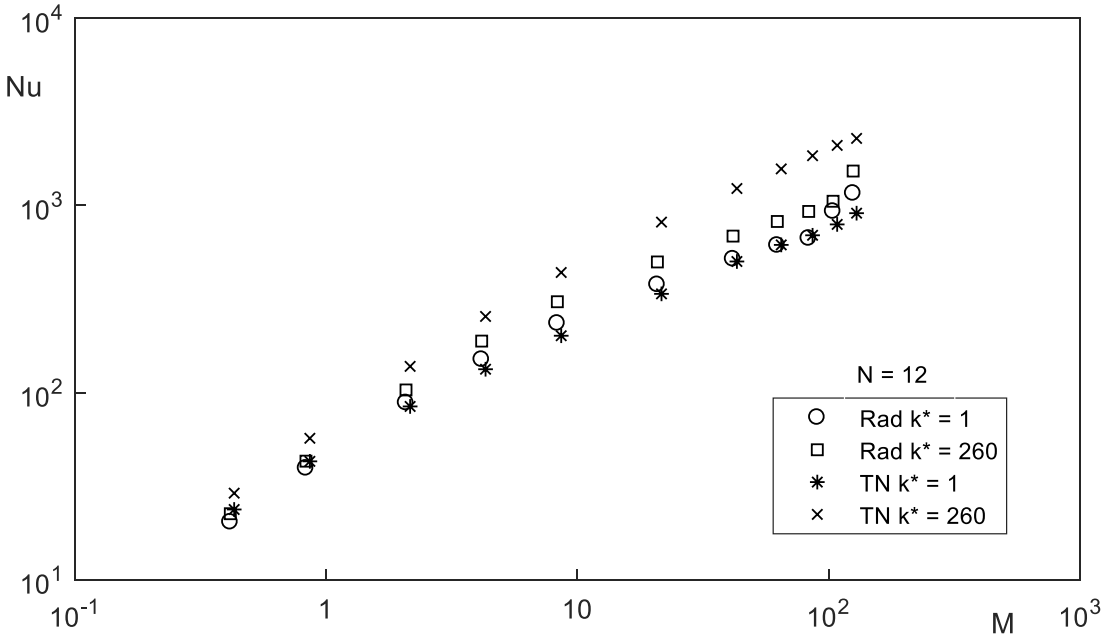

Figure 46. Nusselt number versus M, for N = 12, and k^* = 1 and 260.

A similar behavior is observed for the case N = 12, with the Nu results shown in Fig. 46. Again, the bifurcating configurations show better performance than their radial alternatives, except for when k^* = 1, in which case the results, although close, indicate a slightly better performance for the radial configuration. One interesting aspect in the definition of Nu is the effect of q'' – the heat flux across the solid-fluid interfaces is function of the surface area between the two constituents, Eq. (30), and this area decreases as the number of bifurcation increases, leading to a higher heat flux.

A summary of the Nu results is shown in Fig. 47. It is worth recalling the flows are always laminar, being fully developed in the radial flow configuration. The bifurcating cases add another component to the heat transfer process, as seen in the flow results, of flow recirculation as M increases. The separation and fluid recirculation that occurs when the fluid passes through the bifurcations hinders the convective process, and this effect should be more evident when bifurcations are present. It seems, nevertheless, this effect is overcome by the reduction in the heat flux and by the better access to the heat flow provided by the bifurcating configurations.

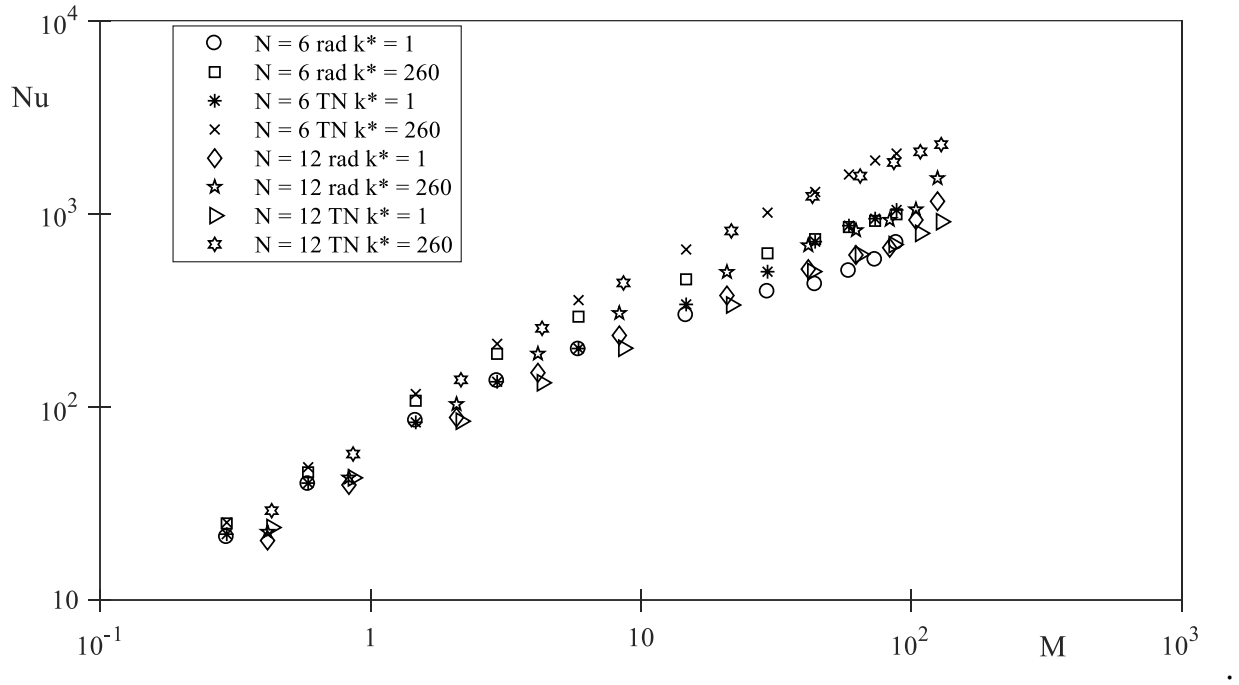

Figure 47. Nusselt number versus M, for N = 6 and 12, and k^* = 1 and 260.

3.4 Conclusions

Numerical simulations of four distinct optimal flow configurations designed for cooling a heat generating and adiabatic disc are performed to identify and compare their thermo-hydraulic behaviors. The configurations are for a fixed volume of fluid channels, with the fluid entering through the center of the disc, splitting into either radial (straight) segments or bifurcating branches, feeding either 6 or 12 outlets positioned at the periphery of the disc. The bifurcating configurations have either one-level or two-level bifurcating networks, and all have three equally distributed branches emanating from the disc center. All geometric parameters of these flow configurations, such as length and diameter of the pipes, are optimized for minimizing the total pressure loss. The geometric optimization process [23] assumes fully developed laminar flow in

all ducts (assuming circular pipes), and it neglects pressure losses at the bifurcations, yielding theoretical estimates for the pressure drop across every configuration. The neglect of the bifurcating effects is supposed to be acceptable (i.e., lead to accurate results) when the svelteness Sv of the network is smaller than 3.16 (or $Sv^2 < 10$), a result derived for T-shape flow networks [26].

The present effort is started with the mathematical modeling of the thermo-hydraulic process in the solid and fluid regions of the disc, including balance transport equations and boundary and compatibility conditions. Nondimensional equations are derived, and ruling parameters identified. The importance of presenting the thermo-hydraulic results in terms of the nondimensional mass flow rate entering the disc, instead of the usual Reynolds number, is highlighted, particularly for comparison purposes of distinct flow configurations. Nondimensional pressure drop, maximum disc temperature, and the Nusselt number are defined for investigating the thermo-hydraulic performances.

Numerical simulations are performed for the case of isothermal water (Newtonian and incompressible fluid) flowing into the disc, under laminar fully developed flow regime in all flow configurations. For the one-level and two-level branching configurations, the Reynolds number of the flow in each pipe segment is shown to decrease for the optimal network as one moves from the center segment to the outmost (exit at the disc periphery) segment. The solid material of the disc has a uniformly distributed volumetric heat dissipation rate, and is considered homogeneous and isotropic.

The numerical pressure loss results are verified against the analytical results available for the radial cases and for the theoretical results obtained by [23] valid for small flow rate (when the laminar fully developed flow and negligible bifurcation loss assumptions are valid). The results

show the hydraulic performance of the flow networks (with bifurcations) is strongly dependent on the number of bifurcations and on the flow strength (mass flow rate). Even though the Sv numbers of the bifurcating configurations should validate a negligible bifurcation effect on the pressure drop, the results clearly show the $Sv^2 < 10$ criterion not to be valid for the current configurations. In this respect, bifurcating networks perform better than their radial counterparts when $M < 10$ for the cases considered here. Of course, when bifurcation effects become pronounced, the more bifurcations a network has the more pressure loss it imposes on the flow. Radial with $N = 6$ performed best in terms of pressure loss.

In terms of thermal performance, a prediction of the best performance becomes even more complex with the introduction of the solid-fluid thermal conductivity ratio k^* into the conjugate convection-diffusion process inside the disc. In general, as k^* increases the conduction thermal resistance of the solid decreases, making the convection thermal resistance of the flow network more predominant on the overall thermal performance, and this makes the maximum disc temperature decrease with an increase in the flow rate, as expected. For small k^*, say $k^* = 1$, the flow configuration affects the thermal performance more and the radial configurations perform better than their bifurcating counterparts. This means when the thermal resistance by conduction is high, the proximity of the flow channels to the heat generating material becomes important, and the radial design provides shorter distances for the heat to reach the flow channels as compared to the bifurcating configurations. When k^* is high, such as 260, the maximum temperature of the disc is similar for all configurations until M reaches beyond about 10. This makes sense: as k^* increases, the convection effect becomes more important; hence the distance for the heat to reach the flow channels becomes less important, so the geometry differences between radial and bifurcating configurations becomes less important. Nevertheless, the heat transport effectiveness of

convection increases when the flow is strong. So, the differences between the flow configurations emerge only when the flow rate is high enough, in which case the bifurcating configurations emerge as better options.

In terms of Nu, the most complex configurations considered, namely the bifurcating configurations, yield the best performance, or the highest Nu, for the entire M range and high k^*, with their values being very similar. Interestingly, the flow configurations and k^* have a limited effect on the Nu variation with M, with the effect increasing slightly as M increases, as expected. Hence, the overall convection effect, which occurs inside the flow channels, seems very robust in terms of variations in the flow configuration and on k^*.

A final observation about the numerical simulations becomes necessary. As attempting to achieve convergence of the numerical results as M increases, not only the computational time necessary to achieve convergence, but also instability toward a convergent result is observed. This explains for instance the slight variation in behavior when M closes in the maximum value used in the laminar regime, namely $M = 100$. In this range, the flow at the initial pipes coming off the disc center present a very high Re, at the border of what is expected for laminar regime. Although the Re of each pipe from the center decreases for the optimal configurations, the numerical simulation certainly feels the difficulty in solving the flow and temperature fields of these high Re pipes. Although this is a localized effect, the numerical simulation everywhere in the domain is affected by this difficulty. This is why the laminar range was limited here to $M_{max} = 100$.

4 BIFURCATING FLOW NETWORKS FOR COOLING A HEAT GENERATING DISC – TURBULENT FLOW CASE

As one attempts to resolve the flow and temperature fields of the configurations considered in Chapter 3 with increasing mass flow rate *M*, one quickly ends up facing increased computational time and eventually numerical instability, and even lack of converged results. This was experienced near the maximum *M* value considered in the previous chapter, as indicated previously, even when the turbulent regime sets in on a few of the flow pipes making a branch (recall the Reynolds number of each flow segment decreases from the disc center toward the periphery). An alternative to allow overcoming this difficulty is the utilization of turbulent models for facilitating the numerical simulations of higher *M* values. Hence, the analysis performed in the previous chapter for the laminar regime is here extended to turbulent flow inside the four configurations considered.

In the literature, it is unusual to find studies considering turbulent flow when applying complex, optimal flow networks as the ones used here, because of the reduction in strength (recall the Reynolds number decreases) as the flow goes through the bifurcating networks. It is a well-known fact in the respiratory tract of human lungs, for instance, the convection process initiated at the trachea level during air inspiration eventually transitions to a diffusion dominated process when the air reaches a certain depth into the lungs (usually past the 17^{th} bifurcation). This transition happens because of the several bifurcations undergone by the original flow. Even though the diameter of individual bifurcated channels decreases, which would cause an increase in fluid speed for the same flow rate, the total available flow area past the bifurcation increases, yielding a smaller Re in the individual channels.

Nevertheless, turbulent flows can be achieved in flows through optimal bifurcation networks, particularly when the number of bifurcations is not large. Miguel [29], for instance, reported an analysis of optimal branching networks of tubes for heat transfer and fluid flow. His work unveils the structural features of these networks, mainly via relationships between the sizes of the parent and daughter tubes and the branching angles of the bifurcations. The process of construction of these networks is described for both laminar and turbulent flow, Newtonian and power-law fluids, and constant and pulsatile flows.

4.1 Mathematical Modeling and Numerical Simulations: Turbulent Flow

The geometries, or flow configurations, used to simulate the turbulent flows here are the same as the one described in laminar flow chapter, see Fig. 26 and Table 2. The balance equations, Eqs. (12)-(15), are also the same, except for the inclusion of turbulence diffusions in the momentum, Eq. (13), and energy, Eq. (14), equations of the fluid flow. In this case, ν of Eq. (13) is replaced by $(\nu + \nu_t)$ and α_f of Eq. (14) is replaced by $(\alpha_f + \alpha_{f\_t})$, where the subscript *t* indicates turbulence diffusivity. Before discussing the determination of these new two turbulence parameters, the boundary and compatibility conditions of the model equations also remain the same, except the inlet velocity profile, which must be modified from laminar profile to turbulent profile. The nondimensional expressions, including the M, f, T_m^*, and Nu definitions Eqs. (22), (27)-(29), the Re versus M relations, Eqs. (23)-26, are still valid, observing of course the modifications indicated so far.

The determination of the turbulence diffusivities ν_t and α_t follows from using turbulence models. Although there are several types of turbulent models in the literature, the standard k–ε model is chosen due to its accuracy in confined (pipe) flows [30].

The k–ε model incorporates two additional balance equation, one for the turbulence kinetic energy k and one for its dissipation rate ε. These equations require an additional set of closure equations, and these equations carry several constants. Modifications of the closure equation and its constants have given rise to several modified k–ε models. Here, the standard k–ε model is used, for being well developed, suitable for the present need, and validated for a large number of flow configurations [31]. The underlying assumption of the k–ε model is that the turbulent diffusivity is isotropic, in other words, the ratio between Reynolds stress and the mean rate of deformations is the same in all directions. The balance equations for turbulence kinetic energy k, and its rate of dissipation, ε, are, respectively:

$$\frac{\partial(\rho k)}{\partial t}+\frac{\partial(\rho k u_i)}{\partial x_i}=\frac{\partial}{\partial x_j}\left[\left(\mu+\frac{\mu_t}{\sigma_k}\right)\frac{\partial k}{\partial x_j}\right]+P_k+P_b-\rho\epsilon-Y_M+S_k \tag{32}$$

$$\frac{\partial(\rho \epsilon)}{\partial t}+\frac{\partial(\rho \epsilon u_i)}{\partial x_i}=\frac{\partial}{\partial x_j}\left[\left(\mu+\frac{\mu_t}{\sigma_\epsilon}\right)\frac{\partial \epsilon}{\partial x_j}\right]+C_{1\epsilon}\frac{\epsilon}{k}(P_k+C_{3k}P_b)-C_{2\epsilon}\rho\frac{\epsilon^2}{k}+S_\epsilon \tag{33}$$

The turbulent viscosity μ_t, where $\mu_t = \rho_f \nu_t$, is obtained by combining k and ε, as:

$$\mu_t=\rho C_\mu\frac{k^2}{\epsilon} \tag{34}$$

where C_μ is a constant ($C_\mu = 0.09$). The turbulence thermal diffusivity is set as

$$\alpha_t = \frac{\nu_t}{Pr_t} \tag{35}$$

with the default value of the turbulent Prandtl number Pr_t is 0.85.

The term P_k is the generation of turbulent kinetic energy from the mean velocity gradients, defined as:

$$P_k = -\rho \overline{u_i'} \overline{u_j'} \frac{\partial u_j}{\partial u_i} \tag{36}$$

and can be evaluate in a manner consistent with the Boussinesq hypothesis:

$$P_k = \mu_t S^2 \tag{37}$$

where S is the modulus of the mean rate-of-strain tensor, defined as:

$$S \equiv \sqrt{2 S_{ij} S_{ij}} \tag{38}$$

The default constants $C_{1\epsilon}$, $C_{2\epsilon}$, C_μ, σ_k and σ_ϵ have been achieved from fine tuning the numerical predictions of the method with experiments with air and water for fundamental turbulent shear flow [30]. They have been found to work well for a wide range of wall-bounded and free shear flows, and are used here: $C_{1\epsilon} = 1.44$, $C_{2\epsilon} = 1.92$, $C_\mu = 0.09$, $\sigma_k = 1.0$, $\sigma_\epsilon = 1.3$.

The inlet velocity profile used for the turbulence case is:

$$u_z(r) = U_0 \left[1 - \frac{r}{R}\right]^{1/n} \tag{39}$$

where n is the exponent given by the power-law equation; usually, $n = 7$ is chosen, giving rise to the term "a one-seventh power profile". The mean velocity U_0 can be used to calculate the maximum velocity u_{max} in the center pipe entry using the following relation [30] :

$$U_0 = \frac{2n^2}{(2n+1)(n+1)} u_{max} \tag{40}$$

Here, the numerical simulations are performed for *M* extended from about 120 (recall the maximum *M* value of the laminar regime is 100) to about 5,700. The high end of M is equivalent to a maximum entry Re_0 of about 100,000.

The numerical simulations of the turbulent flow through the radial branches can be validated against the theoretical predictions for pressure loss of turbulent flow along a straight channel, using [32]:

$$\Delta P = f \rho R \frac{U_0^2}{2D_0} \tag{41}$$

For smooth-walled pipes, the relation established by Prandtl in 1935 with the constants adjusted slightly to fit the friction data better, can be used, namely:

$$\frac{1}{\sqrt{f}} = 2.0 \, log\left(Re_0 f^{\frac{1}{2}}\right) - 0.8 \tag{42}$$

Equation (42) needs to be solved iteratively.

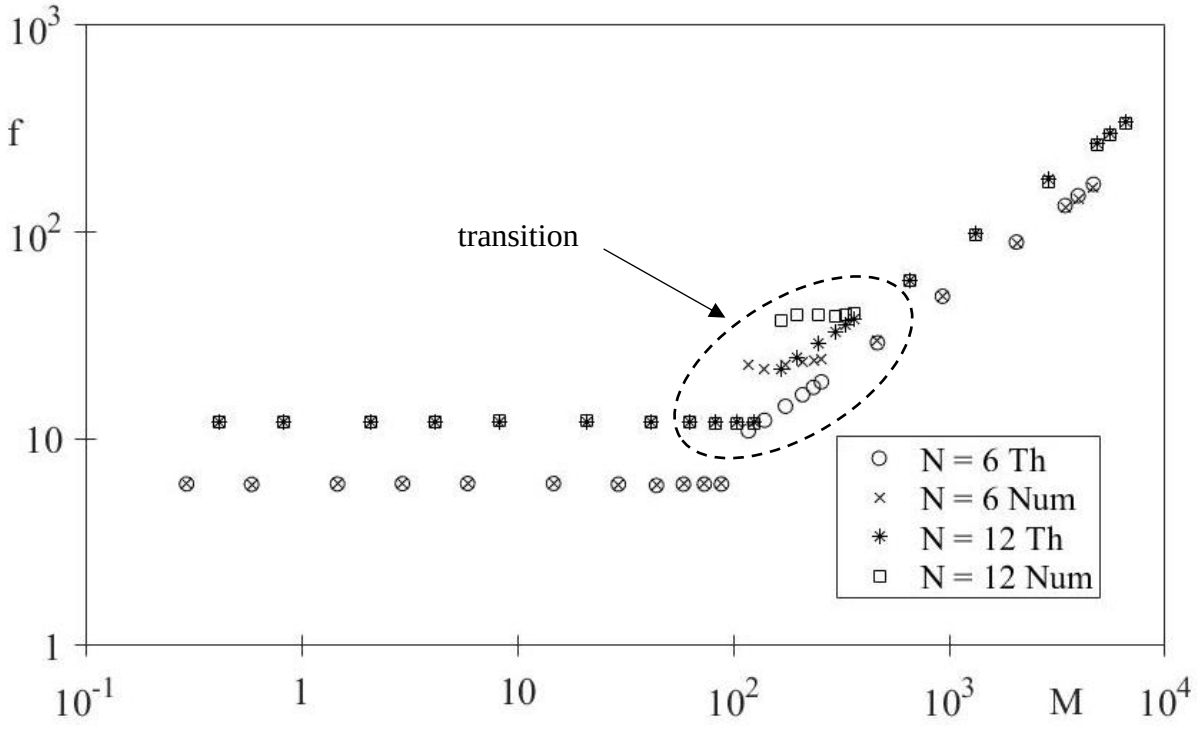

Figure 48. Nondimensional pressure loss versus nondimensional flow rate comparison with theoretical predictions for radial configuration with N = 6 and 12.

The numerical results are validated against the theoretical predictions available for turbulent flow through a smooth straight pipe, with the results shown in Figure 48. Included in the same graph are the results for the laminar regime, for completeness. Because the numerical model does not capture well the transition regime, one shouldn't expect good agreement within this region (shown with a dashed circle in the figure). Outside this small range, the agreement is remarkable. This agreement also speaks about the grid accuracy – several grid tests are performed to guarantee the same criterion used for the laminar regime, namely better than 5% agreement with results obtained when using a grid twice as dense for all simulations.

4.2 Results and Discussions

The results follow pretty much the presentation of results for the laminar regime, which is included in the figures for completeness. The hydraulic performance of the configurations used here are presented in terms of the nondimensional pressure drop across a flow branch, versus the nondimensional flow rate, shown in Figures 49 and 50 for N = 6 and 12, respectively.

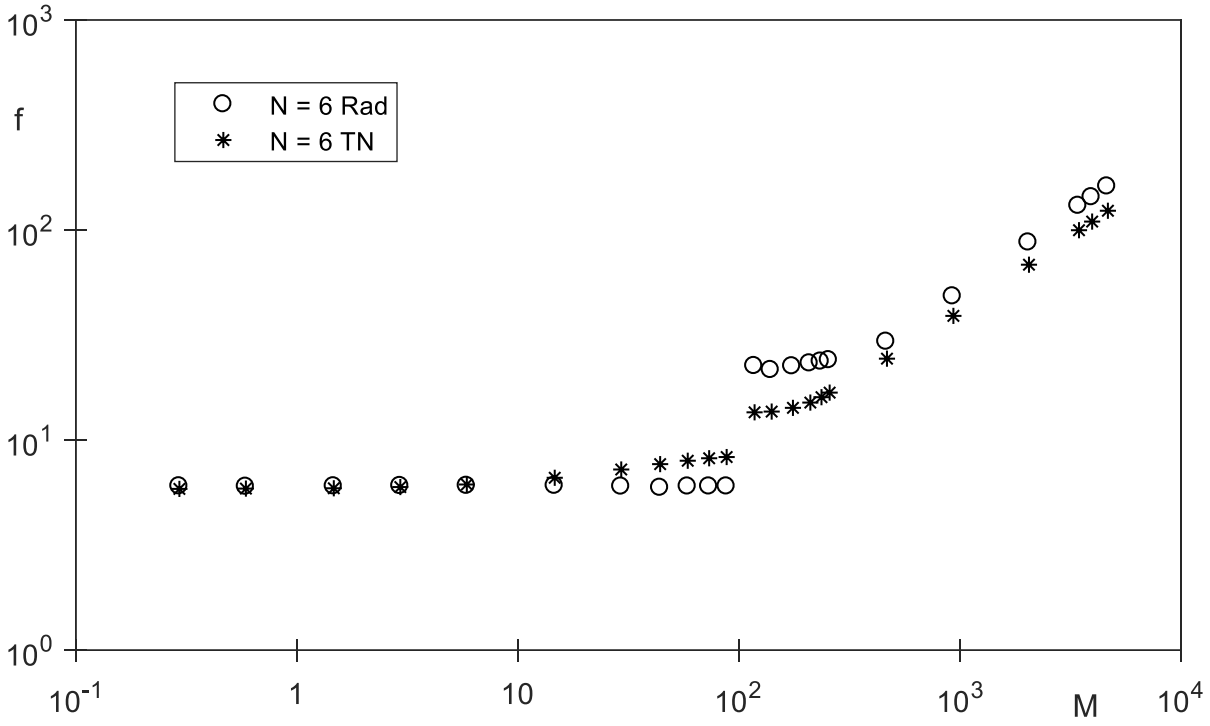

Figure 49. Dimensionless pressure drop versus flow rate for *N* = 6.

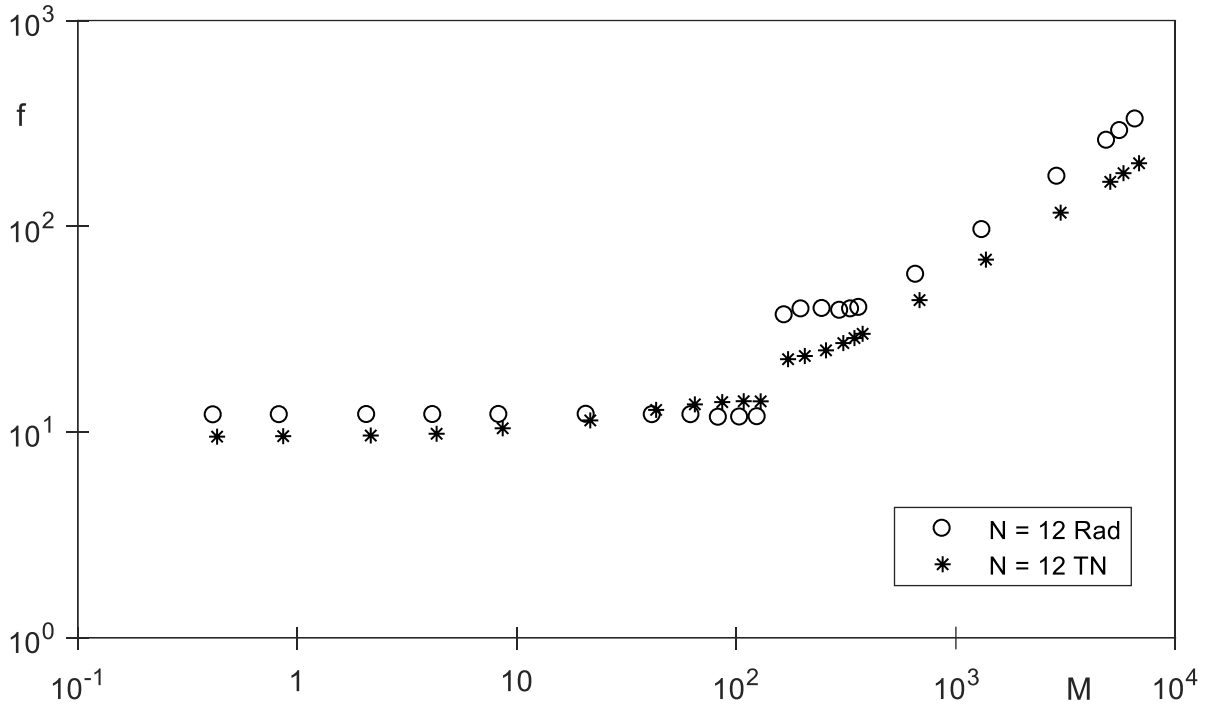

Figure 50. Dimensionless pressure drop versus flow rate for N = 12.

Both figures show a switch in how hydraulic performance of the radial and bifurcating configurations compare. Within the laminar regime, in both cases, for N = 6 and 12, the radial configurations pressure drop is very comparable to the pressure drop of the bifurcating configurations for the same M, with the latter being slightly better when M < 30, then worse when M > 30. In the turbulent regime the performance switches again, with the bifurcating configurations clearly performing much better than their radial counterparts.

This switch in performance can be explained with the help of Figure 51, where streamlines are shown for the flow across the first bifurcation of the two-level bifurcating network with N = 12. For $M = 100$ the flow separation downstream of the bifurcation is larger than the separation observed when M = 5,700. This means the flow area restriction when M = 100 is also larger,

causing a larger pressure drop, which becomes larger than the pressure drop for the same *M* in the radial flow. As M increases, the constricted flow area gets smaller, and the resulting pressure drop becomes smaller than the corresponding pressure drop of the radial configuration.

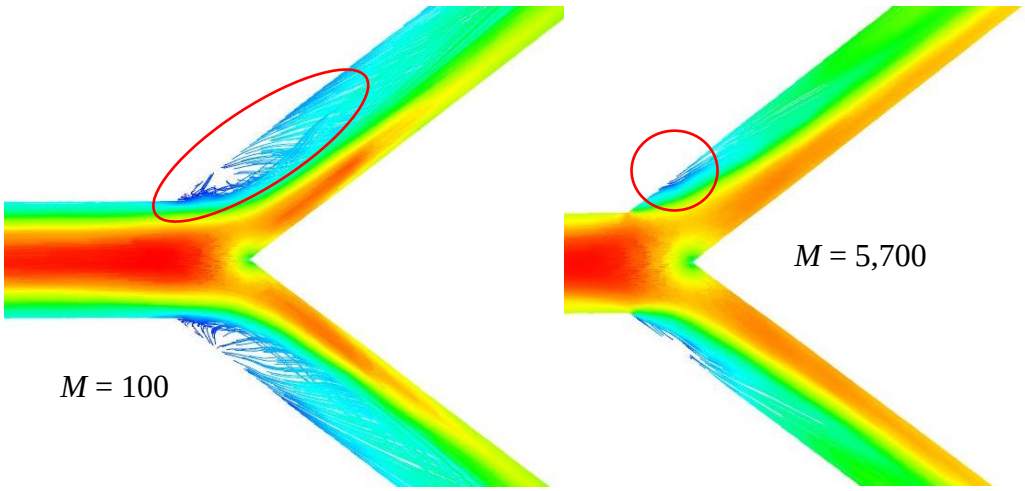

Figure 51. Streamlines for two-level bifurcation network branch across the first bifurcation for M = 100 and M = 5,700.

The pressure drop distribution in four configurations are presented in Figure 52 for *M* = 5,700. For this high flow rate the bifurcating networks yield lower pressure drop than their corresponding radial configurations.

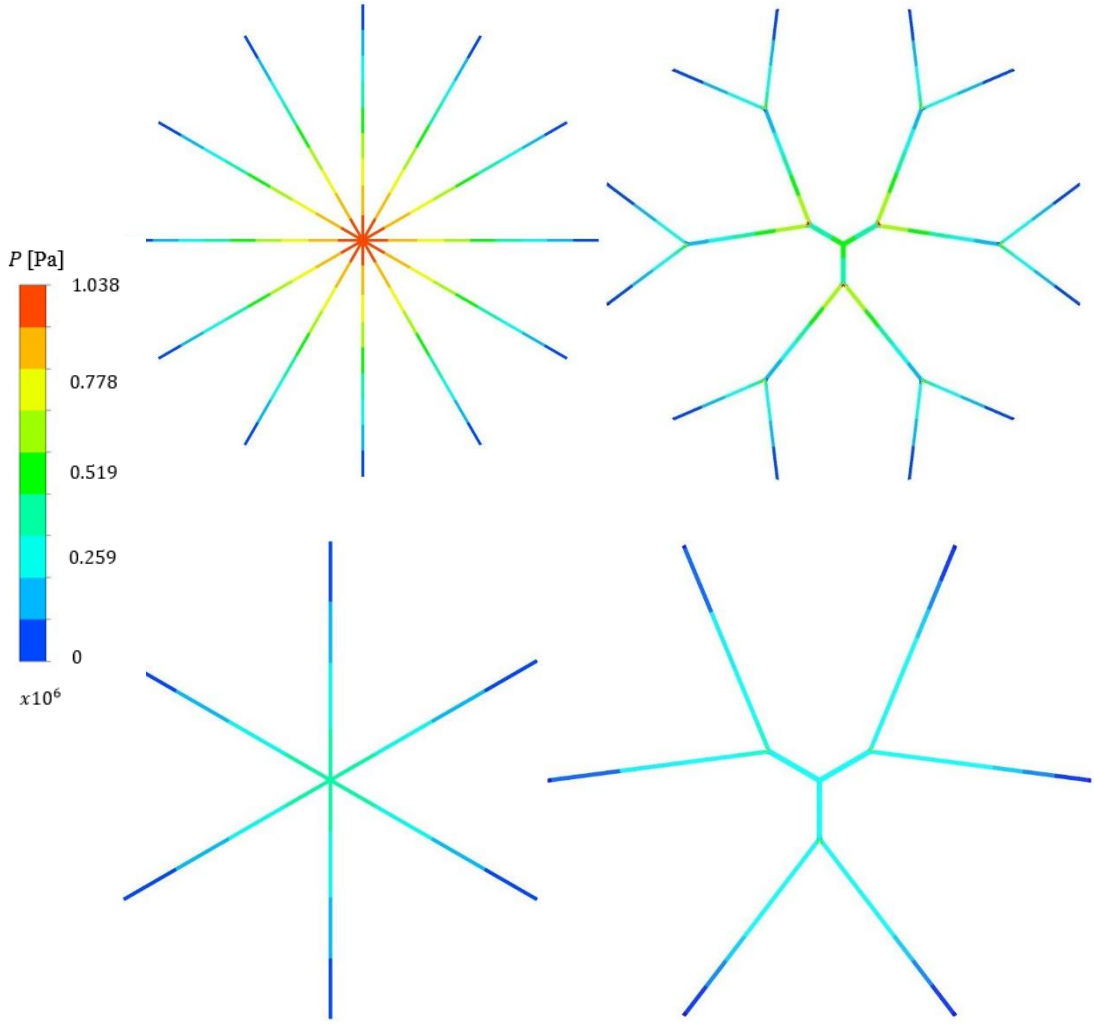

Figure 52. Nondimensional pressure distribution along the flow pipes of radial and bifurcating configurations, for N = 6 and 12, with M = 5,700.

Figure 53 summarizes the flow resistance results using the f_{TN}/f_{Rad} ratio, now with results for the laminar and turbulent flow regimes. The ratio above 1.0 means that the radial geometry has lower flow resistance compared to its equivalent bifurcating network configuration. Therefore, roughly for M < 10 and M > 120, the bifurcating configurations yield the best performance independent of N, and, for 30 < M < 100, radial configuration seems best.

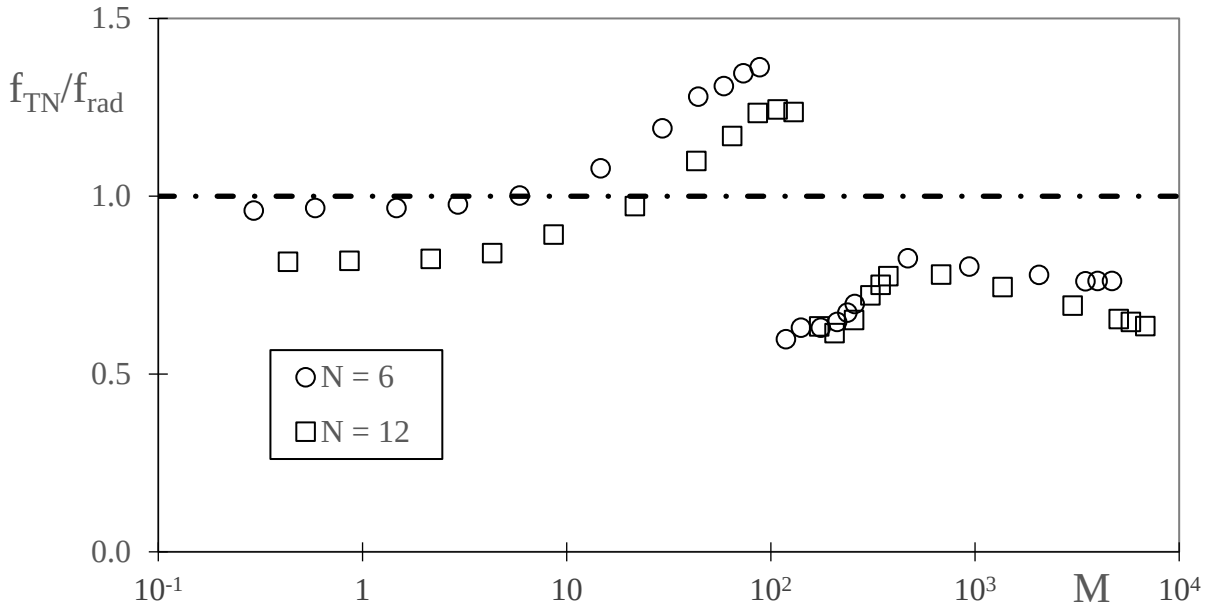

Figure 53. Dimensionless flow resistance ratio versus *M*.

One can notice, for the whole M range, $(f_{TN}/f_{Rad})_{N=6} > (f_{TN}/f_{Rad})_{N=12}$. Keep in mind the turbulence results are not expected to be very accurate within the transition zone, 120 < M < 400.

A summary of the hydraulic results is presented in Figure 54. When the volume of pipes is constant, as in here, the configurations with N = 6 (radial and bifurcated) automatically present higher pipe diameters and therefore, for the same mass flow rate, they will yield lower pressure loss in the laminar flow range. The results corroborate this, indicating the radial configuration to be slightly better as *M* increases. This predominance of the N = 6 configuration as best hydraulic performers is also true in the turbulent regime, except now the bifurcating configuration is better than the radial one.

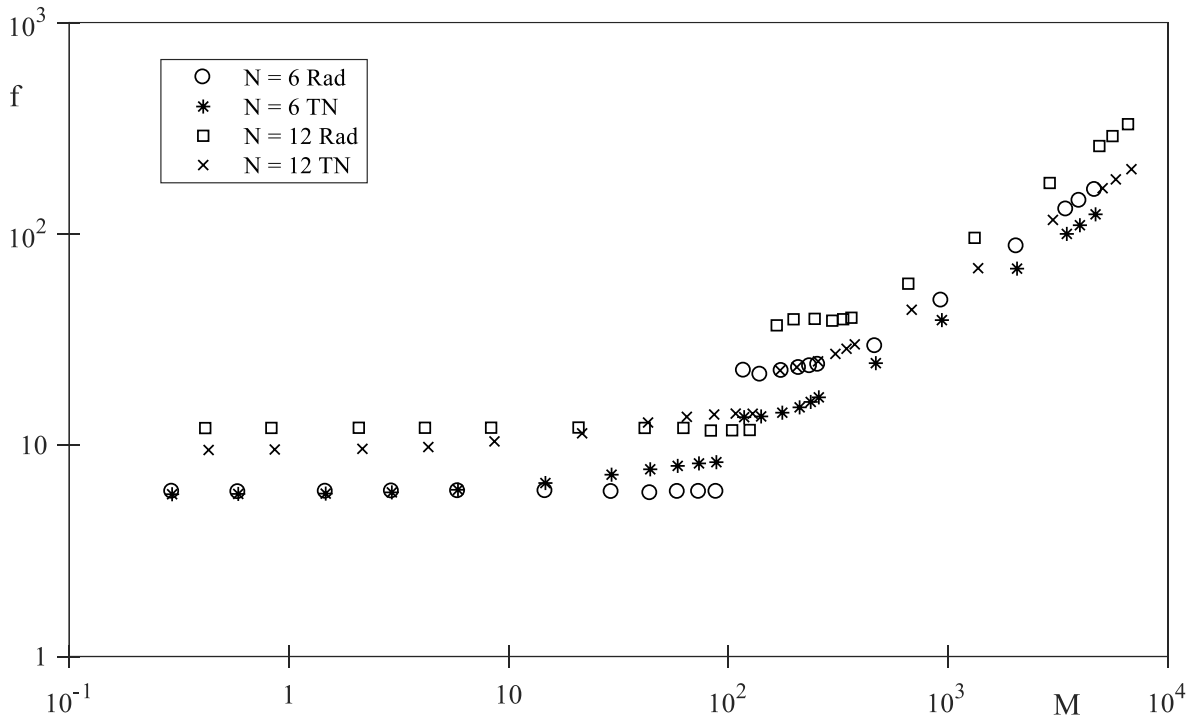

Figure 54. Dimensionless pressure drop versus flow rate for N = 6 and 12.

Figures 55 and 56 show T_m^* results for radial and bifurcating configurations, respectively, with N = 6, for varying M and several k^* values. In all cases T_m^* decreases as M increases, as expected. Notice, however, how the effect of increasing M becomes much more pronounced as k^* increases: this indicates the reduction in the solid diffusion resistance to heat transfer as k^* increases. The turbulent results extend the laminar results, maintaining pretty much the same general tendencies observed at the high end of the M values for the laminar regime: the variations tend to flatten out as M increases being 7,000 for all k^* values, showing the limit of the convection ability to remove the heat.

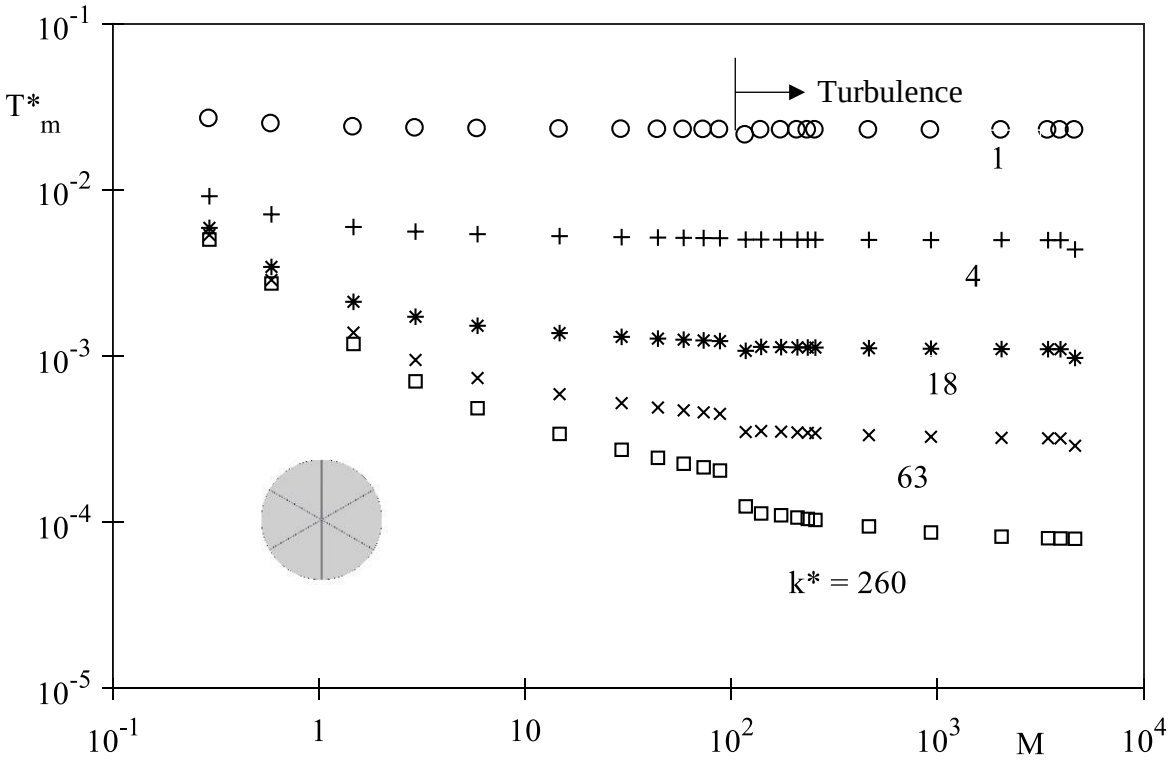

Figure 55. Nondimensional maximum disc temperature versus *M*, for *N* = 6 and radial configuration.

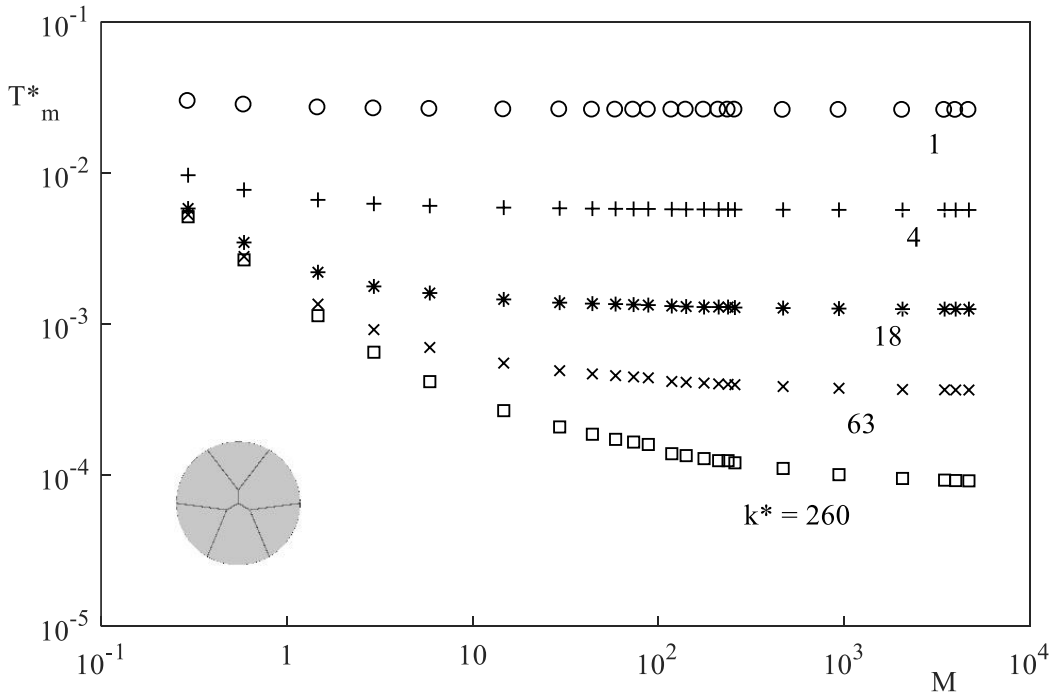

Figure 56. Nondimensional maximum disc temperature versus *M*, for *N* = 6 and one-level bifurcating configuration.

Figures 57 and 58 show similar results, now for the cases of $N = 12$. The same observations made in respect to Figs. 48 and 49 apply to this case as well. Hence, each k^* case has a limiting M beyond which T_m^* no longer decreases appreciably – this marks the convection resistance limit, beyond which this resistance becomes negligible, and M no longer affects the overall thermal performance. Observable also in all four figures the smaller sensitivity of the radial configurations to changes in k^* as compared to the bifurcating networks: see how the spreading of T_m^* (particularly for high M) as k^* varies from 1 to 260 is narrower in the radial cases. Once again, the turbulent results corroborate the trend seen for the laminar flow. Except for the radial flow case where, for $k^* > 63$ the thermal resistance dropped in the turbulent regime.

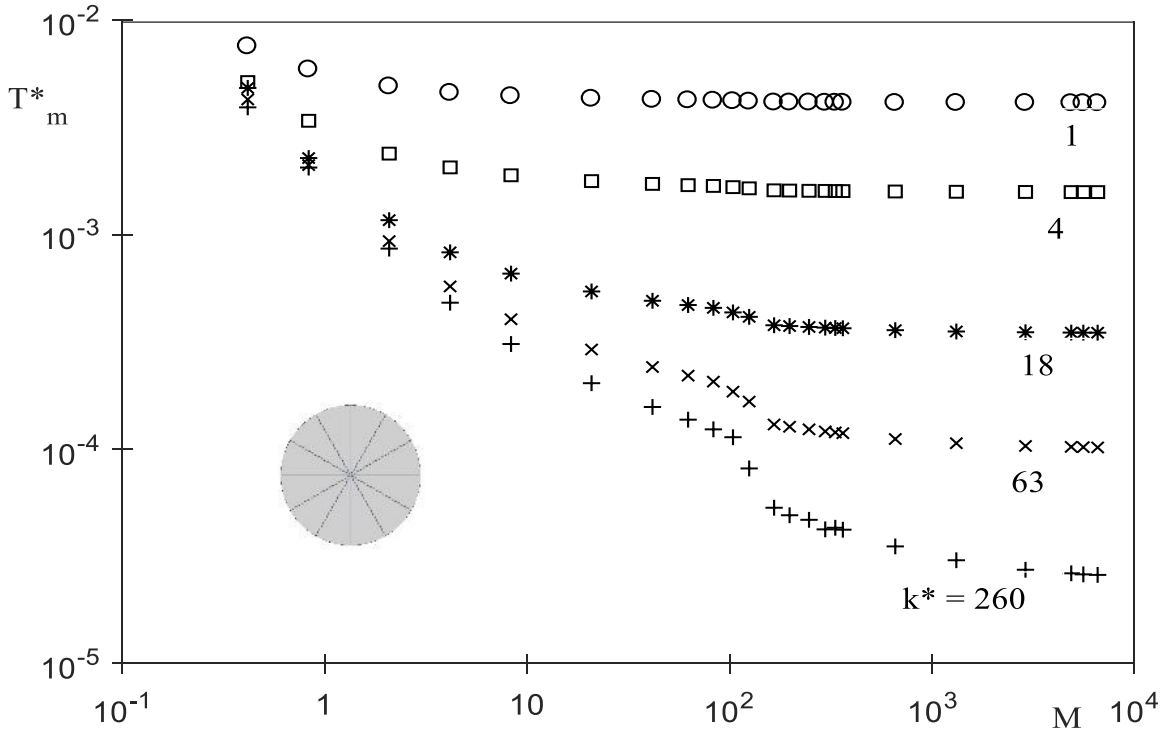

Figure 57. Nondimensional maximum disc temperature versus M, for $N = 12$ and radial configuration.

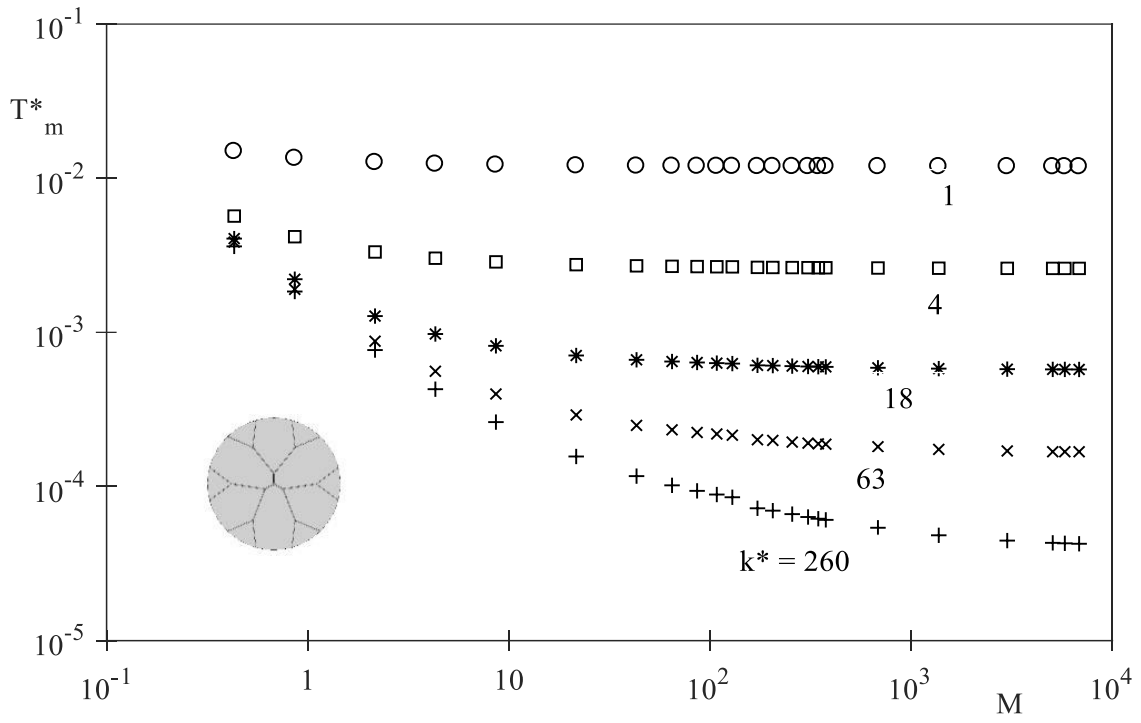

Figure 58. Nondimensional maximum disc temperature versus *M*, for *N* = 12 and two-level bifurcating configuration.

The radial and bifurcating networks performances, for *N* = 6 and 12, can be compared again in terms of T_m^* when considering Fig. 52, for the case k^* = 260, for the entire *M* range including laminar and turbulent flow. Recall this case yields a very small diffusion resistance (for k_s being much higher than k_f). An initial observation, common to both *N* cases, is that when *M* is in the laminar regime the results seem to be less sparse if compared to the turbulence regime.

As observed in the previous chapter, as *M* increases past 10, the performance of the two networks flips, with the bifurcating networks yielding better results with smaller T_m^* than their radial counterparts until the end of the laminar regime range. However, for M > 120 the results flip again with radial flow yielding better results than the bifurcating results.

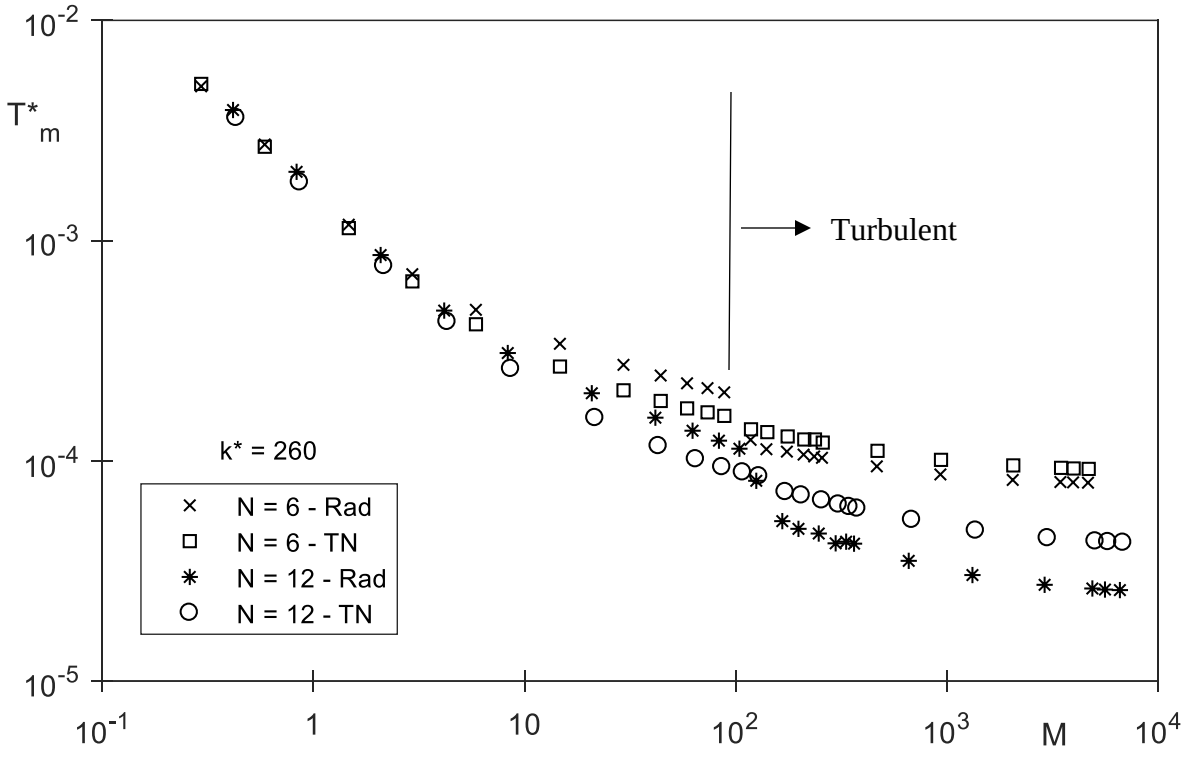

Figure 59. Nondimensional maximum disc temperature versus *M*, for *N* = 6 and 12 and k^* = 260.

A possible justification for the switch is the likely predominance of the turbulence diffusivity affecting the effect of flow separation region the bifurcations induce when *M* is in the turbulence regime compared with the end of the laminar flow range. Notwithstanding, the radial network with *N* = 12 leads to better thermal performance for all turbulent flow range.

Figure 60 shows the solid and liquid region temperature distributions for all flow networks with *M* = 5,700 and k^* = 260.

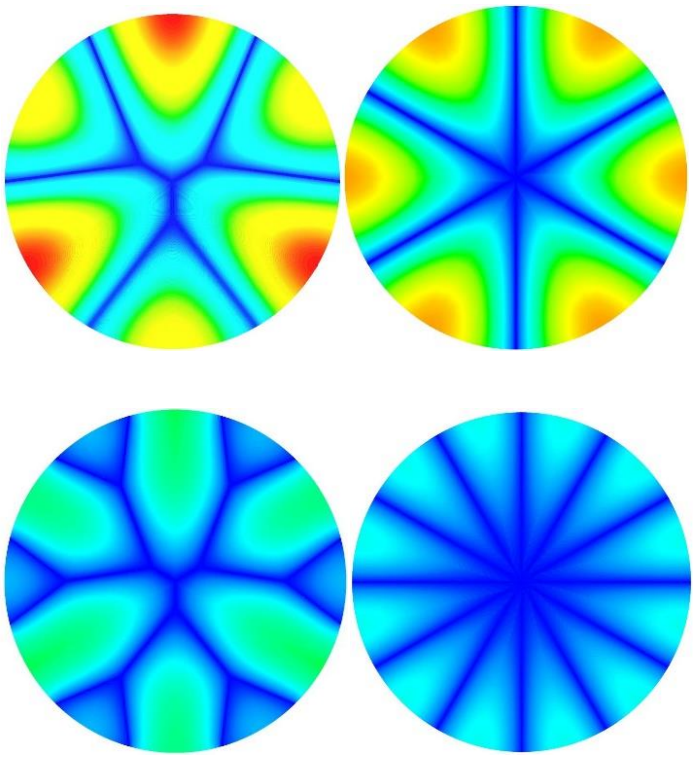

Figure 60. Nondimensional temperature distribution for M = 5,700 and k^* = 260.

As it can be identified, the fluid temperature does not seem to vary much as the fluid flows from the center of the disc toward the periphery, as expected (very high k^* and M). The best thermal performance, in terms of smallest T_m^*, is achieved by the radial configuration with N = 12. Notice with very small convective thermal resistance, the thermal performance is best for the configuration that shortens the most the path to be travelled by the heat from the solid region to the pipes. Although this observation is in line with the conclusion by [15], here the situation involves turbulent flow, as opposed to laminar flow.

Figure 54 shows nondimensional temperature distributions for radial configurations N = 12 and M = 5,700, for several k^* values. Observe the temperature distribution for the case k^* = 260 differs from the one presented in Figure 53 because of the temperature range used – the same

for all cases in Figure 54 – is not wide enough to allow for the distinct observation of the temperature variation in the cases of k^* = 18 and 260. Hence, in relation to the temperature variation observed for the k^* = 1 case, the high k^* cases show basically isothermal condition in the disc.

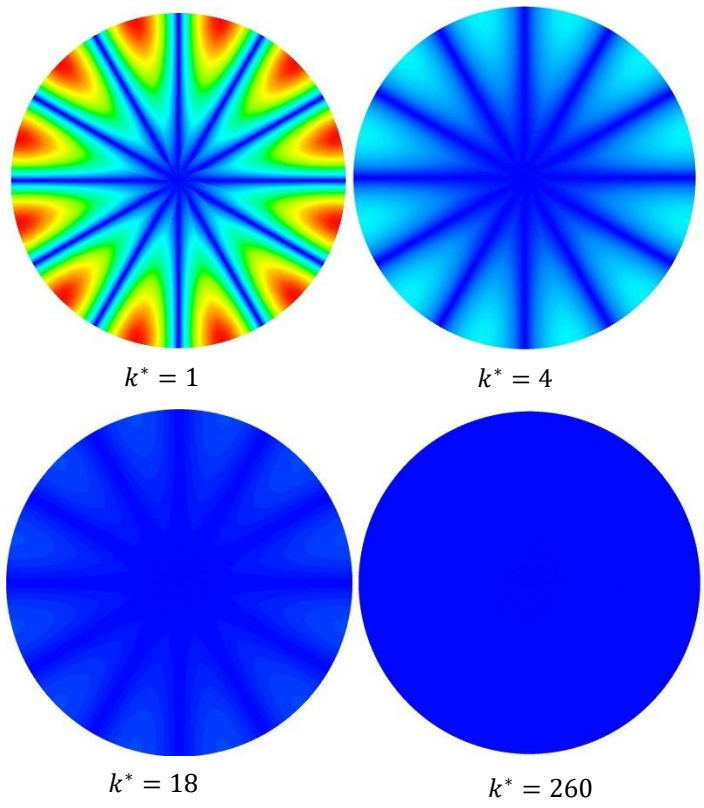

Figure 61. Nondimensional temperature distribution for N = 12, radial configuration, M = 5,700 and several k^* values.

Figures 62 and 63 show Nu results for all four geometries considered in this work for k^* = 1 and 260. Notice that the best performing configurations near the end of the laminar regime to be the bifurcating ones with N = 6 and 12. As M increases further, there is a shift in the performance of the radial and bifurcating networks with N = 6 and 12. That is, for the entire turbulent flow range, the radial flow configurations perform better, with k^* = 260 a little better than k^* = 1. This is in line with the results for T_m^*.

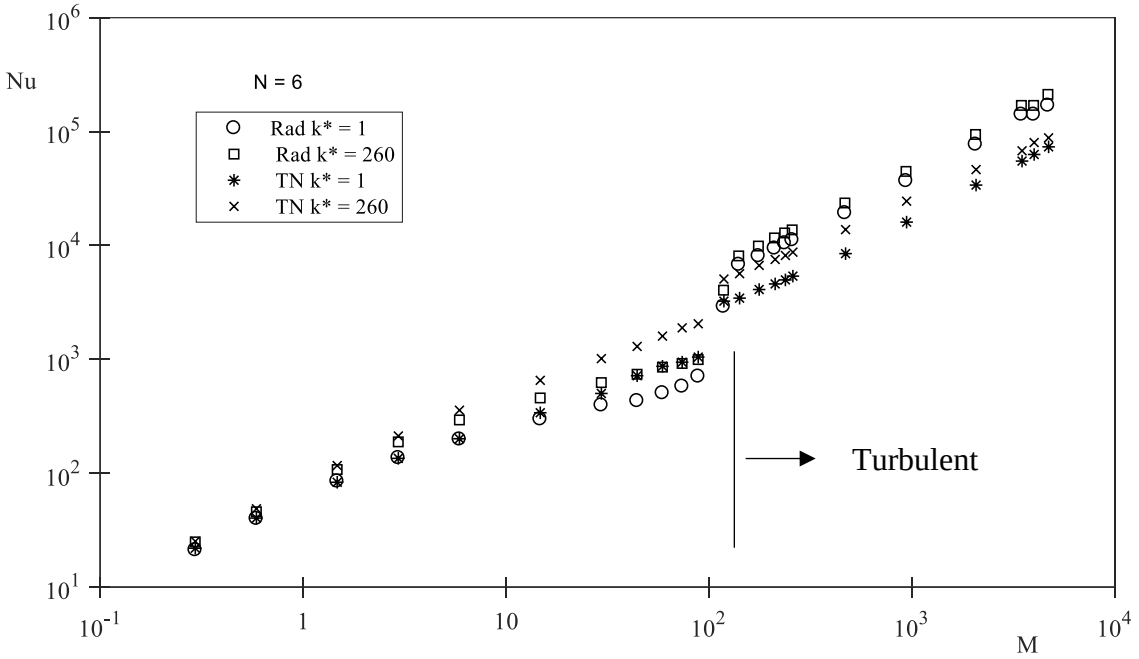

Figure 62. Nusselt number versus M for N = 6, radial and one-level bifurcating configurations, k^* = 1 and 260.

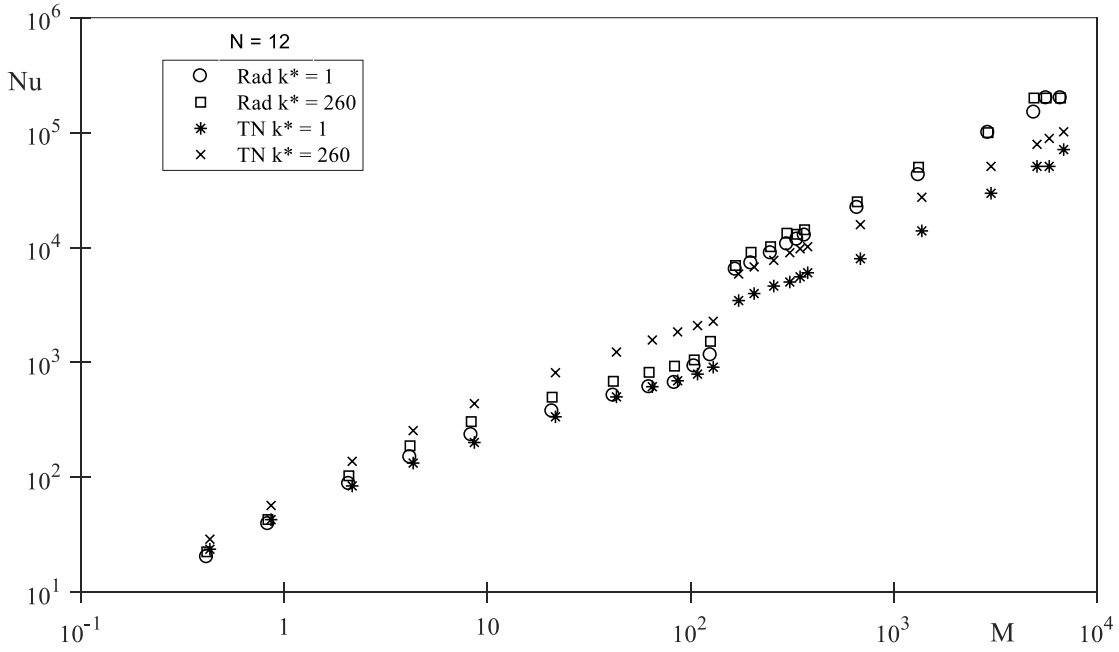

Figure 63. Nusselt number versus M for N = 12, radial and one-level bifurcating configurations, k^* = 1 and 260.

In terms of k^*, there is no single flow configuration that performs better for the entire M range considered here. For laminar flow, the bifurcating configurations seems to hold an edge for high k^* , while radial configuration performs better for any k^* in turbulent flow.

The thermal resistance results show that $k^* = 260$ configurations perform better for either radial or bifurcated geometries. One can try to establish a parallel for Nu numbers for the same configuration. Figure 57 shows the Nu results for N = 6 and 12 bifurcating configurations. One can see that the results are very similar for the entire mass flow range. Therefore, the comparison in terms of Nu numbers is inconclusive to determine if a higher number of outlets is preferable. The results for k^* = 4, 18 and 63 aren't included since they would be in between the result obtained for k^* = 1 and k^* = 260.

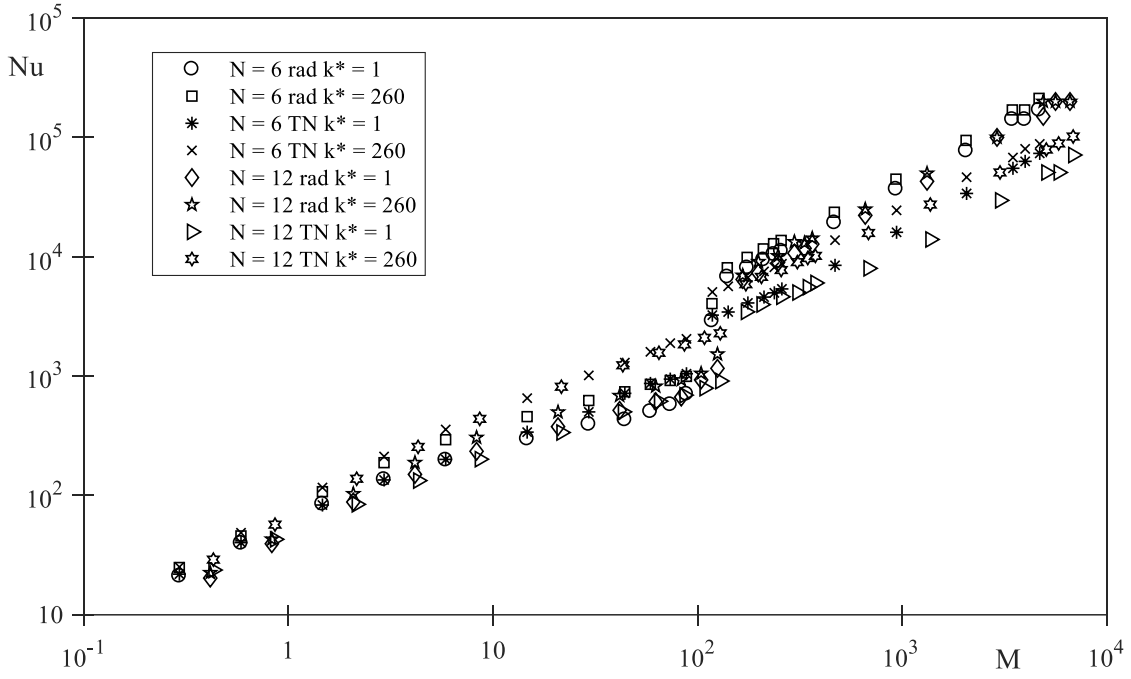

Figure 64. Nusselt number versus M for N = 6 and 12, k^* =1 and 260.

4.3 Conclusions

The numerical results presented here expand to turbulent regime the analysis and conclusions reached in the previous chapter, particularly in terms of thermal-hydraulic performances of radial and bifurcating networks, designed for cooling a heat-generating disc. The hydraulic performance of the flow networks is strongly dependent on the number of bifurcations and on the flow strength (mass flow rate) beyond which the bifurcations induced pressure losses become comparable/larger than the pressure losses caused by the straight sections of the flow channels. In this respect, bifurcating networks can be expected to perform best when the flow rate is small, and radial networks can be expected to perform best when the flow rate is high. Conversely, when the flow becomes turbulent, the shift in performance occurs again and bifurcating networks tend to perform better for N = 6 and 12.

Similarly, there seems to be no simple prediction in how the radial and bifurcating networks perform when it comes to the thermal performance of the disc. In this case, the relative solid-fluid thermal conductivity is an additional parameter to affect the behavior of the flow configuration. This parameter affects the diffusion thermal resistance in the solid region, and, as such, controls the extent to which the convection effect is effective in helping remove the generated heat from the disc. The heat transfer process being conjugated makes the prediction the thermal performance very difficult indeed, with the results showing again a shift in the behavior of radial and bifurcating networks when k^* increases, with radial networks performing better when k^* is small (close to one) and when M is large.

In summary, the decision to choose the flow network with the best performance depends on factors that go beyond the network being either radial or bifurcating. Moreover, the bifurcating effects (flow separation), which may or may not occur, seem to affect not only the overall pressure loss but also the overall heat transfer performance, with this effect being again dependent on k^*. Figure 65 presents a summary of the best performance in terms of thermal resistance, flow resistance, and Nusselt number.

Although it is difficult to choose between radial and bifurcated geometries in terms of thermal resistance, configurations with high k^* values present better performance with lower maximum temperature. This is an important conclusion of the present work since the number of applications in the industry that uses this type of configuration is large.

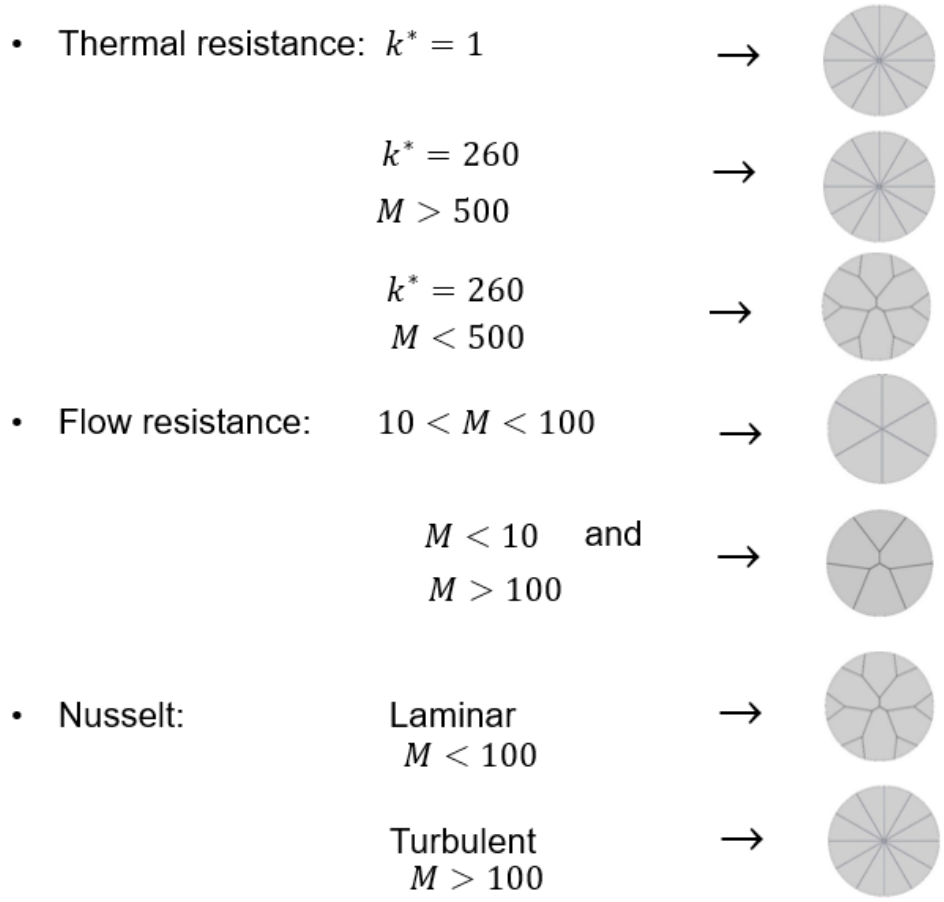

Figure 65. Summary of the best flow configurations in term of T_m^*, f and Nu for M and k^*.

BIBLIOGRAPHY

1. Bejan, A. (1997). Constructal-theory network of conducting paths for cooling a heat generating volume. International Journal of Heat and Mass Transfer, 40(4), 799,813-811,816. doi:10.1016/0017-9310(96)00175-5

2. Bejan, A. (2000). Shape and structure, from engineering to nature (1. publ. ed.). Cambridge [u.a.]: Cambridge Univ. Press.

3. Reis, A. H., Miguel, A. F., & Aydin, M. (2004). Constructal theory of flow architecture of the lungs. Medical Physics, 31(5), 1135-1140. doi:10.1118/1.1705443

4. Azoumah, Y., Neveu, P., & Mazet, N. (2007). Optimal design of thermochemical reactors based on constructal approach. AIChE Journal, 53(5), 1257-1266. doi:10.1002/aic.11152

5. Vianna, J. C. B., Estrada, Emanuel da Silva Diaz, Isoldi, L. A., dos Santos, E. D., & Souza, J. A. (2018). International journal of thermal sciences.126, 118-124. Retrieved from http://www.sciencedirect.com/science/journal/12900729

6. Reis, A. H., & Bejan, A. (2006). Constructal theory of global circulation and climate. International Journal of Heat and Mass Transfer, 49(11), 1857-1875. doi:10.1016/j.ijheatmasstransfer.2005.10.037

7. Bejan, A., & Gobin, D. (2006). Constructal theory of droplet impact geometry. International Journal of Heat and Mass Transfer, 49(15), 2412-2419. doi:10.1016/j.ijheatmasstransfer.2006.02.001

8. Morega, A. M., & Bejan, A. (2005). A constructal approach to the optimal design of photovoltaic cells. International Journal of Green Energy, 2(3), 233-242. doi:10.1080/01971520500198262

9. Chen, L., Wei, S., & Sun, F. (2014). The area–point constructal entransy dissipation rate minimization for a discrete variable cross-section conducting path. International Journal of Low-Carbon Technologies, 9(1), 20-28. doi:10.1093/ijlct/cts030

10. Almogbel, M., & Bejan, A. (2001). Constructal optimization of nonuniformly distributed tree-shaped flow structures for conduction. International Journal of Heat and Mass Transfer, 44(22), 4185-4194. doi:10.1016/S0017-9310(01)00080-1

11. Barik, A. K., Rout, S., & Patro, P. (2020). Evolution of designs for constructal cooling of a square plate using water, ionic liquid, and nano-enhanced ionic liquids. Journal of Thermal Science and Engineering Applications, 12(2) doi:10.1115/1.4045884

12. Sohel Murshed, S. M., & Nieto de Castro, C. A. (2017). A critical review of traditional and emerging techniques and fluids for electronics cooling. Renewable & Sustainable Energy Reviews, 78, 821-833. doi:10.1016/j.rser.2017.04.112

13. Kang, S. S. (March 2012). (March 2012). Advanced cooling for power electronics. Paper presented at the 1-8.

14. Rocha, L. A. O., Lorente, S., & Bejan, A. (2002). Constructal design for cooling a disc-shaped area by conduction. International Journal of Heat and Mass Transfer, 45(8), 1643-1652. doi:10.1016/s0017-9310(01)00269-1

15. Wechsatol, W., Lorente, S., & Bejan, A. (2003). Dendritic heat convection on a disc. International Journal of Heat and Mass Transfer, 46(23), 4381-4391. doi:10.1016/S0017-9310(03)00295-3

16. Lu, Z., Zhang, K., Liu, J., & Li, F. (2020). Effect of branching level on the performance of constructal theory based Y-shaped liquid cooling heat sink. Applied Thermal Engineering, 168, 114824. doi:10.1016/j.applthermaleng.2019.114824

17. Salimpour, M. R., & Menbari, A. (2015). Analytical optimization of constructal channels used for cooling a ring shaped body based on minimum flow and thermal resistances. Energy, 81, 645-651. doi:10.1016/j.energy.2015.01.008

18. Feng, H., Chen, L., Xie, Z., & Sun, F. (2015). Constructal optimization of a disc-shaped body with cooling channels for specified power pumping. International Journal of Low-Carbon Technologies, 10(3), 229-237. doi:10.1093/ijlct/ctt036

19. Reddy, B. V. K., Ramana, P. V., & Narasimhan, A. (2008). Steady and transient thermo-hydraulic performance of disc with tree-shaped micro-channel networks with and without radial inclination. International Journal of Thermal Sciences, 47(11), 1482-1489. doi:10.1016/j.ijthermalsci.2007.11.003

20. Daguenet-Frick, X., Bonjour, J., & Revellin, R. (2010). Constructal microchannel network for flow boiling in a disc-shaped body. IEEE Transactions on Components and Packaging Technologies, 33(1), 115-126. doi:10.1109/TCAPT.2009.2027427

21. Ghaedamini, H., Salimpour, M. R., & Campo, A. (2011). Constructal design of reverting microchannels for convective cooling of a circular disc. International Journal of Thermal Sciences, 50(6), 1051-1061. doi:10.1016/j.ijthermalsci.2011.01.014

22. C.D. Murray. (1926). The physiological principle of minimum work, in the vascular system, and the cost of blood-volume ??

23. Wechsatol, W., Lorente, S., & Bejan, A. (2002). Optimal tree-shaped networks for fluid flow in a disc-shaped body. International Journal of Heat and Mass Transfer, 45(25), 4911-4924. doi:10.1016/S0017-9310(02)00211-9

24. Acheson, D. J. (1991). Elementary fluid dynamics. The Journal of the Acoustical Society of America, 89(6), 3020. doi:10.1121/1.400751

25. Bejan, A. (2013). Convection heat transfer / adrian bejan (4th ed.). Hoboken, New Jersey: Wiley.

26. Wechsatol, W., Lorente, S., & Bejan, A. (2006). Tree-shaped flow structures with local junction losses. International Journal of Heat and Mass Transfer, 49(17-18), 2957-2964. doi:10.1016/j.ijheatmasstransfer.2006.01.047

27. Ghaedamini, H., Salimpour, M. R., & Mujumdar, A. S. (2011). The effect of svelteness on the bifurcation angles role in pressure drop and flow uniformity of tree-shaped microchannels. Applied Thermal Engineering, 31(5), 708-716. doi:10.1016/j.applthermaleng.2010.10.005

28. Ghalichi, F., Deng, X., Champlain, A. D., Douville, Y., King, M., & Guidoin, R. (1998). Low reynolds number turbulence modeling of blood flow in arterial stenoses. Biorheology, 35(4), 281-294. doi:10.1016/S0006-355X(99)80011-0

29. Miguel, A. F. (2010). Dendritic structures for fluid flow: Laminar, turbulent and constructal design. Journal of Fluids and Structures, 26(2), 330-335. doi:10.1016/j.jfluidstructs.2009.11.004

30. Fluent theory guide. (2021). Retrieved from https://ansyshelp.ansys.com/account/secured?returnurl=/Views/Secured/corp/v192/wb2_help/wb2h_Fluentapp.html?q=fluent%20theory%20guide

31. B. E. Launder and D. B. Spalding. (1972). Mathematical models of turbulence, 169.